

---

[All ETDs from UAB](#)

[UAB Theses & Dissertations](#)

---

2014

## Exploring Intrinsic Biomarkers For Optical Assessment Of Outer Retina

Rongwen Lu  
*University of Alabama at Birmingham*

Follow this and additional works at: <https://digitalcommons.library.uab.edu/etd-collection>

---

### Recommended Citation

Lu, Rongwen, "Exploring Intrinsic Biomarkers For Optical Assessment Of Outer Retina" (2014). *All ETDs from UAB*. 2343.

<https://digitalcommons.library.uab.edu/etd-collection/2343>

This content has been accepted for inclusion by an authorized administrator of the UAB Digital Commons, and is provided as a free open access item. All inquiries regarding this item or the UAB Digital Commons should be directed to the [UAB Libraries Office of Scholarly Communication](#).

EXPLORING INTRINSIC BIOMARKERS FOR OPTICAL ASSESSMENT OF  
OUTER RETINA

by

RONGWEN LU

XINCHENG YAO, COMMITTEE CHAIR  
FRANKLIN R. AMTHOR  
CHRISTINE A. CURCIO  
ALLAN C. DOBBINS  
LEI LIU  
ANDREW E. POLLARD

A DISSERTATION

Submitted to the graduate faculty of The University of Alabama at Birmingham,  
in partial fulfillment of the requirements for the degree of  
Doctor of Philosophy

BIRMINGHAM, ALABAMA

2014

Copyright by  
Rongwen Lu  
2014

EXPLORING INTRINSIC BIOMARKERS FOR OPTICAL ASSESSMENT OF  
OUTER RETINA

Rongwen Lu

BIOMEDICAL ENGINEERING

ABSTRACT

The retina suffers pathological changes after attacked by eye diseases. The objective of my PhD dissertation is to explore intrinsic biomarkers for noninvasive assessment of retinal morphological structure and physiological function. Fundus autofluorescence (FAF), optical coherence tomography (OCT), etc. have provided indispensable information for eye disease detection. However, better understanding of the intrinsic biomarkers in FAF and OCT is desirable for quantitative interpretation of clinical outcomes.

The first specific aim of the dissertation research was to characterize FAF signals across the whole retinal depth using two-photon excitation. FAF signals are usually attributable to fluorophores from the choroidal vessel and the retinal pigment epithelium. However, whether other retinal layers contribute to FAF is still unknown. Results from my study showed that FAF signals existed throughout all retinal layers. The second specific aim was to investigate the anatomic correlates to the presumed ‘inner segment/outer segment’ (‘IS/OS’) OCT band. This was accomplished by comparing histological images with OCT images acquired by a custom-designed line-scan OCT with high spatial resolution. Although OCT has been widely used in clinical diagnosis, anatomic sources of the OCT bands at the outer retina, particularly the presumed ‘IS/OS’ photoreceptor OCT band, are still controversial. Our experimental result supported

conjecture that the presumed 'IS/OS' OCT band actually was originated from the IS. The third aim was to characterize a functional biomarker, stimulus-evoked transient phototropism of photoreceptors which was dominant in rods. Functional impairments may precede detectable structural abnormalities. Therefore, functional biomarkers promise early detection of eye diseases. This rod-dominant transient phototropic adaptation provides a specific functional biomarker to evaluate the functional integrity of rod photoreceptors. The last specific aim was to develop an easy, low-cost and phase-artifact free super-resolution method, termed virtually structured detection (VSD), to double the resolution of a confocal point/line scanning system. High resolution imaging is important for reliable identification of structural and functional biomarkers. However, the transverse resolution of conventional imaging systems is fundamentally limited by light diffraction.

This dissertation research could not only generate in-depth understanding of intrinsic biomarkers of outer retina but also provide insights into the optimal design of imaging instruments for improved structural and functional assessment of the retina.

Keywords: optical coherence tomography, transient phototropism, photoreceptor, fundus autofluorescence, virtually structured detection

## DEDICATION

I would like to dedicate this thesis to my parents who trust me and encourage me to pursuit my dreams. Also, I would like to dedicate this thesis to my beloved wife, Qiuxiang Zhang, and to my lovely daughter, Mabel E. Lu. Both of them are the greatest gifts to me.

## ACKNOWLEDGEMENT

First, I would like to thank my supervisor Dr. Xincheng Yao. He is a great mentor for me, leading me to step into the research field, giving me enough space to have independent judgment, guiding me back on the track when I went astray and preparing me for the next step of my research career. I have learnt the importance of planning research projects ahead in time and doing research meticulously.

I am grateful to my dissertation committee members, Dr. Franklin Amthor, Dr. Christine Curcio, Dr. Allan Dobbins, Dr. Lei Liu and Dr. Andrew Pollard, for their caring and encouragement. I see their wisdom from their teaching, passion from their research and vision from insightful suggestions and comments at my annual committee meeting.

I also want to express my sincere gratitude to coworkers at BCCC campus fellowship, Guoqiao Wang, Jige Guo, Lingfei Guo, Yanli Xie, Qiqi He, Benquan Wang, Jianguang Zhu, Xinyan Zhang, etc.. They are also my dear friends. I learnt from them that research is analogous to the service in campus fellowship. Communication skills are important for interpersonal relationship. However, love is fundamental to this relationship. Likewise, although technical skills such as image processing and data analysis are important to the research, other factors are essential to become a good scientist: love, creativity and perseverance. Among these the greatest is love.

This dissertation was supported in part by R01EY023522, NSF CBET-1055889, NSF EPSCoR-1158862, NIH R21 RR025788, NIH R21 EB012264, and UASOM I3 Pilot Award.

## TABLE OF CONTENTS

	<i>Page</i>
ABSTRACT .....	iii
DEDICATION .....	v
ACKNOWLEDGEMENT .....	vi
LIST OF FIGURES .....	ix
LIST OF ABBREVIATIONS.....	xii
INTRODUCTION .....	1
Section I: Background.....	4
Confocal scanning imaging system .....	4
LS-OCT .....	7
Fast functional imaging .....	14
VSD .....	16
Section II: Overview of dissertation research .....	22
TWO-PHOTON EXCITED AUTOFLUORESCENCE IMAGING OF FRESHLY ISOLATED FROG RETINAS .....	26
INVESTIGATION OF THE HYPER-REFLECTIVE INNER/OUTER SEGMENT BAND IN OPTICAL COHERENCE TOMOGRAPHY OF LIVING FROG RETINA .....	47
DYNAMIC NEAR-INFRARED IMAGING REVEALS TRANSIENT PHOTOTROPIC CHANGE IN RETINAL ROD PHOTORECEPTORS.....	59
SUPER-RESOLUTION SCANNING LASER MICROSCOPY THROUGH VIRTUALLY STRUCTURED DETECTION .....	79
RAPID SUPER-RESOLUTION LINE SCANNING MICROSCOPY THROUGH VIRTUALLY STRUCTURED DETECTION .....	99
SUMMARY .....	113
GENERAL LIST OF REFERENCES .....	117



APPENDIX A: INSTITUTIONAL ANIMAL CARE AND USE COMMITTEE.....122

## LIST OF FIGURES

*Figure* *Page*

### INTRODUCTION

1 Fig. 1. Histological image of the frog retina. ....	1
2 Fig. 2. Optical diagram for confocal imaging system.....	5
3 Fig. 3. Confocal line-scan microscopy. ....	7
4 Fig. 4. Simulation of OCT principle. ....	9
5 Fig. 5. Optical diagram of LS-OCT. ....	12
6 Fig. 6. OCT IOS imaging.....	15
7 Fig. 7. Optical diagram for conventional SIM.....	18
8 Fig. 8. Schematic diagram of the optical setup of the VSD-based SLM. ....	21

### TWO-PHOTON EXCITED AUTOFLUORESCENCE IMAGING OFFRESHLY ISOLATED FROG RETINAS

1 Fig. 1. Schematic diagram of the experimental setup for two-photon imaging of the frog retina. ....	32
2 Fig. 2. Autofluorescence imaging of retinal slice. ....	33
3 Fig. 3. Two-photon excited autofluorescence imaging of the flat-mounted retina.....	35
4 Fig. 4. Autofluorescence comparison between rods and cones. ....	36
5 Fig. 5. Quantitative analysis of PIO autofluorescence.....	38
6 Fig. 6. Averaged autofluorescence of the PIO, ONL, OPL, INL, IPL and GCL.....	39

INVESTIGATION OF THE HYPER-REFLECTIVE INNER/OUTER SEGMENT  
BAND IN OPTICAL COHERENCE TOMOGRAPHY OF LIVING FROG RETINA

1 Fig. 1. Optical setup of LS-OCT.....	51
2 Fig.2. LS-OCT images.....	53
3 Fig. 3. Comparison between OCT and histological images.....	55

DYNAMIC NEAR-INFRARED IMAGING REVEALS TRANSIENT PHOTOTROPIC  
CHANGE IN RETINAL ROD PHOTORECEPTORS

1 Fig. 1. Schematic diagram of stimulation patterns. ....	63
2 Fig. 2. Oblique stimulus-evoked photoreceptor displacements. ....	68
3 Fig. 3. Photoreceptor displacements and IOS responses stimulated by circular stimulus (in transverse plane) with a Gaussian profile (in axial plane). ....	71
4 Fig. 4. Stimulus-evoked photoreceptor displacements at the mouse retina. ....	72

SUPER-RESOLUTION SCANNING LASER MICROSCOPY THROUGH  
VIRTUALLY STRUCTURED DETECTION

1 Fig. 1. Schematic diagram of experimental setup.....	83
2 Fig.2. Computational simulation of the VSD-based super-resolution imaging.....	89
3 Fig. 3. Implementation of the VSD-based super-resolution imaging on the resolution test target. ....	91
4 Fig. 4. VSD-based super-resolution imaging of freshly isolated frog retina. ....	92

RAPID SUPER-RESOLUTION LINE SCANNING MICROSCOPY THROUGH  
VIRTUALLY STRUCTURED DETECTION

1 Fig. 1. Schematic diagram of experimental setup.....	103
2 Fig. 2. VSD-based super-resolution LSM on the resolution test target.....	106

3 Fig. 3. VSD-based super-resolution LSM imaging of freshly isolated  
frog retina. .... 108

## LIST OF ABBREVIATIONS

AMD	age-related macular degeneration
AP	avalanche photodiode
FAF	fundus autofluorescence
GCL	ganglion cell layer
INL	inner nuclear layer
IOS	intrinsic optical imaging
IPL	inner plexiform layer
IS	inner segment
LSM	line-scan microscopy
LS-OCT	line-scan optical coherence tomography
NA	numerical aperture
NFL	nerve fiber layer
NIR	near infrared
OCT	optical coherence tomography
OLM	outer limiting membrane
ONL	outer nuclear layer
OPL	outer plexiform layer
OS	outer segment
PIO	photoreceptor inner segment and outer segment

PMT	photomultiplier tube
PSF	point spread function
RP	retinitis pigmentosa
RPE	retinal pigment epithelium
SIM	structured illumination microscopy
SLD	superluminescent diode
SLM	scanning laser microscopy
SLO	scanning laser ophthalmoscopy
VSD	virtually structured detection

## INTRODUCTION

The retina is a light sensitive tissue, located at the posterior segment of the eye. As shown in Fig. 1, the retina consists of several anatomical layers: the retinal pigment epithelium (RPE) layer, the photoreceptor inner segment (IS) and outer segment (OS), the outer limiting membrane (OLM), the outer nuclear layer (ONL), the outer plexiform layer (OPL), the inner nuclear layer (INL), the inner plexiform layer (IPL), the ganglion cell layer (GCL) and the nerve fiber layer (NFL). Photoreceptor cells extend from the RPE to the OPL. In clinical usage, the term photoreceptor layer (PRL) includes all parts of photoreceptor cells [1]. However, in lots of publications, the PRL only refer to the photoreceptor IS and OS. To avoid confusion, in this dissertation, we use PIS to refer to photoreceptor IS and OS. The retinal photoreceptors detect light and transform it into neural and chemical signals. This process is known as phototransduction.

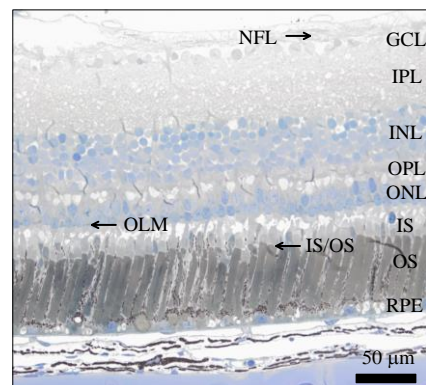


Fig. 1. Histological image of the frog retina. NFL: nerve fiber layer; GCL: ganglion cell layer; IPL: inner plexiform layer; INL: inner nuclear layer; OPL: outer plexiform layer; ONL: outer nuclear layer; IS: inner segment; OS: outer segment; IS/OS: inner

segment/outer segment junction, and RPE: retinal pigment epithelium. (Courtesy: Dr. Christine A. Curcio)

Photopigments at the photoreceptor OS undergo conformational change after capturing photons. The structural change of pigment molecules activates the phototransduction cascades which ultimately lead to closure of ion channels and hyperpolarization of the photoreceptor membrane. The outer retina, i.e., the IS and OS of photoreceptors, suffers pathological changes in many eye diseases such as age-related macular degeneration (AMD) [2, 3], and retinitis pigmentosa (RP) [4]. Without treatment, they may cause severe visual loss or even legal blindness. Examining the structural and functional biomarkers of the retina is important for retinal disease diagnosis and treatment evaluation.

Retinal imaging can be divided into two categories: fluorescence imaging and reflection imaging. For the fluorescence imaging, exogenous fluorophores such as fluorescein and indocyanine green (ICG) are commonly used for angiography to allow identification of leakage of blood vessels at the retina or choroidal neovascularization [5-7]. Both fluorescein angiography and ICG angiography are useful clinical diagnostic tools. However, they are invasive and may cause side effects [8, 9]. Alternatively, fundus autofluorescence (FAF) which explores intrinsic endogenous fluorophores for retinal imaging has been used for eye disease diagnosis and exploration of pathophysiologic mechanisms [10]. The FAF image is typically acquired by scanning laser ophthalmoscopy (SLO) with a specific wavelength filter. Previous studies suggest that lipofuscin in the RPE, all-trans retinol, reduced nicotinamide adenine dinucleotide (NADH) and reduced nicotinamide adenine dinucleotide phosphate (NADPH),



collectively referred to as NAD(P)H, at the PIO could contribute to FAF signals [11-13]. However, whether other retinal layers contribute to FAF signals is still unknown. It is thus important to characterize FAF signals throughout all retinal layers for accurate quantification and interpretation of FAF.

FAF detects signals in wavelengths longer than that of the excitation light. In contrast, the reflection imaging modality detects reflection light at the same wavelength as the illumination light. The most common clinical reflection retinal imaging modalities include fundus camera, SLO and optical coherence tomography (OCT). A fundus camera has a big field of view, but it suffers from low resolution which precludes it from detecting fine structures. SLO is an imaging modality based on confocal configuration which can reject out-of-focus light. With the aid of adaptive optics, SLO is able to reach diffraction-limited resolution on transverse direction. OCT is celebrated by its three-dimensional imaging capacity with unparalleled axial resolution. OCT has provided indispensable information for clinical applications.

This dissertation research focused on investigation of intrinsic structural biomarkers from FAF [14] and OCT [15]. Sources of FAF signals and origins of 'IS/OS' OCT band were investigated. In addition, this dissertation research extended the intrinsic structural biomarkers to intrinsic functional biomarkers which promised early detection of eye diseases [16]. Particularly, transient photoreceptor phototropic adaptation was studied [17]. Moreover, this dissertation research developed a super-resolution method, termed virtually structured detection (VSD), which can break the diffraction limit for both SLO [18], OCT [19] and other confocal scanning imaging systems on transverse direction. Super-resolution allows characterizing fine biomarkers which is not resolvable

by conventional imaging modalities with diffraction-limited resolution. To fully understand my work, I include background information on confocal scanning imaging system, line-scan OCT (LS-OCT), fast functional imaging and VSD in Section I and the overview of this dissertation research in Section II.

## Section I: Background

### *Confocal scanning imaging system*

The confocal scanning imaging system is in the key of this dissertation research. In a confocal scanning imaging system, only one point on the specimen is illuminated and detected at a time. Thus, unwanted scattered light from other areas of the specimen could be minimized comparing to wide field illumination. In addition, the confocal configuration can further reject out-of-focus light and multiple scattered light to increase the contrast of the image, particularly in thick specimens. The prototype of confocal scanning laser microscopy (SLM) was invented by Minsky in 1950s [20]. However, it took another thirty years for confocal SLM to become a standard technique for biological imaging.

Fig. 2 shows an example of confocal SLM/SLO. The light source could be a laser or superluminescent diode (SLD). The light is focused to a single point on the specimen. A pair of scanners is used to steer the focused NIR light across the specimen to generate a two-dimensional (2D) image with a raster scanning pattern. In order to control the vignetting effect, the middle point between two scanners is relayed to the Fourier plane (back focal plane) of the objective. The reflected light from the specimen is descanned by the 2D scanning system before relayed to the image plane. The detector typically could

be avalanche photodiode (AP) or photomultiplier tube (PMT). In front of the detector a pinhole is placed. The pinhole is conjugate to the specimen. The pinhole can reject the out-of-focus light, as shown in Fig. 2B.

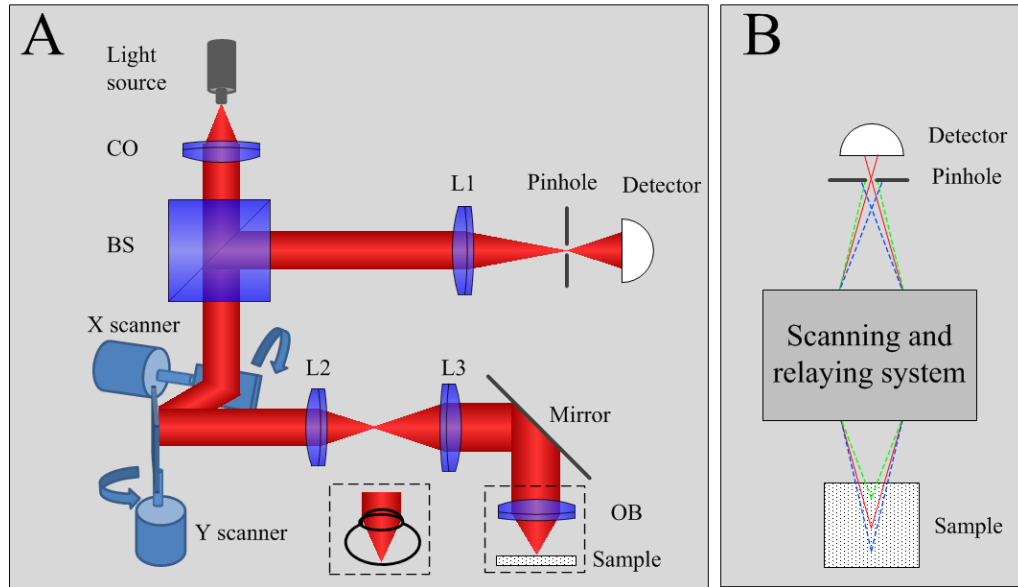


Fig. 2. Optical diagram for confocal imaging system. (A) Optical diagram for confocal SLM and SLO. CO: collimator; BS: beam splitter; OB: objective and L1-L3 lenses. Confocal SLO in principle is the same as SLM, except that there is not objective. In SLO, parallel light is delivered to the eye and converged to a single point at the retina by the cornea and the lens in the eye. (B) Diagram showing optical sectioning ability of confocal configuration.

In theory, confocal configuration can improve the resolution by a factor of the square of 2, if the confocal pinhole is small enough [21]. However, confocal SLM gains its reputation mainly because of its sectioning ability rather than the enhancement of lateral resolution. First, to achieve the lateral resolution enhancement, the confocal pinhole should be minimized, in theory to zero, which reduces the throughput of light for imaging. Second, microscopies, particularly in the thick specimens, may not even achieve

diffraction limit resolution because of aberrations introduced by the specimens and optics. If the beam splitter in Fig.2 is replaced by a dichroic mirror, the confocal SLM can be used for the fluorescence imaging. If two-photon excitation is used, the excited fluorescence intensity is proportional to the square of the excitation light intensity. Only fluorophores within the focal spot are excited. Therefore, the pinhole and the de-scanning system are not necessary. The first specific aim of this dissertation research was to investigate the FAF through all retinal layers using two-photon excitation. The used system was a confocal scanning system without a pinhole or a descanning scheme.

The biggest limitation of a confocal SLM is that it can only image a single point at a time. It takes time to generate a 2D image through raster scanning, as shown in Fig. 3C. One strategy to increase confocal SLM imaging speed is to change it to line illumination. In one direction it is still the confocal configuration, while in the orthogonal direction the illumination is constant. Only one dimensional scanning is needed. Therefore, imaging speed can be increased. A linear camera can be used to record the signals.

Fig.3 shows the mechanism of confocal line-scan microscopy (LSM). A cylindrical lens (CL) is used to condense the light into a focused line, which is projected to the specimen. From the side view of the illumination path (Fig. 3B), the cylindrical lens CL acts as a glass plate and does not converge the light. The focused line is swept across the specimen by a scanning mirror. The reflected light from the specimen is descanned by the scanner, and is relayed to the image plane. The linear camera itself can act as a confocal aperture to reject the out-of-focus light. Thus no additional confocal aperture is needed. Because of the line illumination, only one dimensional scanning

pattern is necessary, as shown in Fig. 3D. Therefore, the imaging speed can be enhanced comparing to the raster scanning pattern (Fig. 3C).

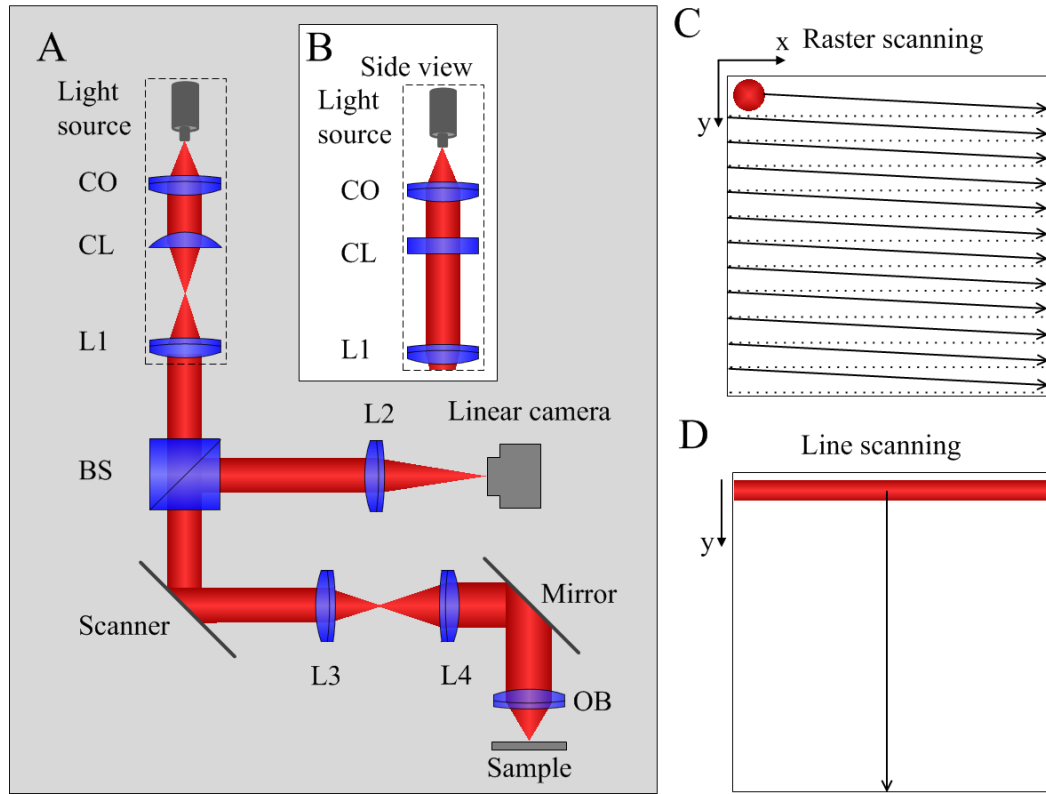


Fig. 3. Confocal line-scan microscopy. (A) Optical diagram for confocal SLM and SLO. CO: collimator; CL: cylindrical lens; BS: beam splitter; OB: objective and L1-L4 lenses. Confocal SLO has the same spirit with SLM, except that there is not objective. (B) Side view of the illumination path. (C) Raster scanning pattern; (D) Line scanning pattern.

### *LS-OCT*

The aforementioned confocal SLM configuration with a single point scanning pattern and the LSM with a line scanning pattern can reject out-of-focus light, thus allowing optical sectioning ability. However, their axial resolution is fundamentally limited by the numerical aperture (NA) of the objective.

$$r_{axial} = 1.4\lambda n / NA^2 \quad (1)$$

where  $\lambda$  is the wavelength and  $n$  is the refractive index of the specimen. The NA of the human eye is 0.1 [22]. If the illumination with a wavelength of 0.83 nm is used, the axial resolution is more than 150  $\mu\text{m}$ , coarser than individual retinal functional layers. To improve the axial resolution, OCT technique can be employed. OCT uses a light source with a low coherence length to generate interference fringes to gate the signals from different depths. The axial resolution of the OCT is independent of the NA of the objective.

Fig. 4 shows the principle of time-domain OCT principle. Fig. 4A is the optical diagram of a Michelson interferometer. The movement of the Mirror 2 generates a relative displacement  $\Delta L$  between Mirror 1 and Mirror 2. Fig. 4B shows the intensity acquired at the detector for three individual wavelengths, 770 nm, 830 nm and 890 nm. If the relative displacement  $\Delta L$  is 0, light from the reference beam (i.e., from Mirror 1) and from the sample beam (i.e., from Mirror 2) should interfere constructively at the detector, no matter at what wavelength the light is. In other words, all wavelengths are in phase if the relative displacement is 0. If  $\Delta L$  is not equal to 0, the in-phase condition cannot longer hold. Light may interfere constructively at some wavelengths but destructively at other wavelengths. Therefore, they are out of phase, which can be directly seen in Fig. 4C (i.e., at  $\Delta L=2 \mu\text{m}$ ). If we assume the light source is SLD with the center wavelength  $\lambda_0=830 \text{ nm}$  and the bandwidth  $\Delta\lambda=60 \text{ nm}$ , integration of interference intensity over all wavelengths generates the curve as shown in Fig. 4D. The overall profile is a Gaussian curve, while the oscillation curve within the profile is a sinusoidal function. In Fig. 4D, it is assumed that the power spectral density of the light source is a Gaussian function.

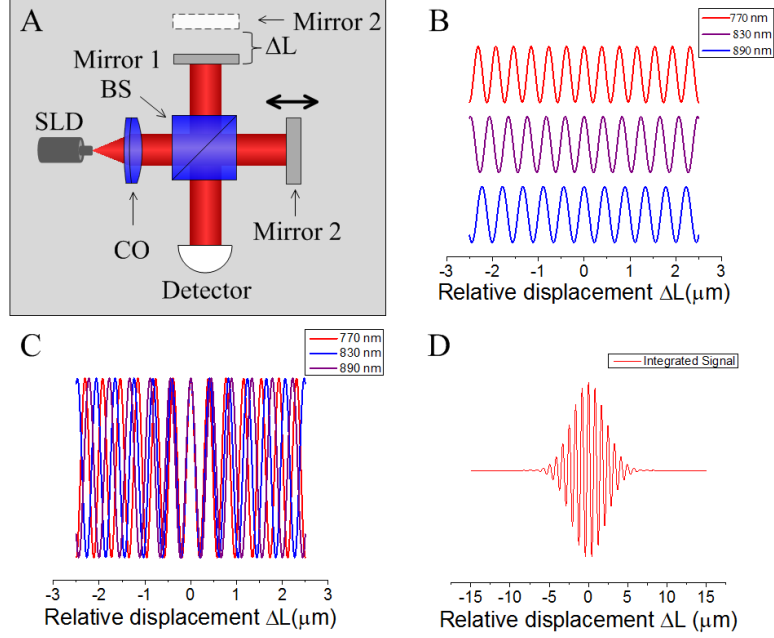


Fig. 4. Simulation of OCT principle. (A) Michelson interferometer. CO: collimator and BS: beam. The position of the Mirror 2 is moving, generating relative displacement  $\Delta L$  with respect to Mirror 1. The light source of SLD with center wavelength of 830 nm and bandwidth of 60 nm is assumed. (B) The intensity captured by the detector for three individual wavelengths, 770 nm, 830 nm and 890 nm as a function of relative displacement  $\Delta L$ . (C) Overlapped intensity profiles as a function of relative displacement for three individual wavelengths, 770 nm, 830 nm and 890 nm. (B) and (C) have the same data. It is worth noting that different wavelengths should have different intensities in theory. In (B) and in (C), intensity for individual wavelengths is normalized for a better comparison. (D) Integrated signal over all wavelengths captured by the detector as a function of the relative displacement  $\Delta L$ .

For individual wavelength  $\lambda$ , the detector in the interferometer captures the intensity of interference  $I_f$  between the reference field and the sample field:

$$I_f = S(f)[I_S + I_R + 2\sqrt{I_S I_R} \cos(2\pi f x)] \quad (2)$$

where  $x = 2\Delta L$ ;  $f = 1/\lambda$ ;  $S(f)$  is the power spectral density of the light source, and  $I_R$  and  $I_S$  are the mean intensities of the reference arm and the sample arm for individual wavelength  $\lambda$ , respectively. In Eq. (2),  $S(f)$  means different wavelengths have different weights. Integration of Eq. (2) over all wavelengths yields:

$$\begin{aligned}
I(x) &= \int_{-\infty}^{\infty} I_f df \\
&= \int_{-\infty}^{\infty} S(f)(I_S + I_R)df + \int_{-\infty}^{\infty} 2\sqrt{I_S I_R} S(f) \cos(2\pi f x) df \\
&= A + B \int_{-\infty}^{\infty} S(f) \cos(2\pi f x) df
\end{aligned} \tag{3}$$

where  $A$  and  $B$  are constant coefficients. Applying Euler's formula in Eq. (3) generates:

$$I(x) = A + B \operatorname{Re}[K(x)] \tag{4}$$

where

$$K(x) = \int_{-\infty}^{\infty} S(f) \exp(-j2\pi f x) df \tag{5}$$

Eq. (5) means that  $K(x)$  coincides with the Fourier transform of the power spectrum density of the light source. If we assume  $S(f)$  is a Gaussian function symmetric with respect to  $f_0$ :

$$S(f) = \operatorname{Gauss}(f - f_0, \delta) \tag{6}$$

where:

$$\operatorname{Gauss}(f, \delta) = \frac{1}{\delta\sqrt{2\pi}} \exp[-f^2/(2\delta^2)] \tag{7}$$

Substituting Eq.(6) into Eq. (5) generates:

$$K(x) = \exp(-j2\pi f_0 x) \int_{-\infty}^{\infty} \operatorname{Gauss}(f, \delta) \exp(-j2\pi f x) df = \exp(-j2\pi f_0 x) \hat{G}(x) \tag{8}$$



where  $\hat{G}(x)$  is the Fourier transform of the  $Gauss(f, \delta)$ . Because  $Gauss(f, \delta)$  is a Gaussian function symmetric with respect to 0, its Fourier transform  $\hat{G}(x)$  is also a real Gaussian function. Therefore,

$$\text{Re}[K(x)] = \text{Re}[\exp(-j2\pi f_0 x) \hat{G}(x)] = \hat{G}(x) \cos(2\pi f_0 x) \quad (9)$$

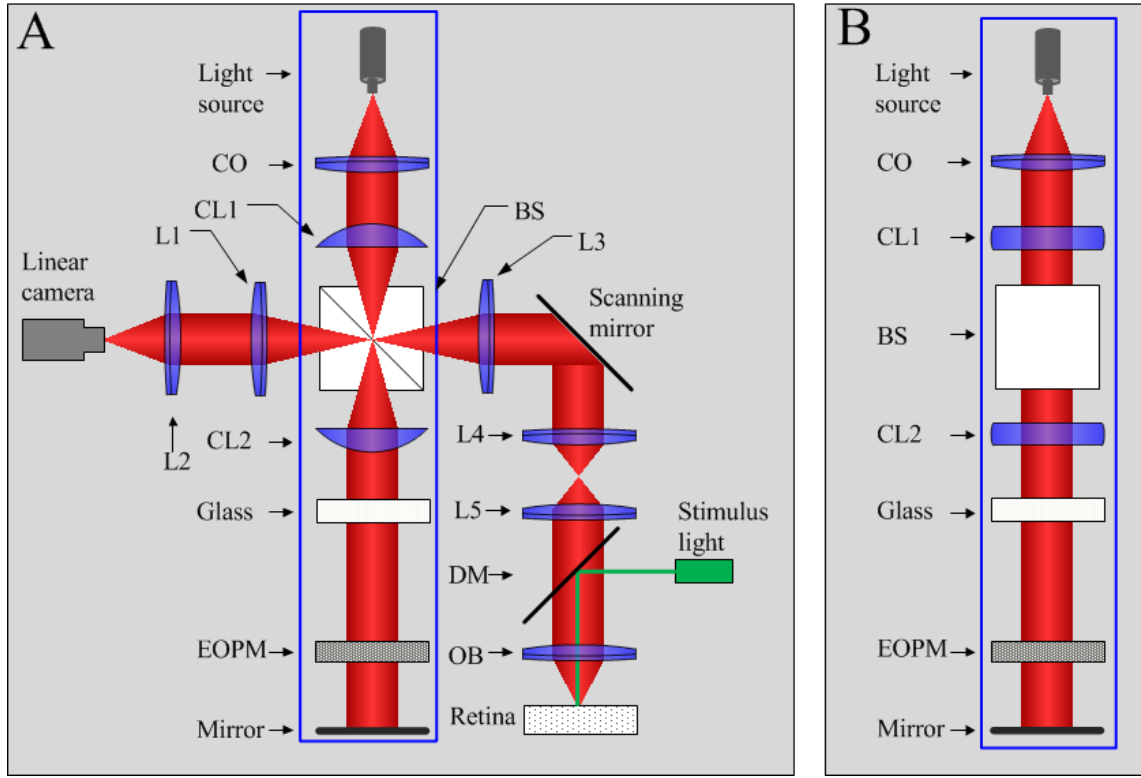
It consists of two functions. The overall profile is a Gaussian function, while within the profile it is a sinusoidal function, as shown in Fig. 4D. The axial resolution of the OCT is defined by the full width at half maximum of  $\hat{G}(x)$  [23]:

$$r_{axial} = \frac{2 \ln 2}{\pi} \frac{\lambda_0^2}{\Delta \lambda} \quad (10)$$

If we assume the center wavelength is  $\lambda_0=830$  nm the bandwidth is  $\Delta\lambda=60$  nm, the axial resolution is about 5  $\mu\text{m}$ .

Because of its high axial resolution, OCT technique is ideal for imaging the retina. It has provided invaluable information about the retinal diseases. However, the anatomic sources of the OCT bands at the outer retina, in particular, the presumed ‘IS/OS’ OCT band, are still controversial. The second specific aim of this dissertation research was to investigate the anatomic correlates to the presumed ‘IS/OS’ OCT band. To facilitate the investigation, we used a LS-OCT system that combined the LSM and OCT techniques, as shown in Fig. 5. It has several advantages. First, the axial resolution is high which is 5  $\mu\text{m}$  in the air according to Eq. (10). Second, the transverse resolution is determined by the NA of the objective. Because it is a time domain OCT, we move the sample so that each layer is acquired at the focal plane. Therefore, the transverse resolution of the system is consistent with respect to all retinal depths, which is useful to obtain high-quality OCT image of the retina. Third, it is a line-scan system with a fast enface imaging

speed (i.e., up to 1 k frames/s), which is capable for transient functional imaging.



Note: Adapted from “En Face Optical Coherence Tomography of Transient Light Response at Photoreceptor Outer Segments in Living Frog Eyecup” by B. Q. Wang, R. W. Lu, Q. X. Zhang, Y. Q. Jiang and X. C. Yao, 2013, *Optics Letters*, 38, p. 4526-4529. Copyright 2013 by Optical Society of America. Adapted with permission.

Fig. 5. Optical diagram of LS-OCT. BS: beam splitter; DM: dichroic mirror; CO: collimator, L1~L5: lenses; OB: objective; CL1 and CL2: cylindrical lenses; and EOPM: electro-optic phase modulator. The focal length of CL1, CL2, L1~L5 was 40mm, 40mm, 40mm, 80mm, 80mm, 40mm, and 75mm, respectively. (B) The side view of the optical geometry of the illumination and reference paths, specified by the blue square in (A).

Fig. 5 shows a practical design for LS-OCT. It is a LSM with line scanning pattern combined with a reference beam. In the illumination path (optics above the BS, Fig.5A), a cylindrical lens CL1 is used to condense the parallel light in one dimension to a single line. This line in turn is relayed to the retina through lenses L3, L4, L5 and the

objective OB. Fig. 5B shows side view of the illumination and reference paths (blue square in Fig. 5A). In the side view, the cylindrical lenses CL1 and CL2 act as a pair of glass plates and do not blend light. The linear camera (spL2048-140k, Basler Sprint) is conjugate to the focused line illumination. The line-sensor (1 x 2048 pixels, 10  $\mu\text{m}$  x 10  $\mu\text{m}$ ) of the linear camera is small and can naturally acts as a spatial-filter to reject out-of-focus light. Therefore, the confocal configuration is achieved.

In the reference path (optics below the BS, Fig.5A), another cylindrical lens CL2 is used to convert the focused light back to a parallel light beam before entering the electro-optic phase modulator (EOPM). EOPM is used to generate rapid vibration- and inertia- free phase modulation [24]. The glass block in the reference arm is used to compensate for optical dispersion of the sample beam. A four-step phase-shifting strategy is employed to retrieve OCT images [25].

To simplify the discussion, we assume the scanning mirror is static. The interference signal at the linear camera is

$$I_{t_i}(x) = \left| \sqrt{I_s(x)} + \sqrt{I_R(x)} \exp[j(\alpha + \theta(t_i))] \right|^2 \quad (11)$$

where  $I_s$  is the intensity from sample arm.  $t_i$  is the time.  $\alpha$  is the constant phase difference between sample and reference arms. The phase modulation produced by EOPM is  $\theta(t_i) = 0.5i\pi$ , where  $i = 0,1,2,3$ .  $I_s$  can be reconstructed by:

$$I_s(x) = [(I_{t_0}(x) - I_{t_2}(x))^2 + (I_{t_1}(x) - I_{t_3}(x))^2] / I_R(x) \quad (12)$$

If uniformity of the light intensity distribution of the reference arm is assumed:

$$I_R(x) = c \quad (13)$$

Substituting Eq. (13) into Eq. (12) and ignoring constant coefficients yield:

$$I_s(x) = [(I_{t_0}(x) - I_{t_2}(x))^2 + (I_{t_1}(x) - I_{t_3}(x))^2] \quad (14)$$

Thus the OCT image can be reconstructed.

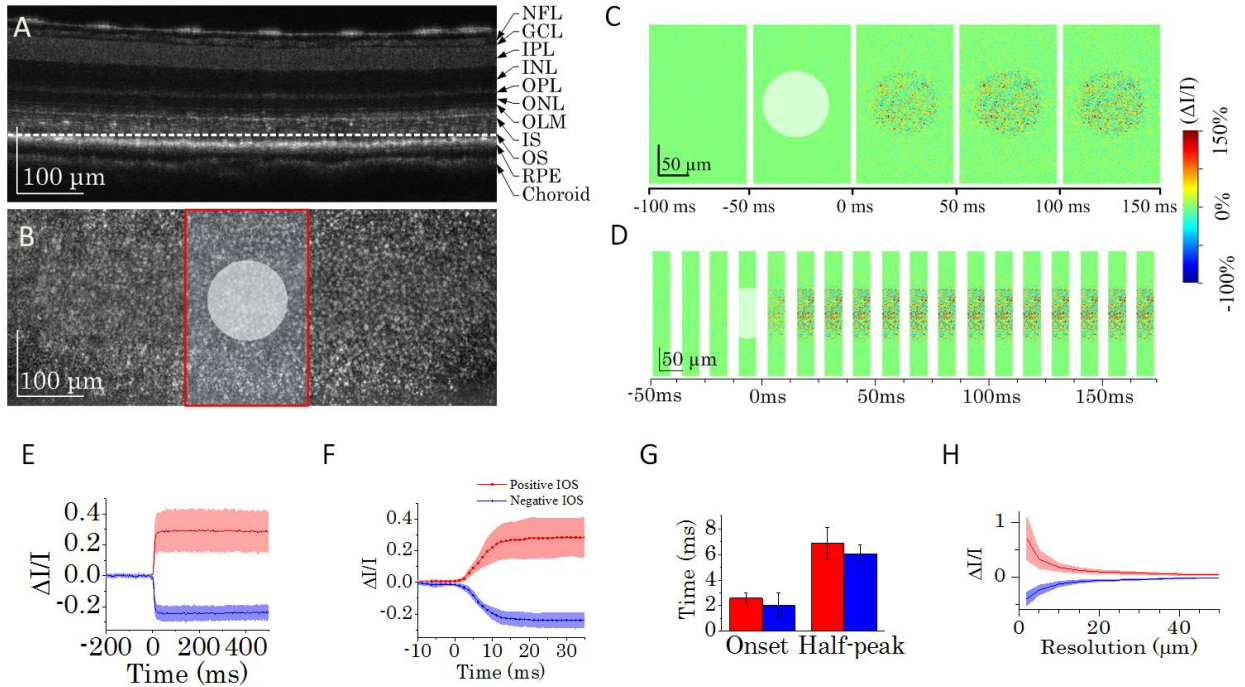
### *Fast functional imaging*

High resolution functional examination of retinal photoreceptors is essential for early retinal disease detection and treatment evaluation. Electroretinogram (ERG) [26], focal ERG , multifocal ERG [27], etc. have been used to evaluate the retinal function clinically. Electrodes are used for these methods to record the stimulus-evoked electrical signals. Their spatial resolution is limited, and thus is not able to identify localized retinal dysfunctions precisely.

Intrinsic optical signal (IOS) imaging promises a non-invasive functional evaluation of the retina with high spatial resolution. After a visible stimulus light flash is delivered to the retina, it not only generates electrical signals through phototransduction but also produces changes of optical properties of the retina i.e., refractive index change of neural tissues [28] cell swelling [29], birefringence change [30, 31], molecule redistribution [32], etc.. Those changes can be reflected in the intensity change of the recording light which could be quantified by IOS method. IOS has been recorded at conventional microscopies [33], line-scan ophthalmology [34], and OCT [16, 32]. To illustrate IOS, we use OCT IOS imaging as an example [16].

The experiment was performed on the LS-OCT shown in Fig. 5. Fig. 6 shows an example of fast IOS imaging at ms level using LS-OCT. Fig. 6A was the reconstructed B-scan image. Fig. 6B shows an enface image at the photoreceptor OS. The recording light for OCT imaging was a SLD with a center wavelength  $\lambda_0=830$  nm and a bandwidth of  $\Delta\lambda=60$  nm. The stimulus light of 5 ms was delivered at 0 ms. A larger image field was

obtained at a frame rate of 200 fps (Fig. 6C). For a smaller image field, 800 fps frame rate could be achieved (Fig. 6D).



Note: Adapted from “En Face Optical Coherence Tomography of Transient Light Response at Photoreceptor Outer Segments in Living Frog Eyecup” by B. Q. Wang, R. W. Lu, Q. X. Zhang, Y. Q. Jiang and X. C. Yao, 2013, *Optics Letters*, 38, p. 4526-4529. Copyright 2013 by Optical Society of America. Adapted with permission.

Fig. 6. OCT IOS imaging. (A) OCT B-scan image. (B) Representative enface OCT image recorded at photoreceptor OS. The axial position is specified by the white dashed line in (A). The red rectangle area shows the area where IOS images were acquired for (C). The white spot indicates the green light stimulus. (C) IOS images acquired at 200 fps. (D) IOS images acquired at 800 fps. (E) Separate averages of positive and negative IOSs. Red curves represent positive IOS and blue curves represent negative IOS. Shadow areas show standard deviations. (F) Enlarged image of (B) from -10 to 35 ms. (G) Onset time and half-peak time of IOS signals. Red bars represent positive signals. Blue bar represent negative signals. (H) Relationship between resolution and IOS magnitudes. The spatial

resolution is decreased by applying different sized Butterworth windows in Fourier domain to OCT images.

IOS at time  $t_i$  can be calculated as:

$$IOS_{t_i}(x, y) = \frac{p_{t_i}(x, y) - p_{\text{ref}}(x, y)}{p_{\text{ref}}(x, y)} \quad (15)$$

where  $p_{t_i}$  is the OCT image at time  $t_i$  and  $p_{\text{ref}}$  is the reference image acquired by averaging all images before stimulus delivery. Fig. 6C and Fig. 6D show IOS maps. After stimulus flash (5 ms), both positive and negative IOSs could be observed (Figs. 6C-6F). The signal was extremely fast (onset time  $< 3$  ms, half-peak time  $< 10$  ms, Fig. 6G). The time course of the fast optical signals is comparable to ERG signals and can be used to evaluate the function of the photoreceptor OS. Fig. 6H shows that IOS magnitude decreases as a function of the transverse resolution, which implies that resolution is important for IOS imaging. The origins of IOS are very complex. We successfully isolated one mechanism: transient phototropism, which was the third specific aim of this dissertation research. Moreover, this transient phototropic adaptation was rod-dominant, which promised a new methodology to evaluate the rod function. This is valuable, because rods are more vulnerable than cones in initial stages in some eye diseases like AMD [3, 35] and RP [36].

## VSD

The transverse resolution of aforementioned systems including confocal SLM with signal point scanning pattern, confocal LSM with line scanning pattern, and OCT is all diffraction limited. For fluorescence imaging, multiple strategies have been developed to break the diffraction limit, such as stimulated emission depletion (STED) microscopy,

stochastic optical reconstruction microscopy (STORM) [37], photoactivated localization microscopy (PALM) [38], fluorescence PALM (FPALM) [39] and structured illumination microscopy (SIM) [40-42]. For the STED imaging, the shape of effective illumination point spread function (PSF) of the excitation light is sharpened by doughnut-shape depletion light which deactivates peripheral regions of the center focal spot while leaving the fluorophores at the desired center to emit fluorescence. Single-molecule imaging, i.e., STORM, PALM, and FPALM, alternatively can achieve super-resolution by localizing centroids of individual single molecules with photo-switchable fluorescence probes. Both STED and single-molecular imaging modalities requires specific dyes or fluorescent proteins, and are not suitable for autofluorescence imaging, or reflection/transmission imaging.

The SIM is applicable to both fluorescence [40-42] and reflection/transmission imaging [43, 44]. The SIM requires a sinusoidal patterned illumination to shift frequencies higher than the diffraction limit to lower frequencies so that the passing band of one optical system can be effectively expanded. However, for the purpose of the reconstruction, the SIM requires complicated mechanical manipulation of gratings [40-42] or grids [45, 46] to generate structured illumination patterns with specific phases, which becomes particularly challenging for a moving specimen. In addition, the conventional SIM requires a wide field illumination and is not feasible for confocal systems. Recently we have demonstrated the feasibility of super-resolution SLM, OCT and LSM via VSD. In the VSD-based system, the sinusoidal modulation is achieved by mathematical processing of digital images. The VSD-based super-resolution imaging is phase-artifact free and is suitable for both fluorescence (either exogenous fluorescence or

autofluorescence) imaging and reflection/transmission imaging in thick tissues. To fully understand principles of VSD, it is necessary to review the conventional SIM illustrated in Fig. 7 [40].

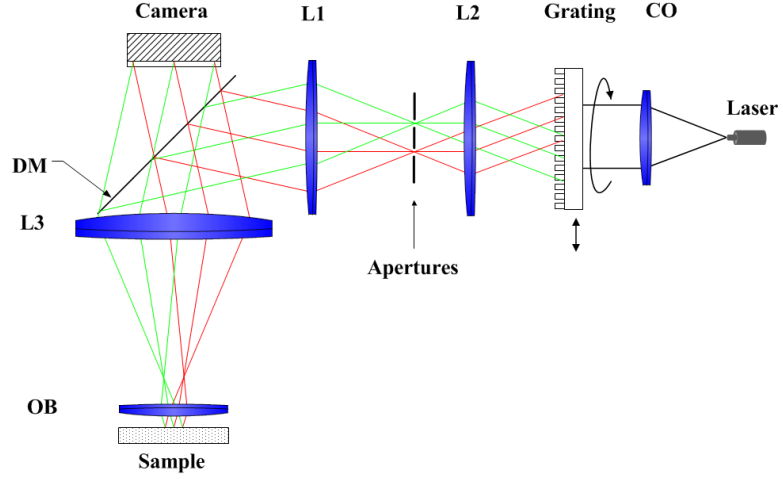


Fig. 7. Optical diagram for conventional SIM. DM: dichroic mirror; CO: collimator, L1~L3: lenses; and OB: objective. Apertures are for order selection. The grating is mounted on a translation stage for vertical movement manipulation. The translation stage in turn can be mounted on a rotation stage for the control of rotation movement.

As shown in Fig.7, the sinusoidal illumination is generated by interference between two oblique beams which are in turn created by a grating. The block in Fig. 7 is used to select only the first positive and negative diffraction orders. We assume that the point spread function (PSF) of the illumination path is  $h_{il}(x, y)$  and that the modulation function is  $m(x, y)$ . Then the illumination pattern on the specimen is  $h_{il}(x, y) \otimes m(x, y)$ , where  $\otimes$  denotes convolution. If we assume that the PSF of the detection path is  $h_{de}(x, y)$ , we will have image:

$$p(x, y) = \{s(x, y)[h_{il}(x, y) \otimes m(x, y)]\} \otimes h_{de}(x, y) \quad (16)$$



where  $s(x, y)$  is the reflectance ratio of the specimen for the reflection imaging or the fluorophore concentration for fluorescence imaging. Fourier transforming of Eq. (16) yields:

$$\tilde{p}(f_x, f_y) = \{\tilde{s}(f_x, f_y) \otimes [\tilde{h}_{il}(f_x, f_y) \tilde{m}(f_x, f_y)]\} \tilde{h}_{de}(f_x, f_y) \quad (17)$$

We assume the mask  $m(x, y)$  is a sinusoidal function:

$$m(x, y) = 1 + \cos[2\pi f_0(x \cos \theta + y \sin \theta) + \alpha] \quad (18)$$

We assume  $\theta = 0.5\pi$ . Then Fourier transform of Eq. (18) is:

$$\tilde{m}(f_x, f_y) = \sigma(f_x, f_y) + 0.5\sigma(f_x, f_y - f_0)e^{i\alpha} + 0.5\sigma(f_x, f_y + f_0)e^{-i\alpha} \quad (19)$$

Substituting Eq. (19) into Eq. (17) generates:

$$\tilde{p}(f_x, f_y) = [\tilde{s}(f_x, f_y) + 0.5\tilde{s}(f_x, f_y - f_0)e^{i\alpha} + 0.5\tilde{s}(f_x, f_y + f_0)e^{-i\alpha}] \tilde{h}_{de}(f_x, f_y) \quad (20)$$

where we assume that  $f_0$  is slightly smaller than the cutoff frequency of the illumination PSF. The second item and the third item in the square bracket contain the super-resolution information. We assume that:

$$\tilde{s}'(f_x, f_y) = \tilde{h}_{il}(f_x, f_y) \tilde{s}(f_x, f_y) \quad (21-a)$$

$$\tilde{s}'(f_x, f_y - f_0) = \tilde{h}_{il}(f_x, f_y) \tilde{s}(f_x, f_y - f_0) \quad (21-b)$$

$$\tilde{s}'(f_x, f_y + f_0) = \tilde{h}_{il}(f_x, f_y) \tilde{s}(f_x, f_y + f_0) \quad (21-c)$$

Substituting Eq. (21) into Eq. (20) yields:

$$\tilde{p}(f_x, f_y) = \tilde{s}'(f_x, f_y) + 0.5\tilde{s}'(f_x, f_y - f_0)e^{i\alpha} + 0.5\tilde{s}'(f_x, f_y + f_0)e^{-i\alpha} \quad (22)$$

If we move the grating vertically to generate three phases  $\alpha_1 = 0$ ,  $\alpha_2 = \frac{2}{3}\pi$  and  $\alpha_3 = \frac{4}{3}\pi$ ,

we will have:

$$\tilde{p}_1(f_x, f_y) = \tilde{s}'(f_x, f_y) + 0.5\tilde{s}'(f_x, f_y - f_0) + 0.5\tilde{s}'(f_x, f_y + f_0) \quad (23-a)$$

$$\tilde{p}_2(f_x, f_y) = \tilde{s}'(f_x, f_y) + 0.5\tilde{s}'(f_x, f_y - f_0)e^{i2\pi/3} + 0.5\tilde{s}'(f_x, f_y + f_0)e^{-i2\pi/3} \quad (23-b)$$

$$\tilde{p}_3(f_x, f_y) = \tilde{s}'(f_x, f_y) + 0.5\tilde{s}'(f_x, f_y - f_0)e^{i4\pi/3} + 0.5\tilde{s}'(f_x, f_y - f_0)e^{-i4\pi/3} \quad (23-c)$$

Solving Eq. (23) yields:

$$\begin{bmatrix} \tilde{s}'(f_x, f_y) \\ \tilde{s}'(f_x - f_0, f_y) \\ \tilde{s}'(f_x + f_0, f_y) \end{bmatrix} = \begin{bmatrix} 1 & 0.5 & 0.5 \\ 1 & 0.5e^{i2\pi/3} & 0.5e^{i2\pi/3} \\ 1 & 0.5e^{i4\pi/3} & 0.5e^{-i4\pi/3} \end{bmatrix}^{-1} \begin{bmatrix} \tilde{p}_1(f_x, f_y) \\ \tilde{p}_2(f_x, f_y) \\ \tilde{p}_3(f_x, f_y) \end{bmatrix} \quad (24)$$

Therefore, the super-resolution information can be recovered. To achieve isotropic resolution enhancement in all directions, it is necessary to rotate the grating.

Unlike conventional SIM which employs a grating to generate sinusoidal modulation of the illumination, the VSD-based system applies the modulation in the detection beam digitally. VSD does not require physical manipulation of the grating and can be applied to the confocal scanning imaging system. Fig. 8 shows the VSD-based super-resolution SLM. It is like the conventional confocal SLM, except that the pinhole and the single-element detector are replaced with a 2D CCD array. If we assume the scanning position is at  $(x_0, y_0)$  and that the illumination intensity is 1, then the light intensity distribution on the specimen is  $h_{il}(x - x_0, y - y_0)$ . In a descanned system as shown in Fig. 8, the light intensity distribution on the image plane (i.e., at the position of the CCD camera sensor) can be expressed as  $I_{des}(x, y, x_0, y_0)$ . After sampling and digitalization  $I_{des}(x, y, x_0, y_0)$  is stored in the computer. The nondescanned image can be obtained by shifting descanned images:

$$I_{non}(x, y, x_0, y_0) = I_{des}(x - x_0, y - y_0, x_0, y_0) \quad (25)$$

In a nondescanned system, we will have [47]:

$$I_{non}(x, y, x_0, y_0) = \iint h_{il}(\mu - x_0, \nu - y_0) s(\mu, \nu) h_{de}(x - \mu, y - \nu) d\mu d\nu \quad (26)$$

A digital mask is applied to multiple with the nondescanned image:

$$I_{mul}(x, y, x_0, y_0) = I_{non}(x, y, x_0, y_0)m(x, y) \quad (27)$$

The spatial integral of the image  $I_{mul}(x, y, x_o, y_o)$  is assigned to the position  $(x_o, y_o)$ :

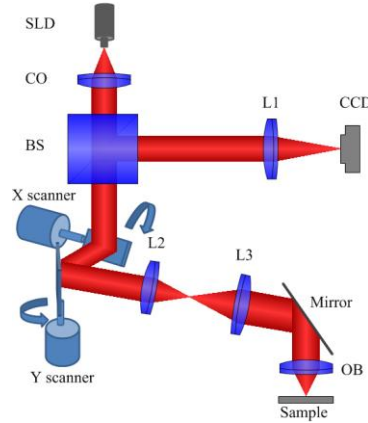
$$p(x_o, y_o) = \iint I_{mul}(x, y, x_o, y_o) dx dy \quad (28)$$

Substituting Eqs. (26) and (27) into Eq. (28) yields [47]:

$$\begin{aligned} p(x_o, y_o) &= \iint \iint h_{il}(\mu - x_o, \nu - y_o) s(\mu, \nu) h_{de}(x - \mu, y - \nu) m(x, y) d\mu d\nu dx dy \\ &= \iint h_{il}(\mu - x_o, \nu - y_o) s(\mu, \nu) [\iint h_{de}(\mu - x, \nu - y) m(x, y) dx dy] d\mu d\nu \\ &= h_{il}(x_o, y_o) \otimes \{s(x_o, y_o) [h_{de}(x_o, y_o) \otimes m(x_o, y_o)]\} \end{aligned} \quad (29)$$

where the integration order is changed, the fact that PSFs are even functions is assumed.

If we assume illumination PSF is equal to detection PSF, then Eq. (29) is equivalent to Eq. (16). Equivalency of Eq. (16) and Eq. (29) implies that modulation on the illumination beam and the detection beam is equivalent. Therefore, super-resolution information of the VSD-based system can be also achieved following the reconstruction method of the conventional SIM.



Note: From “Dynamic Near-infrared Imaging Reveals Transient Phototropic Change in Retinal Rod Photoreceptors” by R. W. Lu, A. M. Levy, Q. X. Zhang, S. J. Pittler and X. C. Yao, 2013, *Journal of Biomedical Optics*, 18, p. 106013. Copyright 2013 by SPIE. Reprinted with permission.

Fig. 8. Schematic diagram of the optical setup of the VSD-based SLM. OB: objective; CO: collimator; L1-L3: lens; and BS: beam splitter. Focal length of lenses L1, L2 and L3

was 200 mm, 40 mm and 150 mm, respectively. The objective was 5X with NA 0.1. The measured magnification was about 21. The light source was provided by SLD with center wavelength  $\lambda=830$  nm and bandwidth  $\Delta\lambda=60$  nm. The theoretical resolution of this system is  $0.61\lambda/NA=5$   $\mu\text{m}$ .

## Section II: Overview of dissertation research

This dissertation research is twofold: (1) to investigate the intrinsic structural and functional biomarkers at the outer retina; (2) to develop the VSD super-resolution method. The VSD can break the diffraction limit for retinal imaging, which allows for reliable investigation of intrinsic structural and functional biomarkers of the retina.

The first kind of intrinsic structural biomarkers studied in this dissertation research are FAF biomarkers. FAF has been helpful for better understanding of eye diseases such as AMD [48, 49], RP [50], multifocal choroiditis and panuveitis [51] and Stargardt disease [52]. FAF signals are originated from choroidal vessels and the retinal pigment epithelium (RPE) [53]. Recent studies show that all-trans retinol and reduced NAD(P)H at the PIO could also contribute to FAF [11-13]. However, whether other retinal layers could emit FAF signals is still unknown. The first specific aim of the dissertation research is to characterize FAF throughout the retinal depths using two-photon excitation. Freshly prepared frog retina specimens in the Ringer solution were used to ensure the physiological condition. Both sliced and flat-mounted retinas were examined. Two-photon excitation and a high NA objective were used to minimize the crosstalk among retinal layers. Two-photon FAF showed that FAF signals exist across multiple functional layers, including the PIO, ONL, OPL, INL, IPL and GCL. This work

implies that FAF that is intended to image the outer retina, i.e., the RPE or PIO, cannot exclude contamination from inner retinal layers. This contamination should be taken into consideration during quantitative analysis of FAF signals, particularly for *in vivo* studies of human, because the NA of the human is low ( $\sim 0.1\text{NA}$ ) [22], which is not able to isolate the signal from the desired layers. The results of the first specific aim are reported in the first article of this dissertation, which has been published by *Biomedical Optical Express* as a full-length original paper.

The FAF can have good image contrast. However, the axial resolution of the *in vivo* FAF is still limited by the low NA of the human eye. OCT, on the other hand, has excellent axial resolution. However, the anatomic correlates to the OCT layers at the outer retina, particularly the presumed ‘IS/OS’ OCT band, are still controversy. The second set of intrinsic structural biomarkers studied in this dissertation research is OCT biomarkers. We compared high-quality OCT images with histological images to identify the origins of the presumed ‘IS/OS’ OCT band. A LS-OCT was constructed to achieve a sub-cellular resolution (lateral:  $\sim 2\ \mu\text{m}$ ; axial:  $\sim 4\ \mu\text{m}$ ) of excised living frog retinas. An electro-optic phase modulator was employed for rapid and vibration-free phase modulation. Comparison of normalized distance measurements between LS-OCT images and histological images revealed that the dominant source of the signal reported as the ‘IS/OS’ OCT band is actually located in the IS. This study can provide valuable information for accurate clinical interpretation of the presumed ‘IS/OS’ OCT band [54]. The results of the second specific aim are reported in the second article of this dissertation, published by *Journal of Biomedical Optics* as a full-length original research paper.

The two aforementioned intrinsic structural biomarkers including FAF and OCT biomarkers are helpful for eye disease diagnosis and studies. However, some functional abnormalities may take place before structural abnormalities become detectable. Therefore, functional biomarkers are critical for early detection of eye diseases. Rods, which detect dim light, are more vulnerable than cones which are for day light vision in the initial stages of some eye diseases such as AMD [3, 35] and RP [36]. Although structural images of rods can be observed using adaptive optics SLO [55-57], evaluation of rod dysfunction is still mostly confined to ERG [58] recording and psychophysical measurement [59]. However, it is still challenging to identify localized rod dysfunctions reliably because of the limited resolution and sensitivity. In the third specific aim of this dissertation research, an intrinsic functional biomarker, transient phototropic adaptation of rod was discovered and explored. After delivered a flash of the oblique stimulus, rods rapidly shifted toward the incident direction of the stimulus on transverse direction. In contrast, such transient phototropism was negligible in cones. Further investigation of such rod-dominant phototropic adaptation promises a new methodology for evaluation of localized rod dysfunction. The results of the third specific aim are reported in the third article of this dissertation, published by *Journal of Biomedical Optics* as a full-length original research paper.

High resolution imaging is important for identifying subtle intrinsic structural and functional biomarkers. However, the transverse resolution of current retinal imaging modalities is all limited by the light diffraction. SIM is a super-resolution method applicable for both autofluorescence and reflection/transmission imaging modalities. However, the conventional SIM uses full field illumination and is not applicable for thick

tissues. Moreover, it requires complex physical manipulation of the sinusoidal illumination generator and may generate phase errors during image reconstruction for moving specimens, i.e., *in vivo* retinal imaging. As a last specific aim of this dissertation research, we developed VSD-based super-resolution imaging systems. VSD can be integrated to confocal scanning systems. In addition, digital sinusoidal modulation is applied in VSD which does not require any physical manipulation illumination generator. We demonstrated the VSD-based super-resolution confocal SLM [18] and OCT [19] with single point raster scanning pattern (Fig. 3C). The raster scanning pattern is slow for the VSD method. To increase speed, VSD is integrated to confocal LSM with line scanning pattern as shown in Fig. 3D. The VSD-based super-resolution SLM with single point raster scanning pattern has been reported in the fourth article of this dissertation, published by *Biomedical Optics Express* as a full-length original research paper. In addition, the VSD-based super-resolution LSM with line scanning pattern are reported in the fifth article of this dissertation, which will be submitted to *Optics Letters* as a full-length original research article. In summary my dissertation includes:

- 1) characterization of intrinsic structural biomarker FAF through all retinal layers, presented in the first article of this dissertation;
- 2) investigation of anatomic correlates to the presumed 'IS/OS' OCT band, presented in the second article of this dissertation;
- 3) exploration of transient phototropic adaptation, an intrinsic functional biomarker, presented in the third article of this dissertation; and
- 4) development of the super-resolution VSD for confocal scanning imaging systems, presented in the fourth and fifth articles of this dissertation.

TWO-PHOTON EXCITED AUTOFLUORESCENCE IMAGING OF FRESHLY  
ISOLATED FROG RETINAS

by

RONGWEN LU, YICHAO LI, TONG YE, CHRISTIANNE STRANG, KENT KEYSER,  
CHRISTINE A. CURCIO, AND XINCHENG YAO

Biomedical Optics Express 2(6), 1494-1503, 2011

Copyright  
2011  
by  
Optical Society of America

Used by permission

Format adapted and errata corrected for dissertation



## **Abstract**

The purpose of this study was to investigate cellular sources of autofluorescence signals in freshly isolated frog (*Rana Pipiens*) retinas. Equipped with an ultrafast laser, a laser scanning two-photon excitation fluorescence microscope was employed for sub-cellular resolution examination of both sliced and flat-mounted retinas. Two-photon imaging of retinal slices revealed autofluorescence signals over multiple functional layers, including the photoreceptor inner segment and outer segment (PIO), outer nuclear layer (ONL), outer plexiform layer (OPL), inner nuclear layer (INL), inner plexiform layer (IPL), and ganglion cell layer (GCL). Using flat-mounted retinas, depth-resolved imaging of individual retinal layers further confirmed multiple sources of autofluorescence signals. Cellular structures were clearly observed at the PIO, ONL, INL, and GCL. At the PIO, the autofluorescence was dominantly recorded from the intracellular compartment of the photoreceptors; while mixed intracellular and extracellular autofluorescence signals were observed at the ONL, INL, and GCL. High resolution autofluorescence imaging clearly revealed mosaic organization of rod and cone photoreceptors; and sub-cellular bright autofluorescence spots, which might relate to connecting cilium, was observed in the cone photoreceptors only. Moreover, single-cone and double-cone outer segments could be directly differentiated.

## **1. Introduction**

Functional evaluation of the retina is important for early detection and treatment evaluation of eye diseases, such as age-related macular degeneration (AMD) [1, 2], diabetic retinopathy (DR) [3, 4], and glaucoma [5, 6]. Previous investigations have

demonstrated that autofluorescence alterations could be used to detect metabolic parameters such as partial pressure of oxygen [7] in biological tissues, and could also act as unique biomarker for selective evaluation of individual cell types such as retinal pigment epithelium (RPE) [8-11]. Without complexities of sample preparation and potential toxicity of exogenous biomarkers, autofluorescence imaging of endogenous fluorophores promises a noninvasive method for functional measurement of the retina [12]. Fundus imaging has revealed autofluorescence from choroidal vessels and the retinal pigment epithelium (RPE) [13]. In principle, fundus autofluorescence imaging may provide high resolution identification of localized retinal dysfunction and thus allow improved disease detection and treatment evaluation. However, multiple types of retinal cells may contribute to fundus autofluorescence. Previous investigations of the retina [14, 15] and other systems [16-18] have revealed that abundant endogenous fluorophores exist in both intracellular and extracellular compartments of biological tissues. Therefore, better understanding of cellular sources of fundus autofluorescence is essential to pursue advanced applications of this imaging technology.

Because of ocular aberrations and complex retinal structure, *in vivo* evaluation of the autofluorescence correlated with individual retinal cell types is challenging. In coordination with adaptive optics to compensate for ocular aberrations, *in vivo* autofluorescence imaging with cellular resolution in transverse direction has recently been demonstrated in macaque and human eyes [19, 20]. However, axial resolution of adaptive optics imaging is limited, typically larger than the thickness of individual functional layers of the retina [21, 22]. Therefore, *in vivo* dissection of the autofluorescence from individual retinal layers is still difficult.

Without the complication of ocular optics, isolated retinas can provide a simple *ex vivo* preparation for quantitative analysis of the contribution of individual retinal layers/cells, including the photoreceptor and inner retinal neurons, to the fundus autofluorescence. Fluorescence microscopy has been used to disclose robust autofluorescence in both outer and inner segments [23, 24]. In principle, two-photon imaging can provide sub-cellular resolution in both transverse and axial directions to characterize autofluorescence in intact retinas. Recently, two-photon autofluorescence imaging of both fixed [14, 15, 25, 26] and unfixed [27-29] *ex vivo* retinal preparations has been demonstrated. However, quantitative two-photon autofluorescence examination of the photoreceptor and inner retinal neurons has not been examined in freshly isolated, i.e., living, retinas. Early investigations suggested that excitation efficiencies and emitted spectra of the fluorophores can be very sensitive to various environmental factors such as partial pressure of oxygen, solvent polarity or viscosity, etc [7, 30]. Therefore, physiological solutions may provide for more accurate measurement of autofluorescence associated with live tissue.

The purpose of this study is to quantify two-photon excited autofluorescence signals from photoreceptors and inner neurons in freshly isolated retinas. In oxygenated Ringer's solution, freshly isolated retinas are viable and excitable, at least for a few hours. We have recently using freshly isolated retinas, including both sliced [31] and flat-mounted [32-39] retinas, to investigate stimulus-evoked retinal neural activities. In this study, the same retinal preparation, i.e., isolated but living retinas, to characterize cellular sources of retinal autofluorescence. In the freshly isolated retinas, robust autofluorescence signals were consistently observed across whole retinal depth, i.e., the

photoreceptor inner segment and outer segment (PIO), outer nuclear layer (ONL), outer plexiform layer (OPL), inner nuclear layer (INL), inner plexiform layer (IPL), and ganglion cell layer (GCL). Characteristic autofluorescence patterns were imaged over different retinal layers, and autofluorescence signals of individual retinal layers were quantitatively compared.

## 2. Method

### 2.1. Retinal Preparation

Isolated leopard (*Rana Pipiens*) frog retinas were used for the experiments. Isolated retinas provide a simple preparation to investigate cellular sources of autofluorescence in the retina without the complications associated with the presence of other ocular tissues and eye movements. Both sliced and flat-mounted retinas were used for this study. A retinal slice opens a cross-section of the retina, and thus allows simultaneous monitoring of autofluorescence signal from the photoreceptor outer segments to inner retina; while a flat-mounted retina allows depth-resolved imaging of individual retinal layers. The experimental procedures were approved by the Institutional Animal Care and Use Committee of University of Alabama at Birmingham. Details of the preparation of flat-mounted retinas [34] and retinal slices [31] have been previously reported. Briefly, retinal dissection was conducted in a dark room with dim red illumination. The frog was sacrificed by rapid decapitation and double pithing before the eyes were enucleated. The eyeball was hemisected below the equator with fine scissors to remove the lens and anterior structures before separating the retina from the retinal pigment epithelium. The isolated retina was directly used for flat-mounted imaging, or cut into ~200  $\mu\text{m}$  slices for

cross section imaging of the retina. During the recording, the retina was immersed in oxygenated Ringer's solution containing (in mM) [40]: 110 NaCl, 2.5 KCl, 1.6 MgCl<sub>2</sub>, 1.0 CaCl<sub>2</sub>, 22 NaHCO<sub>3</sub>, and 10 D-glucose.

## *2.2. Experimental setup*

Figure 1 shows a schematic diagram of the experimental setup. Equipped with an ultrafast mode-locked Ti: Sapphire laser (Chameleon, Coherent Inc), a laser scanning multi-photon microscope (Prairie Technologies) was used for two-photon excited autofluorescence imaging of freshly isolated retinas. During the recording, 720 nm laser pulses were selected for autofluorescence excitation of both flat-mounted retinas and retinal slices. Similar laser wavelength has been used for two-photon autofluorescence investigation of ocular tissues [14]. The width of each laser pulse was <140 fs, and the repetition rate was 90 MHz. The averaged laser power was adjusted between 2~10 mW which was measured at the specimen position and did not result in obvious damage of the retinal tissues. A high sensitivity photomultiplier tubes (PMT, H7422P, Hamamatsu Photonics) was employed for autofluorescence recording. A typical imaging frame (512 x 512 pixels) period used in the experiments was ~6.8s, which corresponded to a 25.2  $\mu$ s pixel dwell time (i.e. laser exposure time of each pixel).

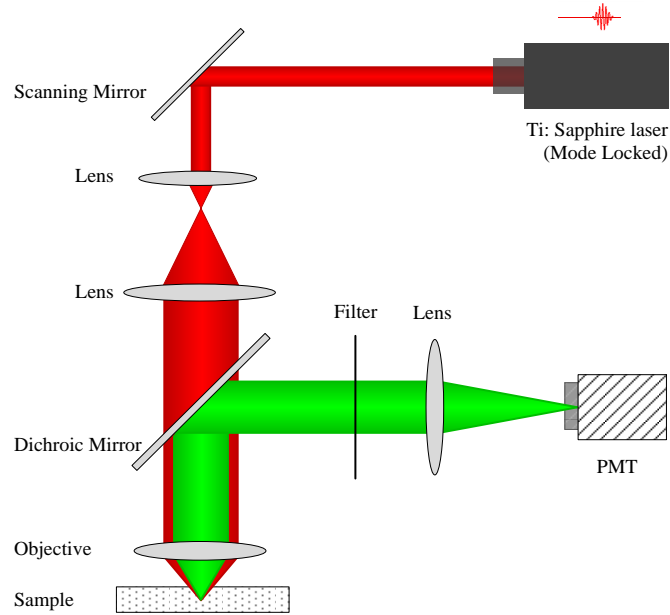


Fig. 1. Schematic diagram of the experimental setup for two-photon imaging of the frog retina. A mode-locked Ti: Sapphire laser (Chameleon, Coherent Inc) was used to provide excitation light (720 nm). At the dichroic mirror, the long-wavelength 720 nm excitation light (red rays) was passed through and the short-wavelength emission light (green rays) was reflected. A band-pass (450-550 nm) filter was placed in front of the photomultiplier tube (PMT).

### 3. Results

#### 3.1. Autofluorescence imaging of retinal slices

The first step of this study was to verify multiple sources of autofluorescence signals in the retina. We started the experiments using freshly isolated frog retinal slices. Fig. 2A represents conventional transmission image; while Fig. 2B represents two-photon excited autofluorescence image (Fig. 2B) of retinal slices. Fig. 2C shows averaged autofluorescence signal at each depth of the retina shown in Fig. 2B. High resolution two-

photon imaging disclosed robust autofluorescence from multiple retinal layers, including PIO, ONL, OPL, INL, IPL and GCL, with sub-cellular spatial resolution. Retinal slice experiments indicated that the 720 nm pulse laser can provide autofluorescence excitation of both photoreceptors and inner retinal cells. In comparison with the conventional transmission imaging (Fig. 2A), the two-photon autofluorescence measurement (Fig. 2B) showed significantly improved image contrast, allowing direct observation of single cells (green arrowheads in Fig. 2B) at individual functional layers, and also fiber like Müller glial cells that initiated from the GCL and penetrated into inner retinal layers (red arrowheads in Fig. 2B). Although autofluorescence signals were consistently observed throughout the retina, the signal efficiency of the outer retina, e.g., PIO, was significantly higher than that of inner retinal layers (Fig. 2C).

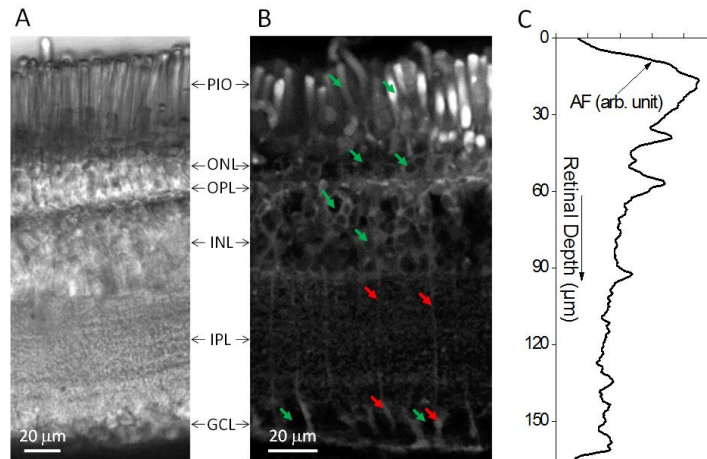


Fig. 2. Autofluorescence imaging of retinal slice. (A) Transmission image of a frog retinal slice. During the recording, the retinal slice was continuously illuminated by an infrared (800-1000 nm) light. The PIO, ONL, OPL, INL, IPL, GCL could be directly differentiated. (B) Representative two-photon fluorescence image of frog retinal slices. The excitation light was set at 720 nm, and the average power is ~ 5 mW. In this image, single cellular structures (green arrowheads) were clearly observed in the PIO, ONL,

INL, and GCL. Individual Müller glial cells (red arrowheads) were observed. (C) Averaged autofluorescence (AF) signal at each depth of the retinal slice shown in Fig. 2B.

### *3.2. Autofluorescence imaging of flat-mounted retinas*

The second phase of this study was to test the feasibility of depth-resolved imaging of two-photon excited autofluorescence in flat-mounted retinas, i.e., isolated but living retinas. Fig. 3A-F represents two-photon images of the PIO, ONL, OPL, INL, IPL, and GCL, respectively. Fig. 3G shows a cross-section scan, from the GCL to the PIO, of the flat-mounted retina. As shown in Fig. 3A, PIO autofluorescence was dominantly localized at intracellular compartment of individual photoreceptors; while ONL, INL and GCL autofluorescence images were dominated by extracellular signals, although mixed intracellular and extracellular patterns were observed. Different brightness of individual cells, which might reflect variable cell types, was observed. Bright spots were observed in the OPL and IPL (Fig. 3C and 3E). Mosaic pattern of rod and cone photoreceptors was clearly observed in Fig. 3A. The rod (blue arrowheads in Fig. 3A) and cone (red arrowheads in Fig. 3A) photoreceptors could be separated simply based on their cellular sizes. In general, the outer segment diameter of frog rods ( $\sim 5\text{-}8\ \mu\text{m}$ ) is larger than that of the cones ( $\sim 1\text{-}3\ \mu\text{m}$ ) [41, 42]. Moreover, single and double cones could be further separated (green arrowheads in Fig. 4B). In overall, the cones show brighter autofluorescence than that of the rods (Fig. 3H).



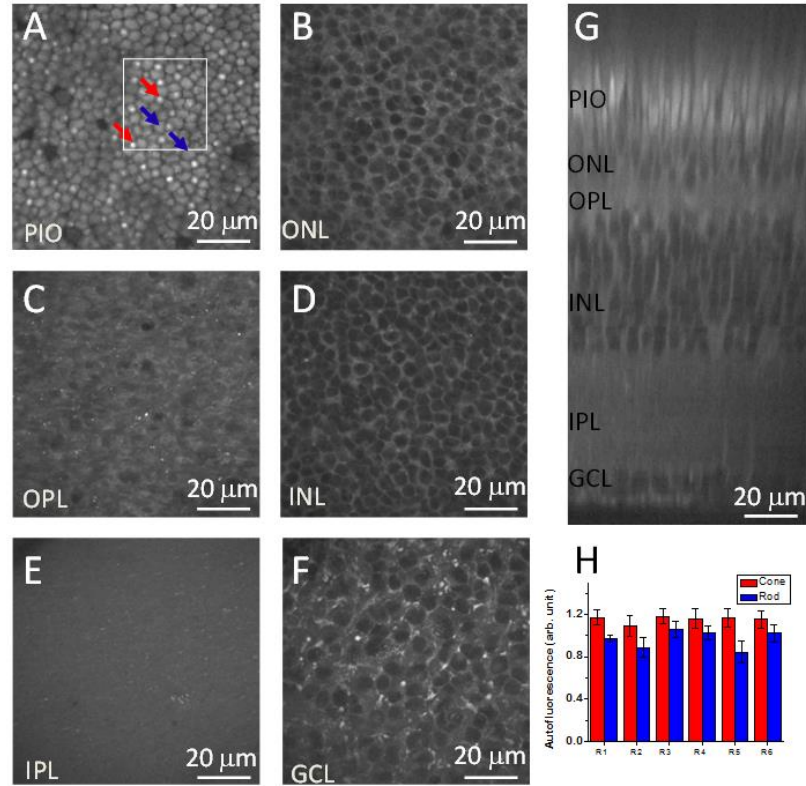


Fig. 3. Two-photon excited autofluorescence imaging of the flat-mounted retina. The 720 nm excitation light was delivered from the GCL side, i.e., the GCL side faced to the objective in Fig. 1. Two-photon images of the PIO (A), ONL (B), OPL (C), INL (D), IPL (E), and GCL (F), were collected with identical excitation power of  $\sim 10$  mW. The white square in A marks the region of interest shown in greater detail in Figure 4. (G) Depth-resolved scan, i.e., a cross-section, of a line area of the flat-mounted retina. (H) Comparison of rod and cone autofluorescence recorded from 6 retinal preparations R1-6. For each retina, 10 rods and 10 cones were randomly selected for average calculations of the rod and cone autofluorescence. The line bars indicate standard deviation.

Fig. 4A shows enlarged PIO illustration of a sub-image marked by the white square in Fig. 3A. From Fig. 4A, we observed that the rod (blue arrowheads) autofluorescence was relatively homogenous at the cellular level; while distinct bright

spots were frequently observed in the cones (red arrowheads). In order to demonstrate the repeatability of the experiment, Fig. 4B shows another example of autofluorescence image of the rod and cone mosaics. The peak value, i.e., the pixel value with highest brightness, of individual cones (Fig. 4C) was significantly ( $\sim 1.7$  times) larger than the average cone value; while the peak value of individual rods (Fig. 4D) was only slightly ( $\sim 1.2$  times) larger than the average rod value.

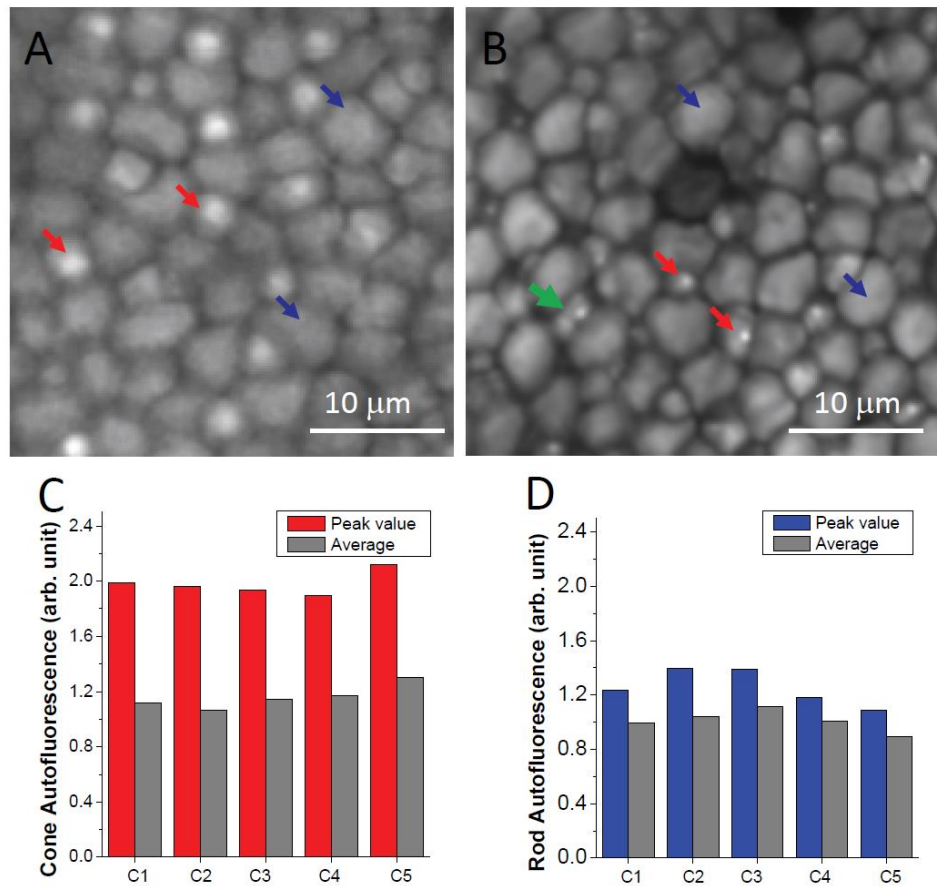


Fig. 4. Autofluorescence comparison between rods and cones. (A) Enlarged PIO illustration of a sub-image marked by the white square in Fig. 3A. This image revealed that the rod (blue arrowheads) autofluorescence was relatively homogenous at the cellular level; while a bright spot with sub-cellular structure was frequently observed in the cones (red arrowheads). (B) Another example of autofluorescence image of the rod and cone

mosaics. Bright autofluorescence spots were consistently observed in the cones (red arrowheads) and double cones (green arrowhead). (C) and (D) show peak and average values of 5 representative cones and 5 rods, respectively.

In order to further characterize the rod and cone autofluorescence, Fig. 5 shows depth-resolved image sequence of the PIO with a depth interval of 2  $\mu\text{m}$ . During the recording, the transverse scanning step, i.e., pixel resolution was improved to 0.3  $\mu\text{m}$  (compared to the 0.5  $\mu\text{m}$  pixel size used for the experiments shown in Fig. 3 and Fig. 4). In order to minimize signal cross-talk of adjacent rods and cones, the excitation power was lowered to ~5 mW (compared to the 10 mW used for the experiments shown in Fig. 3). High resolution two-photon imaging consistently revealed bright autofluorescence spots in the cones. Depth-resolved recording indicated that the bright spots were localized primarily at  $z = 16\text{-}30 \mu\text{m}$ , relative to the PIO side retinal surface.

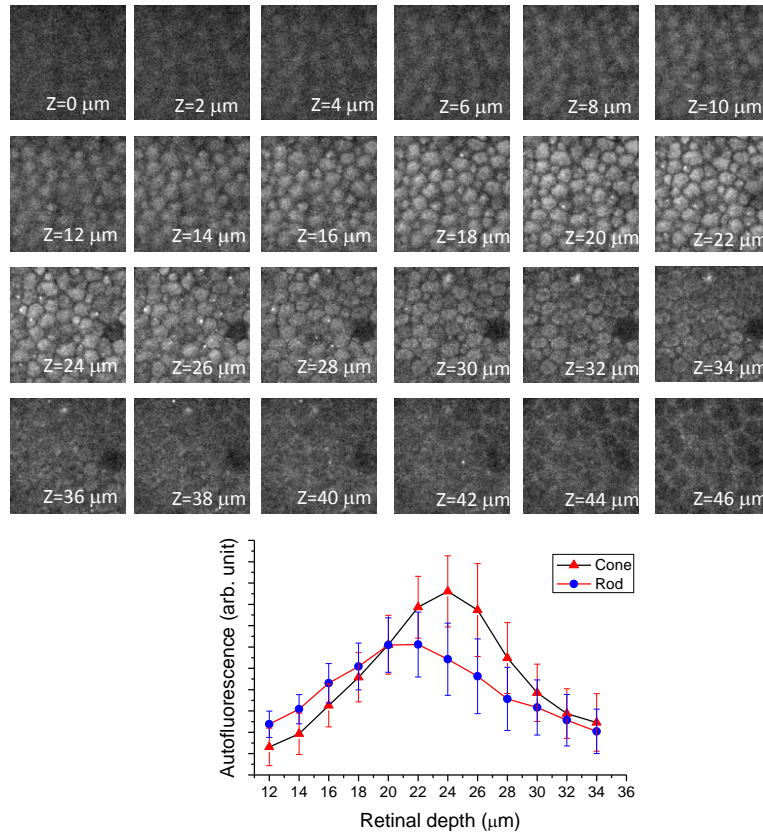


Fig. 5. Quantitative analysis of PIO autofluorescence. Top panel shows depth-resolved imaging of the PIO autofluorescence. The images were collected with 2  $\mu\text{m}$  depth interval and 0.3  $\mu\text{m}$  pixel size. The excitation power was  $\sim 5$  mW. A bright autofluorescence spot was frequently observed in the cone. Primary bright spots were localized at  $z = 16\text{-}30$   $\mu\text{m}$  relative to the PIO side retinal surface. Bottom panel is quantitative comparison of autofluorescence between rods and cones at  $z = 12\text{-}34$   $\mu\text{m}$ . At each depth, 6 rods and 6 cones were used for averaging. The line bars indicate standard deviation.

### 3.3. Comparison of autofluorescence signals in retinal slices and flat-mounted retinas.

In retinal slices, the autofluorescence sensitivity of the PIO was significantly

higher than that of inner retinal layers (Fig. 2B and 2C). However, in flat-mounted retinas, relative fluorescence sensitivity, i.e., signal contrast to other retinal layers, of the PIO was compromised (Fig. 3A-H)). Fig. 6 shows autofluorescence averages of the PIO, ONL, OPL, INL, IPL and GCL in retinal slices and flat-mounted retinas.

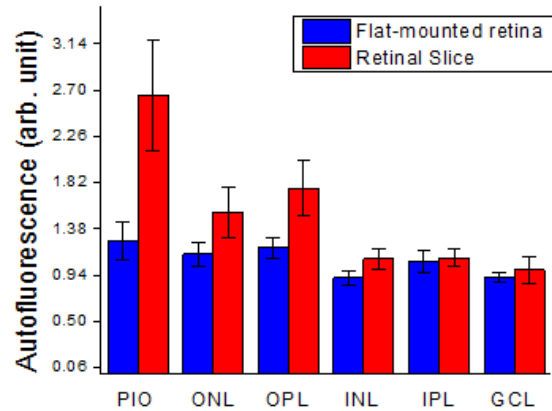


Fig. 6. Averaged autofluorescence of the PIO, ONL, OPL, INL, IPL and GCL. 6 retinal slices and 6 flat-mounted retinas were used for the average. Red and blue bars show the signals recorded from retinal slices and flat-mounted retinas, respectively. The line bars indicate standard deviation.

#### 4. Discussion

In summary, two-photon excited autofluorescence imaging of freshly isolated frog retinas was conducted. Freshly isolated retinas could be maintained in a physiological environment that can minimize the differences from *in situ* metabolic status of living retinas. High resolution examination of the freshly isolated retinas verified multiple cellular sources, including the PIO, ONL, OPL, INL, IPL, and GCL of retinal autofluorescence. Both retinal slices and flat-mounted retinas were used for this study.

Two-photon image of the retinal slice revealed that signal efficiency of the PIO was significantly higher than that of inner retinal layers, although autofluorescence signals were consistently observed over the whole thickness of the retina (Fig. 2C). In contrast, autofluorescence sensitivity of the PIO was compromised in flat-mounted retinas (Fig. 3A-H). This might result from reduced light efficiency due to light scattering, absorption, and aberration, in the flat-mounted retinal preparation.

At the PIO, autofluorescence was dominantly confined to the intracellular compartment. High-resolution imaging revealed the mosaic organization of rod and cone photoreceptors, and single and double cones could be identified (Figs. 3 and Fig. 4). Autofluorescence distribution in the rod outer segment was relatively homogenous; while sub-cellular bright spots with light intensity well above average level were revealed in the cone outer segment (Figs. 3 and 4). Early investigations suggested that autofluorescence signals of outer and inner photoreceptor segments were related to all-trans retinol and nicotinamide adenine dinucleotide phosphate (NADPH), respectively [14, 23, 26]. However, the observed bright autofluorescence spots in cones might not, at least not completely, result from the all-trans retinol. These bright spots were frequently observed at the periphery of the cones (Fig. 4). We speculate that the bright autofluorescence spots might be related to the connecting cilium (CC), which links the inner segments to the outer segments. It is well established that the CC constitutes a sort of highway for proteins, such as rhodopsin, travelling to and from the outer segment [43]. These proteins might contribute to the observed bright autofluorescence spots by producing autofluorescence signals directly. Alternatively, the CC might act as a light waveguide to affect the excitation and collection efficiency of all-trans retinol in sub-cellular locations,

relative to the CC axis, in the cone outer segments. Early investigations indicated that the length of the cone outer segment is 7-13  $\mu\text{m}$  [41], which is consistent with the observed depth range ( $\sim 14 \mu\text{m}$ , i.e.,  $z = 16\text{-}30 \mu\text{m}$  in Fig. 5) of the bright autofluorescence spots.

In other retinal layers, both intracellular and extracellular autofluorescence signals were observed. Cellular structures were clearly observed at the ONL, INL, and GCL, while bright autofluorescence spots, which might relate to individual nerve terminals, were observed in the OPL and IPL. According to previous investigations with retina and other biological tissues, the observed autofluorescence might result from reduced nicotinamide adenine dinucleotide (NADH) and reduced nicotinamide adenine dinucleotide phosphate (NADPH), collectively referred to as NAD(P)H, and the oxidized forms of flavoproteins [14]. Most of the NAD(P)H fluorescence originates from the mitochondria and can serve as the basis for redox fluorometry. Therefore, pyridine nucleotides and flavins not only can provide morphological contrast, but may also act as valuable biomarkers for functional imaging of metabolic activity of living tissues [14].

In conclusion, two-photon imaging of freshly isolated retinas revealed multiple, intracellular and extracellular, sources of endogenous fluorophores that were simultaneously excited by the constant-wavelength (720 nm) light from a pulsed laser. Because autofluorescence signals originated from both outer and inner retinal layers, signal specificity of fundus autofluorescence imaging is limited and cross-contamination among different cell types is not negligible. Further investigations are necessary to understand biophysical and biochemical mechanisms of retinal autofluorescence better. We are currently pursuing further experiments with mammalian retinas that have a closer similarity with human retinas to verify the autofluorescence inhomogeneity observed in

the frog photoreceptors, and to characterize the autofluorescence mechanisms. In coordination with variable controls of excitation wavelength and spectral measurement, advanced investigations of retinal autofluorescence in the retina of animal models may provide insight in the development of a new imaging methodology for selective evaluation of the rod, cone, and inner retinal neurons, which may lead to better study and improved diagnosis of AMD [1, 2], diabetic retinopathy (DR) [3, 4], and glaucoma [5, 6], retinitis pigmentosa (RP) [44], and other eye diseases that can produce functional damages of retinal cells.

### **Acknowledgments**

This research is supported by the Dana Foundation (Brain and Immuno-Imaging Grant program), the Eyesight Foundation of Alabama, the National Institutes of Health (NIH) (5R21RR025788-02 and 1R21EB012264-01A1), and the National Science Foundation (CBET-1055889). The two-photon fluorescence images were acquired in the Neuroimaging Core, which was supported by NIH Neuroscience Blueprint Core Grant NS57098 to the University of Alabama at Birmingham.

### **Reference**

1. G. R. Jackson, C. Owsley, and C. A. Curcio, "Photoreceptor degeneration and dysfunction in aging and age-related maculopathy," *Ageing Res. Rev.* **1**, 381-396 (2002).
2. R. E. Hogg, and U. Chakravarthy, "Visual function and dysfunction in early and late age-related maculopathy," *Prog. Retin. Eye. Res.* **25**, 249-276 (2006).
3. B. Meyer-Rusenber, M. Pavlidis, T. Stupp, and S. Thanos, "Pathological changes in human retinal ganglion cells associated with diabetic and hypertensive retinopathy," *Graefes Arch. Clin. Exp. Ophthalmol.* **245**, 1009-1018 (2007).



4. Y. Qin, G. Xu, and W. Wang, "Dendritic abnormalities in retinal ganglion cells of three-month diabetic rats," *Curr. Eye Res.* **31**, 967-974 (2006).
5. R. S. Harwerth, and H. A. Quigley, "Visual field defects and retinal ganglion cell losses in patients with glaucoma," *Arch. Ophthalmol.* **124**, 853-859 (2006).
6. R. W. Nickells, "Ganglion cell death in glaucoma: from mice to men," *Vet. Ophthalmol.* **10** Suppl 1, 88-94 (2007).
7. B. Chance, "Pyridine nucleotide as an indicator of the oxygen requirements for energy-linked functions of mitochondria," *Circ. Res.* **38**, I31-38 (1976).
8. S. Bearely, A. A. Khanifar, D. E. Lederer, J. J. Lee, J. H. Ghodasra, S. S. Stinnett, and S. W. Cousins, "Use of Fundus Autofluorescence Images to Predict Geographic Atrophy Progression," *Retina* **31**, 81-86 (2011).
9. F. C. Delori, C. K. Dorey, G. Staurenghi, O. Arend, D. G. Goger, and J. J. Weiter, "In-Vivo Fluorescence of the Ocular Fundus Exhibits Retinal-Pigment Epithelium Lipofuscin Characteristics," *Invest. Ophthalmol. Vis. Sci.* **36**, 718-729 (1995).
10. O. La Schiazza, and J. F. Bille, "High-speed two-photon excited autofluorescence imaging of ex vivo human retinal pigment epithelial cells toward age-related macular degeneration diagnostic," *J. Biomed. Opt.* **13**, 064008 (2008).
11. D. Schweitzer, S. Schenke, M. Hammer, F. Schweitzer, S. Jentsch, E. Birckner, W. Becker, and A. Bergmann, "Towards metabolic mapping of the human retina," *Microsc. Res. Tech.* **70**, 410-419 (2007).
12. Y. Imanishi, K. H. Lodowski, and Y. Koutalos, "Two-photon microscopy: Shedding light on the chemistry of vision," *Biochemistry* **46**, 9674-9684 (2007).
13. J. C. Hwang, D. Y. Kim, C. L. Chou, and S. H. Tsang, "Fundus Autofluorescence, Optical Coherence Tomography, and Electroretinogram Findings Choroidal Sclerosis," *Retina* **30**, 1095-1103 (2010)
14. A. Bindewald-Wittich, M. Han, S. Schmitz-Valckenberg, S. R. Snyder, G. Giese, J. F. Bille, and F. G. Holz, "Two-photon-excited fluorescence imaging of human RPE cells with a femtosecond Ti : sapphire laser," *Invest. Ophthalmol. Vis. Sci.* **47**, 4553-4557 (2006).
15. Y. Hagiwara, K. Hattori, T. Aoki, H. Ohgushi, and H. Ito, "Autofluorescence assessment of extracellular matrices of a cartilage-like tissue construct using a fluorescent image analyser," *J. Tissue Eng. Regen. Med.* **5**, 163-168 (2011).
16. H. Hillman, T. Hussain, and P. Sartory, "Autofluorescence of isolated unfixed rabbit Deiters' neurons and surrounding neuroglial clamps," *Experientia* **29**, 1113-1115 (1973).

17. K. C. Reinert, R. L. Dunbar, W. C. Gao, G. Chen, and T. J. Ebner, "Flavoprotein autofluorescence imaging of neuronal activation in the cerebellar cortex in vivo," *Journal of Neurophysiology* **92**, 199-211 (2004).
18. J. I. Morgan, J. J. Hunter, W. H. Merigan, and D. R. Williams, "The reduction of retinal autofluorescence caused by light exposure," *Invest. Ophthalmol. Vis. Sci.* **50**, 6015-6022 (2009).
19. J. I. W. Morgan, A. Dubra, R. Wolfe, W. H. Merigan, and D. R. Williams, "In Vivo Autofluorescence Imaging of the Human and Macaque Retinal Pigment Epithelial Cell Mosaic," *Invest. Ophthalmol. Vis. Sci.* **50**, 1350-1359 (2009).
20. K. Grieve, and A. Roorda, "Intrinsic signals from human cone photoreceptors," *Invest. Ophthalmol. Vis. Sci.* **49**, 713-719 (2008).
21. F. Romero-Borja, K. Venkateswaran, A. Roorda, and T. Hebert, "Optical slicing of human retinal tissue in vivo with the adaptive optics scanning laser ophthalmoscope," *Appl. Opt.* **44**, 4032-4040 (2005).
22. C. H. Chen, E. Tsina, M. C. Cornwall, R. K. Crouch, S. Vijayaraghavan, and Y. Koutalos, "Reduction of all-trans retinal to all-trans retinol in the outer segments of frog and mouse rod photoreceptors," *Biophys. J.* **88**, 2278-2287 (2005).
23. Q. Q. Wu, C. H. Chen, and Y. Koutalos, "All-trans retinol in rod photoreceptor outer segments moves unrestrictedly by passive diffusion," *Biophys J* **91**, 4678-4689 (2006).
24. M. Han, A. Bindewald-Wittich, F. G. Holz, G. Giese, M. H. Niemz, S. Snyder, H. Sun, J. Y. Yu, M. Agopov, O. La Schiazza, and J. F. Bille, "Two-photon excited autofluorescence imaging of human retinal pigment epithelial cells," *J. Biomed. Opt.* **11**, 010501 (2006).
25. M. Han, G. Giese, S. Schmitz-Valckenberg, A. Bindewald-Wittich, F. G. Holz, J. Y. Yu, J. F. Bille, and M. H. Niemz, "Age-related structural abnormalities in the human retina-choroid complex revealed by two-photon excited autofluorescence imaging," *J. Biomed. Opt.* **12**, 024012 (2007).
26. J. M. Bueno, E. J. Gualda, and P. Artal, "Adaptive optics multiphoton microscopy to study ex vivo ocular tissues," *J. Biomed. Opt.* **15**, 066004 (2010).
27. E. J. Gualda, J. M. Bueno, and P. Artal, "Wavefront optimized nonlinear microscopy of ex vivo human retinas," *J. Biomed. Opt.* **15**, 026007 (2010).
28. L. L. Zhao, J. L. Qu, D. N. Chen, and H. B. Niu, "Layered-resolved autofluorescence imaging of photoreceptors using two-photon excitation," *J. Biomedical Science and Engineering* **2**, 363-365 (2009).

29. P. Yan, A. Xie, M. Wei, and L. M. Loew, "Amino(oligo)thiophene-based environmentally sensitive biomembrane chromophores," *J. Org. Chem.* **73**, 6587-6594 (2008).
30. Y. C. Li, C. Strang, F. R. Amthor, L. Liu, Y. G. Li, Q. X. Zhang, K. Keyser, and X. C. Yao, "Parallel optical monitoring of visual signal propagation from the photoreceptors to the inner retina layers," *Opt. Lett.* **35**, 1810-1812 (2010).
31. Y. B. Zhao, and X. C. Yao, "Intrinsic optical imaging of stimulus-modulated physiological responses in amphibian retina," *Opt. Lett.* **33**, 342-344 (2008).
32. Q. X. Zhang, J. Y. Wang, L. Liu, and X. C. Yao, "Microlens array recording of localized retinal responses," *Opt. Lett.* **35**, 3838-3840 (2010).
33. X. C. Yao, and Y. B. Zhao, "Optical dissection of stimulus-evoked retinal activation," *Opt. Express* **16**, 12446-12459 (2008).
34. Y. G. Li, Q. X. Zhang, L. Liu, F. R. Amthor, and X. C. Yao, "High spatiotemporal resolution imaging of fast intrinsic optical signals activated by retinal flicker stimulation," *Opt. Express* **18**, 7210-7218 (2010).
35. Y. G. Li, L. Liu, F. Amthor, and X. C. Yao, "High-speed line-scan confocal imaging of stimulus-evoked intrinsic optical signals in the retina," *Opt. Lett.* **35**, 426-428 (2010).
36. X. C. Yao, A. Yamauchi, B. Perry, and J. S. George, "Rapid optical coherence tomography and recording functional scattering changes from activated frog retina," *Appl. Opt.* **44**, 2019-2023 (2005).
37. X. C. Yao, and J. S. George, "Near-infrared imaging of fast intrinsic optical responses in visible light-activated amphibian retina," *J. Biomed. Opt.* **11**, 064030 (2006).
38. X. C. Yao, and J. S. George, "Dynamic neuroimaging of retinal light responses using fast intrinsic optical signals," *Neuroimage* **33**, 898-906 (2006).
39. P. A. Sieving, K. Murayama, and F. Naarendorp, "Push-pull model of the primate photopic electroretinogram: a role for hyperpolarizing neurons in shaping the b-wave," *Vis. Neurosci.* **11**, 519-532 (1994).
40. S. E. Nilsson, "An Electron Microscopic Classification of the Retinal Receptors of the Leopard Frog (*Rana Pipiens*)," *J. Ultrastruct. Res.* **10**, 390-416 (1964).
41. P. A. Liebman, and G. Entine, "Visual pigments of frog and tadpole (*Rana pipiens*)," *Vision Res.* **8**, 761-775 (1968).
42. V. Ramamurthy, and M. Cayouette, "Development and disease of the photoreceptor cilium," *Clinical Genetics* **76**, 137-145 (2009).

43. A. D. Marmorstein, L. Y. Marmorstein, H. Sakaguchi, and J. G. Hollyfield, "Spectral profiling of autofluorescence associated with lipofuscin, Bruch's Membrane, and sub-RPE deposits in normal and AMD eyes," *Invest. Ophthalmol. Vis. Sci.* **43**, 2435-2441 (2002).
44. T. Wakabayashi, M. Sawa, F. Gomi, and M. Tsujikawa, "Correlation of fundus autofluorescence with photoreceptor morphology and functional changes in eyes with retinitis pigmentosa," *Acta. Ophthalmol.* **88**, e177-183 (2010).

INVESTIGATION OF THE HYPER-REFLECTIVE INNER/OUTER SEGMENT  
BAND IN OPTICAL COHERENCE TOMOGRAPHY OF LIVING FROG RETINA

by

RONGWEN LU, CHRISTINE A. CURCIO, YOUWEN ZHANG, QIUXIANG ZHANG,  
STEVEN J. PITTLER, DUSANKA DERETIC AND XINCHENG YAO

Journal of Biomedical Optics 17 (6), 0605041-0605043

Copyright  
2012  
by  
SPIE

Used by permission

Format adapted and errata corrected for dissertation

## **Abstract**

This study is to test anatomic correlates, including connecting cilium (CC) and inner segment (IS) ellipsoid, to the hyper-reflective band visualized by optical coherence tomography (OCT) and commonly attributed to the photoreceptor inner/outer segment (IS/OS) junction. A line-scan OCT (LS-OCT) was constructed to achieve sub-cellular resolution (lateral:  $\sim 2 \mu\text{m}$ ; axial:  $\sim 4 \mu\text{m}$ ) of excised living frog retinas. An electro-optic phase modulator was employed for rapid and vibration-free phase modulation. Comparison of normalized distance measurements between LS-OCT images and histological images revealed that the dominant source of the signal reported as the 'IS/OS' OCT band actually originates from the IS.

## **Body of the paper**

Given the excellent capability to identify morphological changes at individual functional layers of the retina, optical coherence tomography (OCT) has increasing application in eye disease detection [1]. In-depth understanding of anatomic sources of the OCT signal is essential for accurate interpretation of clinical outcomes, and is valuable for instrument optimization to improve imaging sensitivity and selectivity. Early studies have disclosed four hyper-reflective OCT bands at the outer retina, i.e. photoreceptor side. Anatomic sources of these four OCT bands have been typically attributed as follows: first (1<sup>st</sup>) band at the outer limiting membrane (OLM); second (2<sup>nd</sup>) band at the photoreceptor inner/outer-segment (IS/OS) junction; third (3<sup>rd</sup>) band at the posterior tip of the OS; and fourth (4<sup>th</sup>) band at the retinal pigment epithelium (RPE) [2]. Anatomic correlates of the 2<sup>nd</sup> band remains controversial. The 2<sup>nd</sup> OCT band is widely

attributed to the IS/OS junction, which cell biologists consider the connecting cilium (CC) between these structures. However, comparative alignment of OCT bands with an anatomically correct model of the outer retina suggested an alternative correlate, i.e., the IS ellipsoid [3], to the 2<sup>nd</sup> OCT band. Previous investigation has indicated that the physiological condition may affect the 2<sup>nd</sup> OCT band recording [4]. Therefore, freshly isolated living retinas were used for OCT imaging.

Leopard (*Rana Pipiens*) frog was selected for this study. Large photoreceptors (cone: ~3  $\mu\text{m}$  and rod: ~6  $\mu\text{m}$ ) [5] of the frog enabled accurate OCT recording at sub-cellular resolution. The experimental procedures were approved by the Institutional Animal Care and Use Committee of the University of Alabama at Birmingham. Without complications of ocular aberrations and signal contamination of other ocular tissues, isolated retinas provided a simple preparation to allow high resolution OCT characterization of the retina. Details of the preparation procedures of freshly isolated living retinas, which have been used to investigate stimulus-evoked retinal neural activities, have been previously reported [6, 7]. During the OCT imaging, the isolated retina was immersed in oxygenated Ringer's solution to maintain its viability.

In order to achieve sub-cellular resolution in both lateral and axial directions, a rapid line-scan OCT (LS-OCT) was developed. The LS-OCT combined technical merits of our recently demonstrated electro-optic phase modulator (EOPM) based functional OCT [6] and line-scan confocal microscopy [7]. Figure 1 shows a simplified diagram of the LS-OCT. In this system, a near infrared superluminescent laser diode (SLD-35-HP, Superlum), with center wavelength  $\lambda=830$  nm and bandwidth  $\Delta\lambda=60$  nm, was used for light illumination. A water immersion objective (10X, NA=0.3) was applied for OCT

imaging. The lateral resolution of the system was estimated at  $\sim 2 \mu\text{m}$  ( $0.61\lambda/\text{NA}$ ), and the axial resolution of the LS-OCT was  $\sim 4 \mu\text{m}$  ( $0.44\lambda^2/n\Delta\lambda$ , where refractive index  $n$  of the sample was assumed  $\sim 1.4$ ).

In the illumination path (optics above the beam splitter BS, Fig.1a), a cylindrical lens CL1 was employed to condense the collimated SLD light in one dimension to produce a focused line illumination which was imaged at the retina through lenses L3, L4, L5 and the objective OB. The long axis of the focused line was parallel to the y-axis in the OCT image (Fig. 2a). The active area of the high-speed (70,000 lines/s) linear camera (spL2048-140k, Basler Sprint) was conjugated to the focused line illumination. The line-sensor (1 x 2048 pixels,  $10 \mu\text{m} \times 10 \mu\text{m}$ ) of the linear camera naturally acted as a spatial-filter to reject out-of-focus light. Thus, a LS confocal mechanism was achieved to reduce background light and therefore maximize effective OCT contrast and dynamic range.

In the reference path (optics below the BS, Fig.1a), another cylindrical lens CL2 was used to convert the focused light back to a collimated light beam before entering the EOPM (Model 350-50, Conoptics) that was used to generate rapid vibration- and inertia-free phase modulation [6]. A four-step phase-shifting strategy was employed to retrieve OCT images [8]. The glass block in the reference arm was used to compensate for optical dispersion of the sample beam. Fig. 1b shows side view of the illumination and reference paths (dashed square in Fig. 1a). In the side view, the cylindrical lenses CL1 and CL2 acted as a pair of glass plates.

Our custom-designed LS-OCT provided both en-face and B-scan recording capabilities. The galvo scanning mirror (GVS001, Thorlabs) could provide rapid en-face (Fig. 2a) imaging up to 400 Hz; while the motorized sample platform (Z825B, Thorlabs)



could scan in the z-direction to achieve B-scan recording (Fig. 2b) of the cross-section of flat-mount retinas.

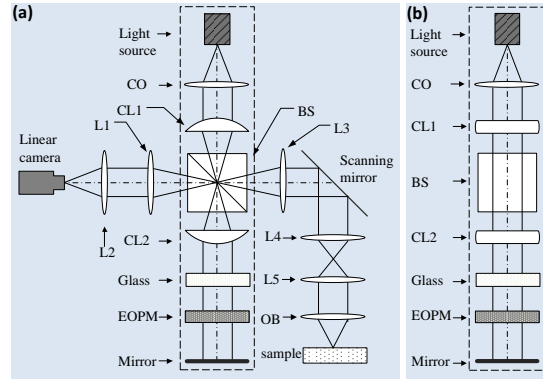


Fig. 9. Optical setup of LS-OCT. (a) Schematic diagram of the LS-OCT. BS: beam splitter; CO: collimator, L1~L5: lenses; OB: objective; CL1 and CL2: cylindrical lenses. The focal length of CL1, CL2, L1~L5 was 40mm, 40mm, 40mm, 80mm, 80mm, 40mm, and 75mm, respectively. (b) The side view of the optical geometry of the illumination and reference paths (dashed square in a).

Figure 2 shows representative en-face and B-scan images recorded using the LS-OCT. During the recording, the photoreceptors were upward, i.e., facing to the objective, to improve image quality of the outer retina. Given the sub-cellular resolution, the en-face image (Fig. 2a) revealed individual photoreceptors. B-scan image (Fig. 2b) disclosed individual layers from the photoreceptor to inner retina. After adapting band nomenclature used in high resolution OCT of human retina to frog retina[2], we labeled individual layers. As shown in Fig. 2b, the OS, ‘IS/OS’ (presumed), OLM, OPL, inner plexiform layer (IPL), nerve fiber layer (NFL) were hyper-reflective; while the outer nuclear layer (ONL), inner nuclear layer (INL) and ganglion cell layer (GCL) were hypo-reflective. The bright ‘IS/OS’ band was bumpy in the high resolution OCT image. In order to achieve better visualization of individual OCT bands, Fig. 2c shows an averaged

cross-section image over 120  $\mu\text{m}$  (200 B-scan images, with 0.6  $\mu\text{m}$  recording interval) along the y-axis. We consistently observed that the whole OS section, not only the OS tip or the 'IS/OS' junction, produced OCT signal; and the band of lower reflectivity (red arrow in Fig. 2c) was observed located sclerally to the 2<sup>nd</sup> OCT band. Moreover, bright spots (red arrows in Figs. 2a and 2b), with dimension at cellular level, were consistently observed. This might reflect reflectance inhomogeneity of different photoreceptors in the frog retina that has 2 types each of cones and rods.

Figure 3 shows comparative histological (Fig. 3a and 3b) and LS-OCT (Fig. 3c) images. For histological examination, DNA was stained with DAPI (blue) with Prolong Gold antifade mounting reagent (Invitrogen) in 10- $\mu\text{m}$  thick fixed retinal cryosections [9]. The DNA marked fluorescence image and the differential interference contrast (DIC) image were superimposed. Based on previously reported light [10] and electron [5] microscopy investigations of frog retinas, the IS/OS, OLM, OPL, etc. were identified in Fig. 3a. For the frog retina, the ONL could be identified as having two rows of nuclei [5, 10]. Frog IS ellipsoid, like humans, is full of mitochondria [3, 5] that contains DNA. Therefore, IS ellipsoid portion was also stained by DAPI, and thus could be separated from other IS portions.

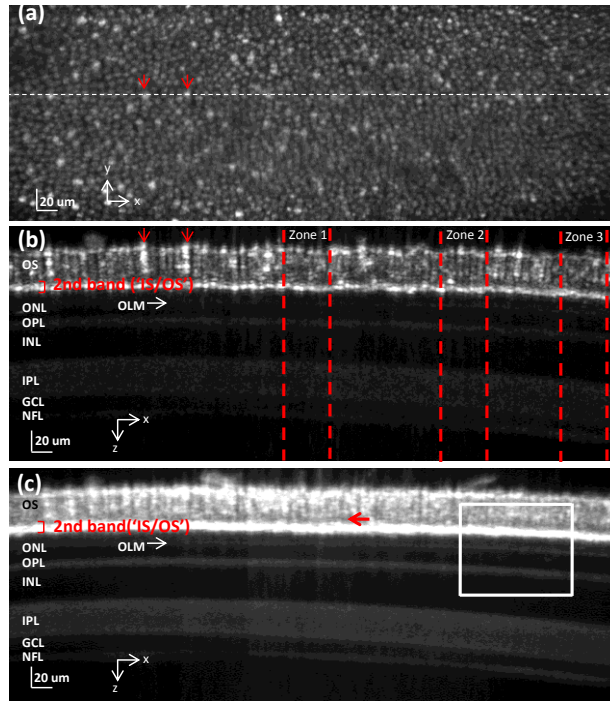


Fig.2. LS-OCT images. (a) En-face image of OS, acquired by averaging a stack of images of OS over 20  $\mu\text{m}$ . (b) Cross-section OCT image of the area marked by the white dashed line in a. Zones 1-3 marked by vertical lines were used for quantitative analysis in Fig. 3d. (c) Cross-section OCT image averaged over 120  $\mu\text{m}$  along the y-axis. The intensity was multiplied by 2, compared to the image in b. Red arrow points to a local hypo-reflective band. The white window shows the area for enlarged display in Fig. 3c.

Figs. 3b and 3c show enlarged sub-images of the histological (Fig. 3a) and OCT (Fig. 2c) images. If the 2<sup>nd</sup> OCT band is correctly attributed to the IS/OS, it would be expected to align with anatomic counterpart in the histological image (Fig. 3b). However, the center of the 2<sup>nd</sup> OCT band shifted toward to the IS, mostly like the IS ellipsoid portion. In contrast, the local hypo-reflective band (red arrow in Fig. 3c) might relate to the IS/OS junction [3].

In order to achieve quantitative analysis, the distance between the well-

established OLM and OPL bands were used to normalize the axial position of the 2<sup>nd</sup> OCT band. Fig. 3d shows 3 representative OCT longitudinal reflectance profiles (LRPs) as a function of retinal depth for three zones specified in Fig. 2b. Each zone was averaged over 50  $\mu\text{m}$  along the x-axis to improve signal to noise ratio. In theory, the OCT bands could be widened due to the logarithmic transformation or gamma correction of OCT displaying [3]. However, neither the logarithmic transformation nor gamma correction shifts the peaks. Therefore, the positions on the z-axis of peaks of the 'IS/OS' (2<sup>nd</sup>) band, the OLM (1<sup>st</sup>) band and the OPL band could be defined as their axial positions. Thus, OCT distance ratio  $(\text{OCT}_{\text{IS/OS}} - \text{OCT}_{\text{OLM}}) / (\text{OCT}_{\text{OLM}} - \text{OCT}_{\text{OPL}})$  could be quantitatively computed and compared to histological distance ratio of  $(\text{H}_{\text{IS/OS}} - \text{H}_{\text{OLM}}) / (\text{H}_{\text{OLM}} - \text{H}_{\text{OPL}})$ .

Fig. 3e shows statistics of OCT and histological distance ratios. Five retinas were used for OCT imaging, and corresponding five retinas were used for histology measurement. For each sample, six lateral positions were measured for estimating the distance ratio. As shown in Fig. 3e, the histological distance ratio of  $(\text{H}_{\text{IS/OS}} - \text{H}_{\text{OLM}}) / (\text{H}_{\text{OLM}} - \text{H}_{\text{OPL}})$  was  $1.0 \pm 0.05$ . In contrast, the mean of  $(\text{OCT}_{\text{IS/OS}} - \text{OCT}_{\text{OLM}}) / (\text{OCT}_{\text{OLM}} - \text{OCT}_{\text{OPL}})$  was  $0.6 \pm 0.1$ . The significant difference (t-test,  $p < 0.003$ ) between the  $(\text{OCT}_{\text{IS/OS}} - \text{OCT}_{\text{OLM}}) / (\text{OCT}_{\text{OLM}} - \text{OCT}_{\text{OPL}})$  and  $(\text{H}_{\text{IS/OS}} - \text{H}_{\text{OLM}}) / (\text{H}_{\text{OLM}} - \text{H}_{\text{OPL}})$  suggested that the 2<sup>nd</sup> OCT band might not actually relate to the IS/OS junction.

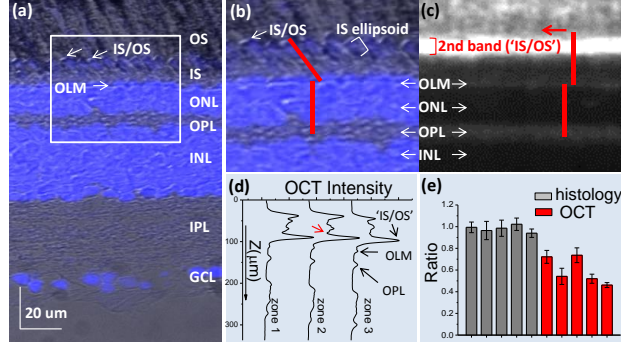


Fig. 3. Comparison between OCT and histological images. (a) Histological image. (b) Enlarged sub-image marked by the white window in Fig. 3a. (c) Enlarged image of OCT sub-image marked by the white window in Fig. 2c. Four red bars in Fig. 3b and Fig. 3c have identical length. (d) Curves of OCT intensity over retinal depth (z axis) of three zones in Fig. 2b. The red arrow points to the local hypo-reflective band, bordering posteriorly on the ‘IS/OS’ band (red arrows in Figs. 2c and 3c). (e) Histological distance ratio  $(H_{IS/OS}-H_{OLM})/(H_{OLM}-H_{OPL})$  and the OCT distance ratio  $(OCT_{IS/OS}-OCT_{OLM})/(OCT_{OLM}-OCT_{OPL})$ . Five samples were used for histological and OCT measurements, respectively. For each sample, six positions were measured. Error bars indicate standard deviations.

In summary, a LS-OCT was developed to demonstrate OCT imaging at sub-cellular resolution in both lateral (Fig. 2a) and axial (Fig. 2b) directions. Quantitative comparison of histological images and LS-OCT images revealed that the OCT distance ratio  $(OCT_{IS/OS}-OCT_{OLM})/(OCT_{OLM}-OCT_{OPL})$  was significantly smaller than the histological distance ratio  $(H_{IS/OS}-H_{OLM})/(H_{OLM}-H_{OPL})$ . The significant difference suggests that dominant source of the signal reported as the ‘IS/OS’ OCT band actually originates from the IS. We speculate that the IS ellipsoid, which consists of abundant mitochondria, or the CC extended into the IS [11] may contribute to the observed 2<sup>nd</sup>

OCT band signal.

Moreover, reflectance inhomogeneity was consistently observed at cellular level (Figs. 2a and 2b). The bumpy 2<sup>nd</sup> OCT band shown in Fig. 2b, might attribute to variable lengths and axial locations of different rod/cone photoreceptors [5]. Robust OCT signal was observed through the whole length of the photoreceptor outer segment. Early spectral-domain OCT study (SD-OCT) did not report OCT signal in the outer segment, i.e., the depth between the presumed 'IS/OS' band and the posterior tip of the OS [2]. We speculate that this discrepancy might attribute to large (0.3) numeric aperture (NA) of the LS-OCT system, compared to ~ 0.1 NA in typical SD-OCT system for retinal imaging. Increased NA could improve collection efficiency of reflected light, particularly scattering light with possible large angle changes, relative to incident light, from outer segment discs. In addition, the large NA system might produce illumination light with incident angle greater than the optimized acceptance of the photoreceptor, which acted as a waveguide [12]. Therefore, more light might be scattered and thus detected from the OS. We expect that further characterization of these observed OCT signals will provide insight for improved instrumental design, validated image attribution, and retinal diagnosis.

The authors thank Jerry Millican and Yangguo Li for mechanical fabrication and prototype construction of the LS-OCT. This research is supported partially by Dana Foundation (Brain and Immuno-Imaging Grant program); Eyesight Foundation of Alabama, NSF CBET-1055889, NIH R21 RR025788, NIH R21 EB012264, NIH R01 EY018143 and Vision Sciences Core grant NIH P30 EY03039.

## Reference

1. D. C. Hood, X. Zhang, R. Ramachandran, C. L. Talamini, A. Raza, J. P. Greenberg, J. Sherman, S. H. Tsang, and D. G. Birch, "The inner segment/outer segment border seen on optical coherence tomography is less intense in patients with diminished cone function," *Investigative ophthalmology & visual science* **52**, 9703-9709 (2011).
2. D. T. Miller, O. P. Kocaoglu, Q. Wang, and S. Lee, "Adaptive optics and the eye (super resolution OCT)," *Eye (Lond)* **25**, 321-330 (2011).
3. R. F. Spaide and C. A. Curcio, "Anatomical correlates to the bands seen in the outer retina by optical coherence tomography: literature review and model," *Retina* **31**, 1609-1619 (2011).
4. Y. Yamauchi, H. Yagi, Y. Usui, K. Kimura, T. Agawa, R. Tsukahara, N. Yamakawa, and H. Goto, "Biological activity is the likely origin of the intersection between the photoreceptor inner and outer segments of the rat retina as determined by optical coherence tomography," *Clin Ophthalmol* **5**, 1649-1653 (2011).
5. S. E. Nilsson, "An Electron Microscopic Classification of the Retinal Receptors of the Leopard Frog (*Rana Pipiens*)," *Journal of ultrastructure research* **10**, 390-416 (1964).
6. X. C. Yao, A. Yamauchi, B. Perry, and J. S. George, "Rapid optical coherence tomography and recording functional scattering changes from activated frog retina," *Applied optics* **44**, 2019-2023 (2005).
7. Y. G. Li, L. Liu, F. Amthor, and X. C. Yao, "High-speed line-scan confocal imaging of stimulus-evoked intrinsic optical signals in the retina," *Optics letters* **35**, 426-428 (2010).
8. J. M. Huntley, G. H. Kaufmann, and D. Kerr, "Phase-shifted dynamic speckle pattern interferometry at 1 kHz," *Applied optics* **38**, 6556-6563 (1999).
9. Y. Zhang, L. L. Molday, R. S. Molday, S. S. Sarfare, M. L. Woodruff, G. L. Fain, T. W. Kraft, and S. J. Pittler, "Knockout of GARPs and the beta-subunit of the rod cGMP-gated channel disrupts disk morphogenesis and rod outer segment structural integrity," *Journal of cell science* **122**, 1192-1200 (2009).
10. J. Mazelova, N. Ransom, L. Astuto-Gribble, M. C. Wilson, and D. Deretic, "Syntaxin 3 and SNAP-25 pairing, regulated by omega-3 docosahexaenoic acid, controls the delivery of rhodopsin for the biogenesis of cilia-derived sensory organelles, the rod outer segments," *Journal of cell science* **122**, 2003-2013 (2009).
11. Q. Liu, G. Tan, N. Levenkova, T. Li, E. N. Pugh, Jr., J. J. Rux, D. W. Speicher, and E. A. Pierce, "The proteome of the mouse photoreceptor sensory cilium complex," *Molecular & cellular proteomics : MCP* **6**, 1299-1317 (2007).

12. C. W. Stiles and B. L. Crawford, "The luminous efficiency of rays entering the eye pupil at different points," Proc R Soc Lond B. **112**, 428-450 (1933).



DYNAMIC NEAR-INFRARED IMAGING REVEALS TRANSIENT PHOTOTROPIC  
CHANGE IN RETINAL ROD PHOTORECEPTORS

by

RONGWEN LU, ALEXANDER M. LEVY, QIUXIANG ZHANG, STEVEN J  
PITTLER AND XINCHENG YAO

Journal of Biomedical Optics 18(10), 106013-106013, 2013

Copyright  
2013  
by  
SPIE

Used by permission

Format adapted and errata corrected for dissertation

## **Abstract**

Stiles-Crawford effect (SCE) is exclusively observed in cone photoreceptors, but why the SCE is absent in rod photoreceptors is still a mystery. In this study, we employed dynamic near infrared (NIR) light imaging to monitor photoreceptor kinetics in freshly isolated frog and mouse retinas stimulated by oblique visible light flashes. It was observed that retinal rods could rapidly (onset: ~10 ms for frog and 5 ms for mouse; time-to-peak: ~200 ms for frog and 30 ms for mouse) shift toward the direction of the visible light, which might quickly compensate for the loss of luminous efficiency due to oblique illumination. In contrast, such directional movement was negligible in retinal cones. Moreover, transient rod phototropism could contribute to characteristic intrinsic optical signal (IOS). We anticipate that further study of the transient rod phototropism may not only provide insight into better understanding of the nature of vision but also promise an IOS biomarker for functional mapping of rod physiology at high resolution.

**Keywords:** Stiles-Crawford effect; phototropism; photoreceptor; directional illumination

## **1 Introduction**

The Stiles-Crawford effect (SCE) states that luminance efficiency is dependent on incident light direction relative to the eye axis.(1) It is well established that the retina is more sensitive to light entering the center of the pupil, i.e., parallel light relative to eye axis, than light passing through the periphery, i.e., oblique light illumination. The SCE is exclusively observed in cones, which can benefit good vision quality by suppressing intraocular stray light under photopic conditions.(2) In contrast, the SCE has not been detected in rods which dominates scotopic vision.(2) In other words, the absorption

efficiency of light by rods is not affected by the incident angle in early SCE studies which were performed with psychophysical methods.(2) The biophysical mechanisms underlying this rod/cone difference are not established. In this study, we conducted dynamic near infrared (NIR) light imaging to explore transient changes in rod and cone photoreceptors activated by oblique light stimuli. High-spatial ( $\mu\text{m}$ ) and high-temporal (ms) resolution NIR imaging revealed that 80% of rods could rapidly move toward the direction of oblique stimulus light, while such directional movement was negligible in cones. Our experimental results suggest that transient phototropic adaptation may quickly compensate for the loss of luminous efficiency in rods activated by oblique stimulation, which can explain the absence of the SCE in the rod system. The observed transient phototropic adaptation of retinal rods not only provides insight into the nature of vision but also promises an intrinsic optical signal (IOS) biomarker. This would enable noninvasive, high-resolution assessment of rod function, which is known to be more vulnerable than cone function in aging and early age-related macular degeneration (AMD),(3, 4) the most common cause of severe vision loss and legal blindness in adults over 50.(3, 5)

## **2 Materials and Methods**

### *2.1 Retina preparation*

Animal handling was approved by the Institutional Animal Care and Use Committee of the University of Alabama at Birmingham. Both frog (*Rana pipiens*) and mouse (*Mus musculus*) retinas were used to demonstrate the transient phototropic adaptation in the retina.

Frog retinas were selected as primary specimens in this study for several reasons. First, the relatively large size of frog (compared to mouse or other mammalian) photoreceptors allows unambiguous observation of individual photoreceptors. Second, the diameter of frog rods (~5-8  $\mu\text{m}$ ) is much larger than cones (~1-3  $\mu\text{m}$ ),(6, 7) and thus rod and cone photoreceptors can be easily separated based on their cellular diameters. Third, rod and cone numbers are roughly equal in frog retinas,(6, 7) and thus unbiased analysis of rod and cone cells can be readily achieved. Preparation procedures of fresh living whole-mount frog retinas have been reported in previous publications.(8) Briefly, the frog was euthanized by rapid decapitation and double pithing. After enucleating the intact eye we hemisected the globe below the equator with fine scissors. The lens and anterior structures were removed before the retina was separated from the retinal pigment epithelium.

Mouse retinas were used to verify the transient phototropic adaptation in mammals. 5-month-old wild type mice, which have been maintained for more than 20 generations from an original cross of C57Bl/6J to 129/SvEv, were used in this study. The *rd1* allele that segregated in the 129/ SvEv stock was removed by genetic crossing and verified as previously described.(9) Protocols for handling mouse samples were previously reported.(10) Briefly, after the eyeball was enucleated from anesthetized mice, the retina was isolated from the eyeball in Ames media and then transferred to a recording chamber. During the experiment, the sample was continuously superfused with oxygenated bicarbonate-buffered Ames medium, maintained at pH 7.4 and 33~37 °C.

## 2.2 Experimental setup

The imaging system was based on a NIR digital microscope that has been previously used for functional imaging of living retinal tissues.<sup>(10)</sup> A fast digital camera (Neo sCMOS, Andor Technology) with pixel size  $6\ \mu\text{m} \times 6\ \mu\text{m}$  was used for retinal imaging. A 20x water immersion objective with 0.5 NA was used for frog experiments. Therefore, the lateral resolution of the system was about  $1\ \mu\text{m}$  ( $0.61\lambda/\text{NA}$ ). For mouse experiments, we used a 40x water immersion objective with 0.75 NA which has the lateral resolution of  $0.7\ \mu\text{m}$ . The system consisted of two light sources: a NIR (800-1000 nm) light for retinal imaging and a visible (450-650 nm) LED for retinal stimulation. The duration of the visible flash was 5 ms. Fig. 1 illustrates rectangular stimulus patterns with oblique incident angles [Fig. 1(a)], and a circular stimulus pattern with perpendicular incident angle [Fig. 1(b)]. Fig. 1(a) and Fig. 1(b) were used for the experiments in Figs. 2 and 4, and Fig. 3, respectively. All images of retinas in this article were acquired at 200 frames/s.

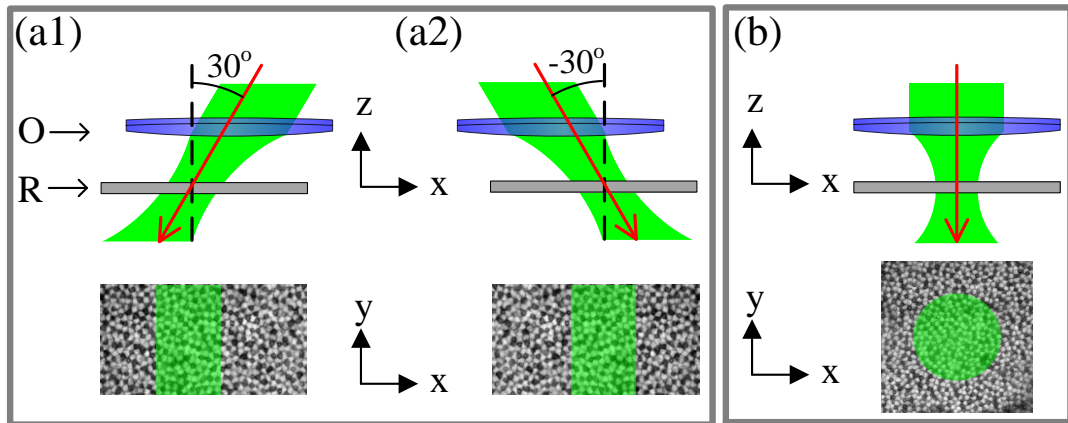


**Fig. 1.** Schematic diagram of stimulation patterns. O: objective; and R: retina. Black dash lines indicate the normal axis of retinal surface. Red solid lines indicate the incident directions. Top panels are cross-section view (transverse or x-z plane) and the bottom

panels are enface view (axial or x-y plane). (a1) Rectangular stimulus (bottom panel) with  $30^\circ$  incident angle with respect to the normal axis of retinal surface (top panel). (a2) Rectangular stimulus (bottom panel) with  $-30^\circ$  incident angle (top panel). (b) Circular stimulus (bottom panel) with  $0^\circ$  incident angle (top panel). The retina was placed with the ganglion cell layer (GCL) facing toward the objective.

### *2.3 Dynamic calculation of individual photoreceptor movements*

In order to quantify transient phototropic changes in rod and cone systems, we calculated the displacement of individual rods [Figs. 2(b) and 4(b) ] and cones [Fig. 2(b)]. The level-set method (11) was used to identify the morphological edge of individual rods and cones. Then the weight centroid was calculated dynamically, allowing accurate registration of the location of individual photoreceptors at nm resolution. The same strategy has been used in stochastic optical reconstruction microscopy (STORM) (12) and photoactivated localization microscopy (PALM) (13, 14) to achieve nm resolution to localize individual molecules with photo-switchable fluorescence probes. The three-sigma rule was used to set up a threshold to distinguish silent and active photoreceptors.(10) If the stimulus-evoked photoreceptor shifted above this threshold, then this photoreceptor was defined as active. Otherwise, it was defined as silent. Thus, the active ratio of the rods and cones could be obtained [Fig. 2(c)].

### *2.4 Computer algorithm of localized retinal movements*

The activated photoreceptors were displaced due to light stimulations [Figs. 2(d), 2(c) and 3(b)]. In order to quantify the photoreceptor displacements, the normalized cross

correlation (NCC) between the post-stimulus and pre-stimulus images were calculated to estimate localized retinal movements. We assume that  $I_{ii}(x, y)$  was the image acquired at the time point of  $t_i$ , where  $i = 1, 2, 3, \dots$  was the image index and  $(x, y)$  was the pixel position. We took the 1<sup>st</sup> image  $I_{t1}(x, y)$  as the reference image. For the pixel at the position of  $(x_0, y_0)$  from the image  $I_{ii}$ , there would be a horizontal shift  $H_{ii}(x_0, y_0)$  (parallel to the x axis) and a vertical shift  $V_{ii}(x_0, y_0)$  (parallel to the y axis) compared to the reference image. At the position of  $(x_0, y_0)$  from the image  $I_{ii}$ , we took a sub-window  $W_{ii}$  ( $m \times m$  pixels):

$$W_{ii}(x_0, y_0, u, v) = I_{ii}\left(x_0 - \frac{m-1}{2} + u, y_0 - \frac{m-1}{2} + v\right) \quad (1)$$

where  $u = 1, 2, 3, \dots, m$  and  $v = 1, 2, 3, \dots, m$ . Here we set  $m=13$  (corresponding to 3.9  $\mu\text{m}$  at the retina). This window is at the level of individual cells (cone: 5 ~ 8  $\mu\text{m}$ ; rod: 1 ~ 3  $\mu\text{m}$ ). We selected corresponding sub-window of the reference image at the position of  $(x_1, y_1)$ :

$$W_{t1}(x_1, y_1, u, v) = I_{t1}\left(x_1 - \frac{m-1}{2} + u, y_1 - \frac{m-1}{2} + v\right) \quad (2)$$

Then the correlation coefficient could be calculated between two image matrices defined by Eq. (1) and Eq. (2):

$$CC_{ii}(x_0, y_0, x_1, y_1) = \frac{\sum_{u=1}^m \sum_{v=1}^m [W_{ii}(x_0, y_0, u, v) - \overline{W_{ii}}][W_{t1}(x_1, y_1, u, v) - \overline{W_{t1}}]}{\left\{ \sum_{u=1}^m \sum_{v=1}^m [W_{ii}(x_0, y_0, u, v) - \overline{W_{ii}}] \right\}^{0.5} \left\{ \sum_{u=1}^m \sum_{v=1}^m [W_{t1}(x_1, y_1, u, v) - \overline{W_{t1}}] \right\}^{0.5}} \quad (3)$$

where  $\overline{W_{ii}}$  was the mean of the matrix  $W_{ii}(x_0, y_0, u, v)$ , and  $\overline{W_{t1}}$  was the mean of the matrix  $W_{t1}(x_1, y_1, u, v)$ . We searched  $x_1$  from  $x_0 - k$  to  $x_0 + k$ , and  $y_1$  from  $y_0 - k$  to  $y_0 + k$ , where  $k$  was the searching size, set to be 3 (corresponding to 0.9  $\mu\text{m}$  at the retina)

here. Thus we could find the position  $(x_{1\_max}, y_{1\_max})$ , where the value of correlation coefficient defined by Eq. (3) was maximum. Therefore, the horizontal shift (parallel to x axis) and vertical shift (parallel to y axis) at the position  $(x_o, y_o)$  were obtained as:

$$H_{ii}(x_o, y_o) = x_o - x_{1\_max} \quad (4-a)$$

$$V_{ii}(x_o, y_o) = y_o - y_{1\_max} \quad (4-b)$$

They could be rewritten as a complex number:

$$H_{ii} + jV_{ii} = A_{ii} \exp(j\Phi_{ii}) \quad (5)$$

where  $j$  is the imaginary unit,  $A_{ii}$  is the shift amplitude map [the color images in Figs. 2(d), 2(e) and 3(b)] and  $\Phi_{ii}$  is the direction map [directions of arrows in Figs. 2(d), 2(e) and 3(b)].

If

$$A_{ii}(x_o, y_o) \neq 0 \quad (6)$$

then the pixel  $(x_o, y_o)$  was displaced, thus defined as active. Therefore, the active pixel numbers could be plotted as a function of the time [Fig. 3(f)].

### 2.5 Intrinsic optical signal (IOS) data processing

In order to test the effect of the phototropic adaptation on the IOS pattern associated with circular stimulus, representative IOS images are illustrated in Fig 3(c), with a unit of  $\Delta I/I$ , where  $I$  is the background light intensity and  $\Delta I$  reflects the light intensity change corresponding to retinal stimulation. Basic procedures of IOS data processing have been previously reported.(8)



## Results

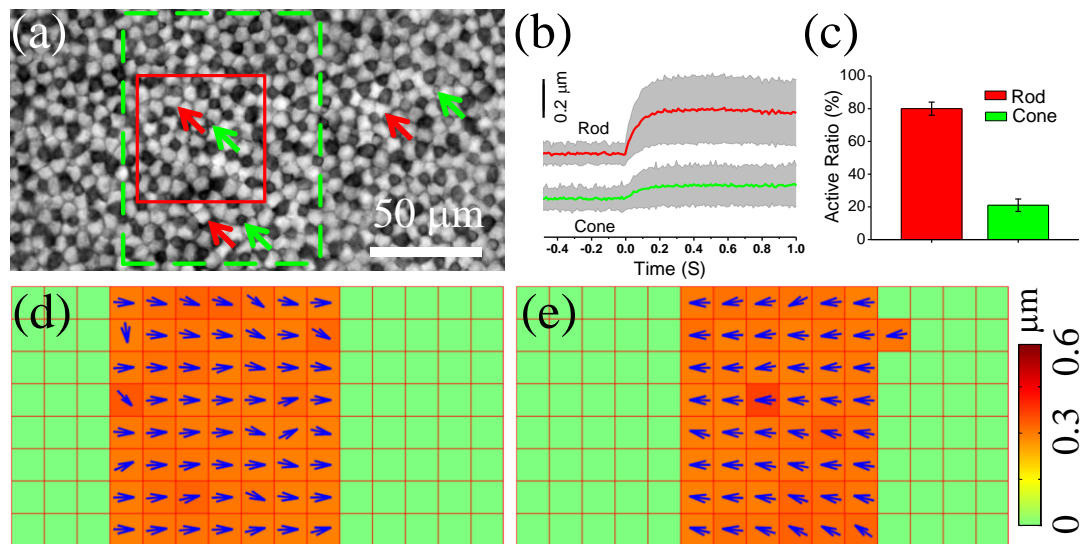
### *3.1 Transient phototropic adaptation in frog retina activated by oblique stimulation*

Fig. 2 shows results of phototropic adaptation correlated with oblique light stimulation. Fig. 2(a) shows the photoreceptor mosaic pattern. Individual rods [red arrows in Fig. 2(a)] and cones [green arrows in Fig. 2(a)] could be observed. A rectangular stimulus with  $30^\circ$  incident angle [Fig. 1(a1)] was delivered to the retina. Within the stimulation area, photoreceptor displacements were directly observed in NIR images (Video 1).

In order to quantify transient phototropic changes in rod and cone systems, we calculated displacements of individual rods and cones (see Materials and Methods). Fig. 2(b) shows average displacements of 25 rods and 25 cones randomly selected from the stimulus window. The displacement of rods occurred almost immediately ( $< 10$  ms) and reached magnitude peak at  $\sim 200$  ms. The magnitude of rod displacement (average:  $0.2 \mu\text{m}$ , with maximum up to  $0.6 \mu\text{m}$ ) was significantly larger than that of cone displacement (average:  $0.048 \mu\text{m}$ , with maximum of  $0.15 \mu\text{m}$ ). In addition, as shown in [Fig. 2(c)], the active ratio (see Materials and Methods for definition) of rods was  $80\% \pm 4\%$ , while  $20\% \pm 4\%$  of cones were activated. The observation indicated that the transient phototropic displacement was dominantly observed in rods.

In order to verify directional dependency of the phototropic adaptation, we used template matching with the NCC to compute non-uniform motion in the retina (see Materials and Methods). (15) As shown in Video 2 and Fig. 2(d), the stimulus-activated retina shifted to right, i.e., towards the direction of the  $30^\circ$  oblique stimulation. In order

to confirm the reliability of the phototropic response, the incident angle of the stimulus was switched to  $-30^\circ$  [Fig. 1(a2)], 5 minutes after the recording illustrated in Fig. 2(d). Fig. 2(e) illustrates the transient movement corresponding to  $-30^\circ$  stimulus at the same retinal area shown in Fig. 2(d). It was observed that the stimulated retina shifted toward left [Fig. 2(e)], i.e., in the opposite direction compared to Fig. 2(d). Comparative recording of the  $30^\circ$  and  $-30^\circ$  stimuli verified that transient photoreceptor movement was tightly dependent on the incident direction of the stimulus light.



**Fig. 2.** Oblique stimulus-evoked photoreceptor displacements. (a) NIR image of frog photoreceptor mosaic pattern. Green dashed window illustrates stimulus area. Red rectangle indicates the area shown in Video 1 (QuickTime, 7.7 MB) [URL:<http://dx.doi.org/10.1117/1.JBO.XX.X.XXXXXXX.1>] which displays a pair of pre- and post-stimulus images alternating repeatedly 20 times. Red and green arrows point to rods and cones, respectively. (b) Average displacement of 25 rods and cones which were randomly selected from the stimulus area. The gray shadow indicates the standard deviation. (c) Active ratios of rods and cones at time 200 ms after the onset of the

stimulus. Six trials were used. For each trial, 25 rods and cones were randomly selected. Thus, in each trial, the active ratio was calculated as the number of active rods or cones divided by 25. (d) Retinal displacements associated with the  $30^\circ$  stimulus [Fig. 3(a1)] at 200 ms. Dynamic changes of retinal displacement maps from  $-200$  ms to  $1,000$  ms are displayed in Video 2 (QuickTime, 6.7 MB) [URL:<http://dx.doi.org/10.1117/1.JBO.XX.X.XXXXXX.2>]. (e) Retinal displacements associated with the  $-30^\circ$  stimulus [Fig. 3(a2)] at 200 ms. Each square in (d) and (e) represents a  $15\ \mu\text{m} \times 15\ \mu\text{m}$  area of the retina. Transient displacements within the small square were averaged.

### *3.2 Transient phototropic adaptation in frog retina activated oblique stimulation by circular (transverse) stimulation with a Gaussian (axial) profile*

In addition to the aforementioned oblique stimulation, Fig. 3 shows transient photoreceptor displacements activated by a perpendicular circular stimulus with a Gaussian profile in the axial plane [Fig. 1(b)]. The circular aperture was conjugate to the focal plane of the imaging system. It is well known that cones taper toward the outer segment (OS) and are shorter than rods,<sup>(6)</sup> which implies that the OS pattern should have relatively larger extracellular space between photoreceptors when compared to the IS pattern. Therefore when the tight mosaic pattern of photoreceptors (Fig. 2a) was clearly observed, the focal plane was around the photoreceptor inner segment (IS). Hence, at the more distal position, i.e., the OS, the stimulus light was divergent and became oblique at the edge. However, at the central area, the stimulus light impinged the photoreceptor without directional dependence. Under this condition, only photoreceptors at the

periphery of the stimulus pattern underwent displacement, which can be directly visualized in Video 3. Figs. 3(b) and 3(d) not only confirmed this phenomenon but also revealed that peripheral photoreceptors shifted toward the center. The number of active pixels [see Eq. (6)] was plotted over time in Fig. 3(f). Rapid displacement occurred almost immediately ( $< 10$  ms) after the stimulus delivery, reached the magnitude peak at  $\sim 200$  ms and recovered at  $\sim 2$  seconds. It was consistently observed that the stimulus-evoked displacement was rod dominant. Utilizing the same methods employed in Fig. 2(c), rod and cone displacements were quantitatively calculated. Within the annular area in Fig. 3(d), 25 rods and cones were randomly selected for quantitative comparison.  $74\% \pm 6\%$  of rods were activated, while  $24\% \pm 5\%$  of cones were activated at 200 ms after the onset of stimulus (six samples).

### *3.3 Correlation of transient phototropism and IOS in frog retina*

We speculated that the transient phototropic changes may partially contribute to stimulus-evoked IOSs, which promised a noninvasive method for spatiotemporal mapping of retinal function. (8, 16) IOS images shown in Fig. 3(c) confirmed the effect of IOS enhancement at the edge of the circular stimulus. The edge enhanced IOS response gradually degraded over time, which was consistent with the change of the photoreceptor displacement [Fig. 3(b)]. In addition, both positive and negative IOS signals, with high magnitude, were observed at the periphery of the stimulus pattern. In contrast, the IOS signal at the stimulus center [Zone 2, Fig. 3(e)] was positive dominant, and the IOS magnitude was weaker than that observed at peripheral area [Zone 1, Fig. 3(e)]. Moreover, time courses of IOS responses were different between Zone 1 and Zone 2 [Fig.

3(g)]. The central IOS curve [black curve in Fig. 3(g)] more resembled the curve of active pixel number [Fig. 3(f)], which suggested that transient phototropic change primarily contribute to the periphery IOSs.

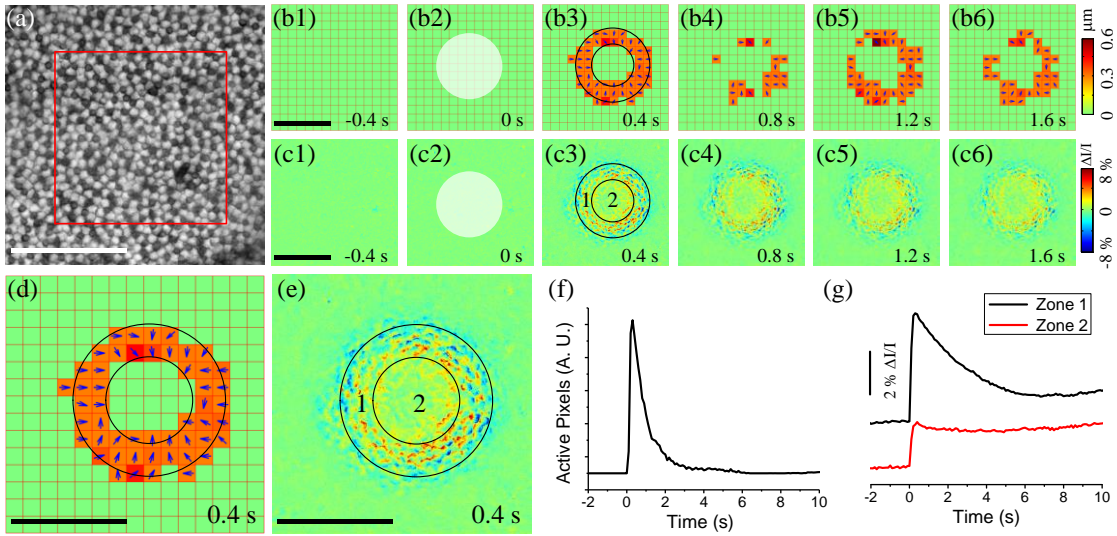


**Fig. 3.** Photoreceptor displacements and IOS responses stimulated by circular stimulus (in transverse plane) with a Gaussian profile (in axial plane). (a) NIR image of frog photoreceptor mosaic. Red rectangle indicated the area shown in Video 3 (QuickTime, 7.9 MB) [URL: <http://dx.doi.org/10.1117/1.JBO.XX.X.XXXXXX.3>] which displays a pair of pre- and post-stimulus images alternating repeatedly 20 times. (b) Localized retinal displacements associated with circular stimulus. This stimulus had a Gaussian profile in axial plane [Fig. 3(b)]. The same methods as those in Figs. 2(e) and 2(f) were used here to produce the displacement maps. (c) IOS maps.  $\Delta I$  reflected the light intensity change and  $I$  was the background light intensity. Zone 1 corresponds to the area within the inner ring. Zone 2 corresponds to the annular area. The stimulus was delivered at time 0. (d) Enlarged view of (b3). (e) Enlarged view of (c3). Scale bars indicate 100  $\mu\text{m}$ . (f)

Dynamic change of the number of active pixels in (b). The pixel with non-zero value was defined as active. (g) Temporal IOS profiles.

### 3.4 Transient phototropic adaptation in mouse retina activated by oblique stimulation

In order to verify the transient phototropic changes in mammals, we have conducted preliminary study of mouse retinas with oblique stimulation. Unlike large frog photoreceptors (rod:  $\sim 5\text{-}8\ \mu\text{m}$ , cone:  $\sim 1\text{-}3\ \mu\text{m}$ ), mouse photoreceptors ( $1\text{-}2\ \mu\text{m}$  for both rods and cones) are relatively small.(17, 18) Although individual mouse photoreceptors [Fig. 4(a)] were not as clear as frog photoreceptors [Fig. 3(a)], we selected representative individual mouse photoreceptors [arrows in Fig. 4(a)] which could be unambiguously isolated from others. Fig. 4(b) shows temporal displacements of 10 mouse photoreceptors pointed in Fig. 4a. These 10 photoreceptors shifted to left [arrows in Fig. 4(b)]. Fig. 4(c) shows average magnitude of photoreceptor displacements. As shown in Fig. 4(c), the displacement occurred within 5 ms, and reached the peak at 30 ms.

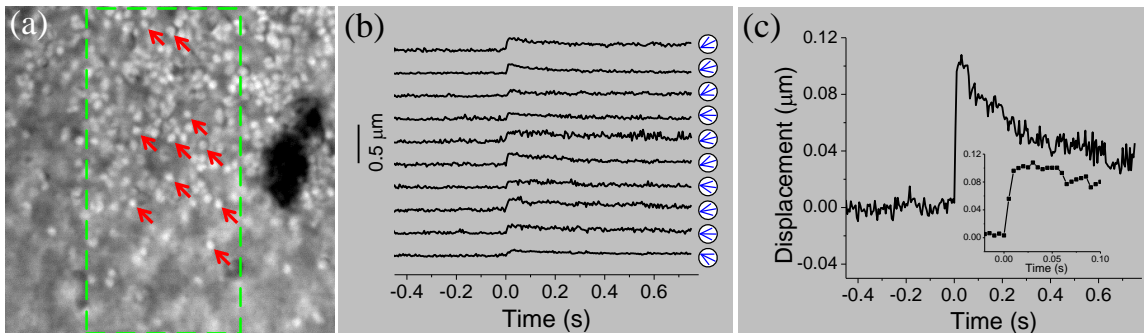


**Fig. 4.** Stimulus-evoked photoreceptor displacements at the mouse retina. (a) NIR image of mouse photoreceptor mosaic. A 40X objective with 0.75 NA was used. The image size corresponds to a  $60\ \mu\text{m} \times 60\ \mu\text{m}$  area at the retina. The green dashed rectangle indicates the oblique stimulation area. (b) Displacements of ten photoreceptors over time. The stimulus was delivered at time 0. These ten photoreceptors were specified by arrows in

(a). Green arrows in circles indicate the direction of the displacement at time 30 ms after stimulation. (c) Averaged displacement of 10 photoreceptors. The inset panel shows the same data within the time period from -0.02 s to 0.1 s.

## Discussion

In summary, high spatial and temporal resolution imaging revealed rod-dominant transient phototropic response in frog (Fig. 2) and mouse (Fig. 4) retinas under oblique stimuli. Such transient phototropic response could compensate for the loss of illumination efficiency under oblique stimulation in the rod system. Although the image resolution in Fig. 4(a) was not high enough to separate rods and cones reliably, we speculate that the observed displacement was rod dominated due to the established knowledge that rods account for ~97% of total number of the photoreceptors in mouse retinas.(19) In contrast to rods, it can take a long time, at least tens of seconds or even days, for cone adaptation. (20) In other words, rapid (onset: ~10 ms for frog and ~ 5 ms for mouse; time-to-peak: ~200 ms for frog and ~20 ms for mouse) phototropic adaptation in retinal rods is too quick for the SCE to be detected by conventional psychophysical methods with the advanced involvement of brain perception. Gaussian-shape stimulation further confirmed the transient rod displacement (Fig. 3). In addition, the observed off-center and on-surround pattern [Fig. 3(b)] may imply early involvement of the photoreceptors in contrast enhancement. The edge enhancement was confirmed by the IOS maps [Fig. 3(c)]. In general, it is believed that the center-surround antagonism, which is valuable for contrast perception, is initiated by horizontal cells (21, 22) and/or amacrine cells.(23) However, our experimental results here suggest that the discrepancy of the incident angle

between the surround and the center of the Gaussian illumination [Fig. 1(b)] can evoke directional displacement only at the surround [Fig. 3(b)]. Such an edge-enhanced pattern of photoreceptor activity may suggest early involvement of the photoreceptors in contrast perception.

Moreover, the observed transient rod movement provides an IOS biomarker to allow early detection of eye diseases that can cause retinal dysfunction. Rod function has been well established to be more vulnerable than cones in aging and early AMD,(3, 4) which is the most common cause of severe vision loss and legal blindness in adults over 50.(3, 5) Structural biomarkers, such as drusen and pigmentary abnormalities in the macula are important for retinal evaluation. Adaptive optics imaging of individual rods has been recently demonstrated.(24-26) However, the most commonly used tool for retinal imaging, the fundus examination, is not sufficient for a final retinal diagnosis.(27) In principle, physiological function is degraded in diseased cells before detectable abnormality of retinal morphology. Psychophysical methods (28-30) and electroretinography (ERG) (31) measurements have been explored for functional assessment of the retina, but reliable identification of localized rod dysfunctions is still challenging due to limited resolution and sensitivity. The experimental results shown in Fig. 3 indicate that the transient phototropic changes can partially contribute to IOS recording which has the potential to be developed into a superior noninvasive method for spatiotemporal mapping of retinal function.(8, 10) The different time courses of the IOSs at Zone 1 (periphery) and Zone 2 (center) suggest that the phototropic change of rod photoreceptors primarily contribute to the periphery IOS response. Multiple IOS origins, including neurotransmitter secretion,(32) refractive index change of neural tissues,(33)



interactions between photoexcited rhodopsin and GTP-binding protein,(34) disc shape change,(35) cell swelling,(36) etc. have been proposed. In order to investigate the biophysical mechanism of transient phototropic adaptation, we are currently pursuing optical coherence tomography (OCT) of retinal photoreceptors to quantify the axial location of phototropic kinetics. Further investigations are also planned to quantify time courses of the transient phototropic adaptations in wild type and diseased mouse retinas. We anticipate that further investigation of the rod dominant phototropic effect can provide a high resolution methodology to achieve objective identification of rod dysfunction, and thereby allowing early detection and easy treatment evaluation of eye diseases, such as AMD associated photoreceptor degeneration.

### **Acknowledgement**

This research is supported in part by NSF CBET-1055889, NIH R21 EB012264, UASOM I3 Pilot Award and NEI R01 EY018143-05. The authors wish to thank Dr. Christine Curcio and Dr. Walter Makous for their valuable comments and constructive suggestions on the manuscript, we thank Delores W. Davis in Dr. Pittler's laboratory for providing the mice and relevant genotype and age information.

### **Reference**

1. W. S. Stiles and B. H. Crawford, "The luminous efficiency of rays entering the eye pupil at different points," *Proc. R. Soc. Lond.* **112**(778), 428-450 (1933)
2. G. Westheimer, "Directional sensitivity of the retina: 75 years of Stiles-Crawford effect," *Proc. Biol. Sci.* **275**(1653), 2777-2786 (2008)
3. C. A. Curcio, N. E. Medeiros and C. L. Millican, "Photoreceptor loss in age-related macular degeneration," *Invest. Ophthalmol. Vis. Sci.* **37**(7), 1236-1249 (1996)

4. C. Owsley, et al., "Cone- and rod-mediated dark adaptation impairment in age-related maculopathy," *Ophthalmology* **114**(9), 1728-1735 (2007)
5. N. M. Bressler, S. B. Bressler and S. L. Fine, "Age-related macular degeneration," *Surv. Ophthalmol.* **32**(6), 375-413 (1988)
6. S. E. Nilsson, "An Electron Microscopic Classification of the Retinal Receptors of the Leopard Frog (*Rana Pipiens*)," *J. Ultrastruct. Res.* **10**(5), 390-416 (1964)
7. P. A. Liebman and G. Entine, "Visual pigments of frog and tadpole (*Rana pipiens*)," *Vis. Res.* **8**(7), 761-775 (1968)
8. X. C. Yao and Y. B. Zhao, "Optical dissection of stimulus-evoked retinal activation," *Opt. Express* **16**(17), 12446-12459 (2008)
9. S. J. Pittler and W. Baehr, "Identification of a nonsense mutation in the rod photoreceptor cGMP phosphodiesterase beta-subunit gene of the rd mouse," *Proc. Natl. Acad. Sci. U. S. A.* **88**(19), 8322-8326 (1991)
10. Q. X. Zhang, et al., "Comparative intrinsic optical signal imaging of wild-type and mutant mouse retinas," *Opt. Express* **20**(7), 7646-7654 (2012)
11. C. Li, et al., "Distance regularized level set evolution and its application to image segmentation," *IEEE Trans Image Process* **19**(12), 3243-3254 (2010)
12. M. J. Rust, M. Bates and X. Zhuang, "Sub-diffraction-limit imaging by stochastic optical reconstruction microscopy (STORM)," *Nat. Methods* **3**(10), 793-795 (2006)
13. E. Betzig, et al., "Imaging intracellular fluorescent proteins at nanometer resolution," *Science* **313**(5793), 1642-1645 (2006)
14. M. F. Juetten, et al., "Three-dimensional sub-100 nm resolution fluorescence microscopy of thick samples," *Nat. Methods* **5**(6), 527-529 (2008)
15. A. J. Hii, et al., "Fast normalized cross correlation for motion tracking using basis functions," *Comput. Methods Programs Biomed.* **82**(2), 144-156 (2006)
16. Q. X. Zhang, et al., "In vivo confocal intrinsic optical signal identification of localized retinal dysfunction," *Invest. Ophthalmol. Vis. Sci.* **53**(13), 8139-8145 (2012)
17. L. D. Carter-Dawson and M. M. LaVail, "Rods and cones in the mouse retina. I. Structural analysis using light and electron microscopy," *J. Comp. Neurol.* **188**(2), 245-262 (1979)
18. D. Mustafi, A. H. Engel and K. Palczewski, "Structure of cone photoreceptors," *Prog Retin. Eye Res.* **28**(4), 289-302 (2009)

19. C. J. Jeon, E. Strettoi and R. H. Masland, "The major cell populations of the mouse retina," *J. Neurosci.* **18**(21), 8936-8946 (1998)
20. H. S. Smallman, D. I. A. MacLeod and P. Doyle, "Vision: Realignment of cones after cataract removal," *Nature* **412**(6847), 604-605 (2001)
21. F. S. Werblin and J. E. Dowling, "Organization of the retina of the mudpuppy, *Necturus maculosus*. II. Intracellular recording," *J. Neurophysiol.* **32**(3), 339-355 (1969)
22. D. A. Baylor, M. G. Fuortes and P. M. O'Bryan, "Receptive fields of cones in the retina of the turtle," *J. Physiol.* **214**(2), 265-294 (1971)
23. D. S. Lebedev and D. W. Marshak, "Amacrine cell contributions to red-green color opponency in central primate retina: a model study," *Vis. Neurosci.* **24**(4), 535-547 (2007)
24. E. A. Rossi, et al., "Imaging retinal mosaics in the living eye," *Eye* **25**(3), 301-308 (2011)
25. D. Merino, et al., "Observation of cone and rod photoreceptors in normal subjects and patients using a new generation adaptive optics scanning laser ophthalmoscope," *Biomed. Opt. Express* **2**(8), 2189-2201 (2011)
26. N. Doble, et al., "In vivo imaging of the human rod photoreceptor mosaic," *Opt. Lett.* **36**(1), 31-33 (2011)
27. C. Owsley, et al., "Delays in rod-mediated dark adaptation in early age-related maculopathy," *Ophthalmology* **108**(7), 1196-1202 (2001)
28. R. Klein, et al., "The relationship of age-related maculopathy, cataract, and glaucoma to visual acuity," *Invest. Ophthalmol. Vis. Sci.* **36**(1), 182-191 (1995)
29. J. Siderov and A. L. Tiu, "Variability of measurements of visual acuity in a large eye clinic," *Acta Ophthalmol Scand* **77**(6), 673-676 (1999)
30. A. Loewenstein, et al., "Replacing the Amsler grid: a new method for monitoring patients with age-related macular degeneration," *Ophthalmology* **110**(5), 966-970 (2003)
31. A. Binns and T. H. Margrain, "Development of a technique for recording the focal rod ERG," *Ophthalmic Physiol. Opt.* **26**(1), 71-79 (2006)
32. B. M. Salzberg, A. L. Obaid and H. Gainer, "Large and rapid changes in light scattering accompany secretion by nerve terminals in the mammalian neurohypophysis," *J. Gen. Physiol.* **86**(3), 395-411 (1985)

33. R. A. Stepnoski, et al., "Noninvasive detection of changes in membrane potential in cultured neurons by light scattering," *Proc. Natl. Acad. Sci. U. S. A.* **88**(21), 9382-9386 (1991)
34. H. Kuhn, et al., "Interactions between photoexcited rhodopsin and GTP-binding protein: kinetic and stoichiometric analyses from light-scattering changes," *Proc. Natl. Acad. Sci. U. S. A.* **78**(11), 6873-6877 (1981)
35. K. P. Hofmann, et al., "Measurements on fast light-induced light-scattering and -absorption changes in outer segments of vertebrate light sensitive rod cells," *Biophys. Struct. Mech.* **2**(1), 61-77 (1976)
36. I. Tasaki and P. M. Byrne, "Rapid structural changes in nerve fibers evoked by electric current pulses," *Biochem. Biophys. Res. Commun.* **188**(2), 559-564 (1992)

SUPER-RESOLUTION SCANNING LASER MICROSCOPY THROUGH  
VIRTUALLY STRUCTURED DETECTION

by

RONGWEN LU, BENQUAN WANG, QIUXIANG ZHANG AND XINCHENG YAO

Biomedical Optics Express 4(9), 1673-1682, 2013

Copyright

2013

by

Optical Society of America

Used by permission

Format adapted and errata corrected for dissertation

## **Abstract**

High resolution microscopy is essential for advanced study of biological structures and accurate diagnosis of medical diseases. The spatial resolution of conventional microscopes is light diffraction limited. Structured illumination has been extensively explored to break the diffraction limit in wide field light microscopy. However, deployable application of the structured illumination in scanning laser microscopy is challenging due to the complexity of the illumination system and possible phase errors in sequential illumination patterns required for super-resolution reconstruction. We report here a super-resolution scanning laser imaging system which employs virtually structured detection (VSD) to break the diffraction limit. Without the complexity of structured illumination, VSD provides an easy, low-cost and phase-artifact free strategy to achieve super-resolution in scanning laser microscopy.

© 2013 Optical Society of America

**OCIS codes:** (100.6640) Superresolution; (110.3080) Infrared imaging; (170.3880) Medical and biological imaging; (180.5810) Scanning Microscopy.

## **1. Introduction**

High resolution imaging is essential for biomedical study and disease evaluation. However, the spatial resolution of conventional imaging systems is constrained by light diffraction, which precludes the observation of fine structures of biological specimens. Several approaches, including stimulated emission depletion (STED) microscopy, stochastic optical reconstruction microscopy (STORM) and photoactivated localization microscopy (PALM), have been investigated to achieve super-resolution imaging. In a

STED system, the fluorophores are excited by an excitation laser and followed by a second depletion laser with a doughnut-shaped intensity profile. The STED laser can deactivate the fluorophores in the periphery of the excitation laser focus, allowing only the fluorescence from the sub-diffraction-limited center to contribute to super-resolution recording [1, 2]. However, the extremely intensive laser exposure limits its applications for live cell imaging of biological systems, such as delicate and fragile retina. Alternatively, STORM [3], PALM [4], or fluorescence PALM (FPALM) [5] can achieve super-resolution by mapping localizations of individual molecules with photo-switchable fluorescence probes. Although single molecule localization based imaging approach has been demonstrated for live cell imaging [6-8], the imaging speed is limited due to the requirement of acquiring multiple sub-images for super-resolution reconstruction. Therefore, its application for high temporal resolution monitoring of live systems is still challenging.

Moreover, aforementioned super-resolution imaging approaches require exogenous fluorescent dyes or proteins. Therefore, they are not practical for intrinsic signal (e.g., reflectance or transmission) imaging. Bertero and his colleagues proposed a computational strategy suitable for both fluorescence and intrinsic signal imaging by taking the super-resolution reconstruction as an inverse problem [9-11]. However, the inversion process is ill-posed and sensitive to potential noise, and the reconstruction is numerically complicated and time consuming. Alternatively, structured illumination microscopy (SIM) has been developed to surpass the diffraction limit by shifting high frequency signal of the sample into the passing band of imaging systems [12-14]. The SIM can be implemented in both fluorescence and intrinsic signal imaging, However, the

wide-field spatially structured illumination patterns require sophisticated manipulation of the pattern generator, i.e., grating [12-14] or grid [15, 16], and is not suitable for extended application in confocal scanning laser microscopy (SLM). In theory, SIM can also be realized in a point scanning system through spatiotemporal modulation, either by modulating light source intensity in illumination arm or by placing a moving mask in light detection arm [17]. However, the spatiotemporal modulation of the illumination/detection arm is technically difficult. So far, experimental validation of the proposed spatiotemporal modulation is not yet demonstrated.

The purpose of this study is to demonstrate virtually structured detection (VSD) for super-resolution SLM, which requires neither dynamic modulation of the light source intensity in illumination arm nor the physical mask in light detection arm [17]. In the VSD-based system, the spatiotemporal modulation is achieved by mathematical processing of digital images. Digital implementation of the spatiotemporal modulation in the detection arm has been proposed in a theoretical article [17]. In this paper, freshly isolated retinas were employed for experimental validation of the VSD-based super-resolution system in intrinsic reflectance imaging of thick ( $> 100 \mu\text{m}$ ) live tissues. Experimental results showed that individual photoreceptors, which were not differentiated in the diffraction limited SLM, could be clearly identified in the VSD-based super-resolution imaging.

## **2. Method**

### *2.1. Experimental setup*

Figure 1 illustrates a schematic diagram of the VSD-based super-resolution SLM.



A superluminescent laser diode (SLD-35-HP, Superlum), with center wavelength  $\lambda=830$  nm and bandwidth  $\Delta\lambda=60$  nm, is used to produce near infrared (NIR) illumination of the specimen. A pair of galvo mirrors (GVS002, THORLABS) is used to steer the focused NIR light across the specimen to generate two-dimensional (2D) images. In order to control the vignetting effect, the Fourier plane of the objective is conjugated to the middle point between these two galvo mirrors. The reflected light from the sample is descanned by the 2D (X and Y) scanning system, and is relayed to the image plane (CCD). Instead of using a single element detector for recording light intensity in conventional SLM, a CCD camera (AVT Pike F-032B) is employed to map light profile (i.e., intensity distribution) of individual sampling points. The stack of 2D light profiles is used to construct super-resolution image based on the VSD method. Using a 5X objective with numeric aperture (NA) 0.1, the diffraction limited imaging resolution is  $5 \mu\text{m}$ ; while theoretical resolution of the VSD-based super-resolution imaging is  $2.5 \mu\text{m}$ .

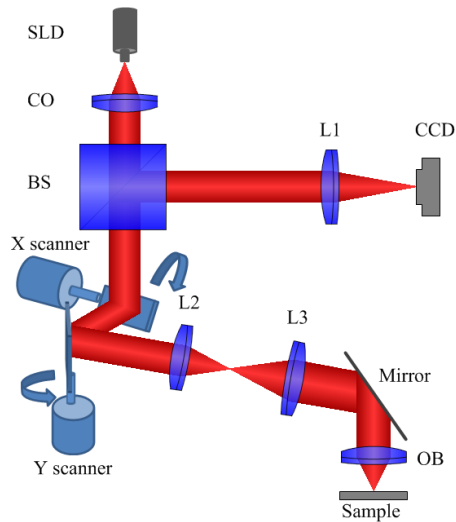


Fig. 1. Schematic diagram of experimental setup. OB: objective; CO: collimator; L1-L3: lens; and BS: beam splitter. Focal lengths of lenses L1, L2 and L3 are 200 mm, 40 mm and 150 mm, respectively. The objective is 5X (NA=0.1). The light source is provided by

the SLD with center wavelength  $\lambda=830$  nm and bandwidth  $\Delta\lambda=60$  nm. The theoretical resolution of this system is  $0.61\lambda/NA=5$   $\mu\text{m}$ .

Confocal configuration can be readily achieved using virtually synthesized pinholes [18] to reject out-of-focus light. The pinhole in conventional SLM and scanning laser ophthalmoscope (SLO) varies from 0.8X~10X Airy disc diameter [19-22] depending on specific applications. In comparison with a large pinhole, a small pinhole provides better resolution and enhanced sectioning ability [23]. However, a small pinhole can also reject photons that carry useful information which is required for the VSD-based super-resolution reconstruction. In this paper, we set the virtual confocal pinhole as 2X Airy disc diameter as a trade-off.

## 2.2. Principle of VSD-based super-resolution reconstruction

Point spread function (PSF) can be used to evaluate the resolution in spatial domain. For the system shown in Fig.1, the PSF of the illumination path  $h_{il}(x, y)$  is identical to the PSF of the detection path  $h_{de}(x, y)$ . Under incoherent illumination, the theoretical PSF is [24]:

$$h_{il}(x, y) = h_{de}(x, y) = \frac{\Omega^2}{\pi} \left( \frac{J_1(\Omega\rho)}{\Omega\rho} \right)^2 \quad (1)$$

where  $J_1$  is the first-order Bessel function,  $\Omega=2\pi NA/\lambda$  and  $\rho = \sqrt{x^2 + y^2}$ . The resolution of conventional SLM is defined as the radius of the Airy disc:

$$R = 0.61\lambda / NA \quad (2)$$

Given that  $\lambda=830$  nm and  $NA=0.1$ , the spatial resolution of the system is  $R=5$   $\mu\text{m}$ . In Fourier domain, the corresponding cutoff frequency of the PSF can be expressed as:

$$f_c = 1/R \quad (3)$$

In other words, only frequency below the cutoff frequency is able to pass through conventional SLM system:

$$-f_c \leq f \leq f_c \quad (4)$$

For a single point light source, we assume here that the illumination intensity has a normalized number 1. Therefore, at the sampling position  $(x_0, y_0)$ , corresponding light intensity distribution on the sample is  $h_{it}(x-x_0, y-y_0)$ . In a descanned system in Fig. 1, the light intensity distribution on the image plane (i.e., CCD) can be expressed as  $I_{des}(x, y, x_0, y_0)$ . The non-descanned image can be obtained by shifting descanned images:

$$I_{non}(x, y, x_0, y_0) = I_{des}(x-x_0, y-y_0, x_0, y_0) \quad (5)$$

If we assume the reflectance ratio of the sample is  $s(x, y)$  and that the magnification of the system is ignored, then we will have [17]

$$I_{non}(x, y, x_0, y_0) = \iint h_{it}(\mu-x_0, \nu-y_0) s(\mu, \nu) h_{de}(x-\mu, y-\nu) d\mu d\nu \quad (6)$$

In order to achieve VSD, a digital mask is applied to multiply with the non-descanned image:

$$I_{mul}(x, y, x_0, y_0) = I_{non}(x, y, x_0, y_0) m(x, y) \quad (7)$$

We select a digital mask  $m(x, y)$  with sinusoidal function:

$$m(x, y) = \cos[2\pi f_0 (x \cos \theta + y \sin \theta) + \alpha] \quad (8)$$

where  $\theta$  is the rotation angle of sinusoidal stripes and  $\alpha$  represents a constant phase. The carrier frequency  $f_0$  is set here to the value of the cutoff frequency  $f_c$ :

$$f_0 = f_c \quad (9)$$

It is worth noting that negative values are allowed in the digital mask. Therefore, there is no direct current (DC) component in Eq. (8). The spatial integral of the image  $I_{mul}(x, y, x_0, y_0)$  is assigned to the position  $(x_0, y_0)$ :

$$p(x_0, y_0) = \iint I_{mul}(x, y, x_0, y_0) dx dy \quad (10)$$

Substituting Eqs. (6) and (7) into Eq. (10) yields [17]:

$$\begin{aligned} p(x_0, y_0) &= \iiint h_{il}(\mu - x_0, \nu - y_0) s(\mu, \nu) h_{de}(x - \mu, y - \nu) m(x, y) d\mu d\nu dx dy \\ &= \iint h_{il}(\mu - x_0, \nu - y_0) s(\mu, \nu) \left[ \iint h_{de}(\mu - x, \nu - y) m(x, y) dx dy \right] d\mu d\nu \\ &= h_{il}(x_0, y_0) \otimes \left\{ s(x_0, y_0) \left[ h_{de}(x_0, y_0) \otimes m(x_0, y_0) \right] \right\} \end{aligned} \quad (11)$$

where the integration order is changed, the fact that PSFs are even functions is assumed, and  $\otimes$  denotes convolution. Considering  $h_{il}(x, y) = h_{de}(x, y)$ , exchanging  $h_{de}(x, y)$  and  $h_{il}(x, y)$  and then rearranging Eq. (11) yield:

$$p(x_0, y_0) = \left\{ \left[ m(x_0, y_0) \otimes h_{il}(x_0, y_0) \right] s(x_0, y_0) \right\} \otimes h_{de}(x_0, y_0) \quad (12)$$

Eq. (12) exactly represents the acquired image of conventional wide-field SIM in which the modulation function  $m(x_0, y_0)$  is implemented spatially in the illumination arm [25]. Equivalency of Eq. (11) and Eq. (12) implies that modulations in the illumination arm and in the detection arm are equivalent to each other in theory. The Fourier transform of Eq. (11) is [17]:

$$\tilde{p}(f_x, f_y) = ft[p(x_0, y_0)] = \tilde{h}_{il}(f_x, f_y) \left\{ \tilde{s}(f_x, f_y) \otimes \left[ \tilde{h}_{de}(f_x, f_y) \tilde{m}(f_x, f_y) \right] \right\} \quad (13)$$

where  $f_x$  and  $f_y$  are spatial frequencies, and  $ft$  is the Fourier transform operator.  $\tilde{m}(f_x, f_y)$  is the Fourier transform of Eq. (8):

$$\tilde{m}(f_x, f_y) = \frac{1}{2} \left[ \sigma(f_x - f_0 \cos\theta, f_y - f_0 \sin\theta) e^{i\alpha} + \sigma(f_x + f_0 \cos\theta, f_y + f_0 \sin\theta) e^{-i\alpha} \right] \quad (14)$$

where  $\sigma$  is the Dirac delta function. Because of sifting property of the Dirac delta function, Eq. (13) can be rewritten as:

$$\tilde{p}(f_x, f_y) = \tilde{h}_H(f_x, f_y) \left[ \tilde{s}(f_x - f_0 \cos\theta, f_y - f_0 \sin\theta) e^{i\alpha} + \tilde{s}(f_x + f_0 \cos\theta, f_y + f_0 \sin\theta) e^{-i\alpha} \right] \quad (15)$$

where constant coefficients are ignored. Thus, the higher frequency  $\tilde{s}(f_x, f_y)$  is shifted toward the lower passing band of  $\tilde{h}_H(f_x, f_y)$  and the retrievable frequency based on Eq. (15) is

$$-2f_c \leq f \leq 2f_c \quad (16)$$

Therefore, the theoretical retrievable band width is doubled. In other words, the theoretical resolution is enhanced by a factor of two.

### 2.3. Sample Preparation

A standard optical target (USAF 1951 1X, Edmond) and freshly isolated frog (*Rana Pipiens*) retina was used for functional test of the system in Fig.1. It is known that the frog retina consists of photoreceptors with variable diameters (rods: ~5-8  $\mu\text{m}$ ; cones: ~1-3  $\mu\text{m}$ ) [26, 27]. Therefore, the frog retina provides an excellent preparation to evaluate the SLM resolution before (5  $\mu\text{m}$ ) and after (2.5  $\mu\text{m}$ ) VSD data processing. Moreover, the frog retina has ~ 200  $\mu\text{m}$  thickness, and thus it readily allows testing the VSD-based super-resolution imaging in deep (> 100  $\mu\text{m}$ ) tissue. Animal handling was approved by the Institutional Animal Care and Use Committee of the University of Alabama at Birmingham. Preparation procedures of freshly isolated retinas have been documented in previous publications [28, 29]. Briefly, the frog was euthanized by rapid decapitation and double pithing. After enucleating the intact eye we hemisected the globe below the

equator with fine scissors. The lens and anterior structures were removed before the retina was separated from the retinal pigment epithelium.

### 3. Results

#### 3.1. Computer simulation of VSD-based super-resolution imaging

Fig. 2 shows computational simulation of the VSD-based super-resolution method. The diffraction limited resolution of the simulated system was  $5\ \mu\text{m}$  while the period of the simulated sample was  $2.5\ \mu\text{m}$ . In other words, the information of the sample (black curve in Fig. 2B) could not pass through the passing band of the PSF (red curve in Fig. 2B) except for the DC component. Therefore, conventional SLM could not differentiate the sinusoidal variations of the sample as shown in Fig. 2C. Fig. 2D confirmed that only DC component of the sample was detected by conventional SLM. In contrast, the VSD-based super-resolution imaging detected the diffraction light profile of each sampling point (Fig. 2E). The diffraction light profile was modulated by digital sinusoidal masks, as shown in Figs 2F-2H. Then the spatial integration was applied to the modulated map [see Eq. (10)]. Fig. 2I shows the reconstructed image through the VSD-based super-resolution method. From Fig. 2I and its spectrum (Fig. 2J), we can see that the lost information outside of the critical frequency was partially retrieved.

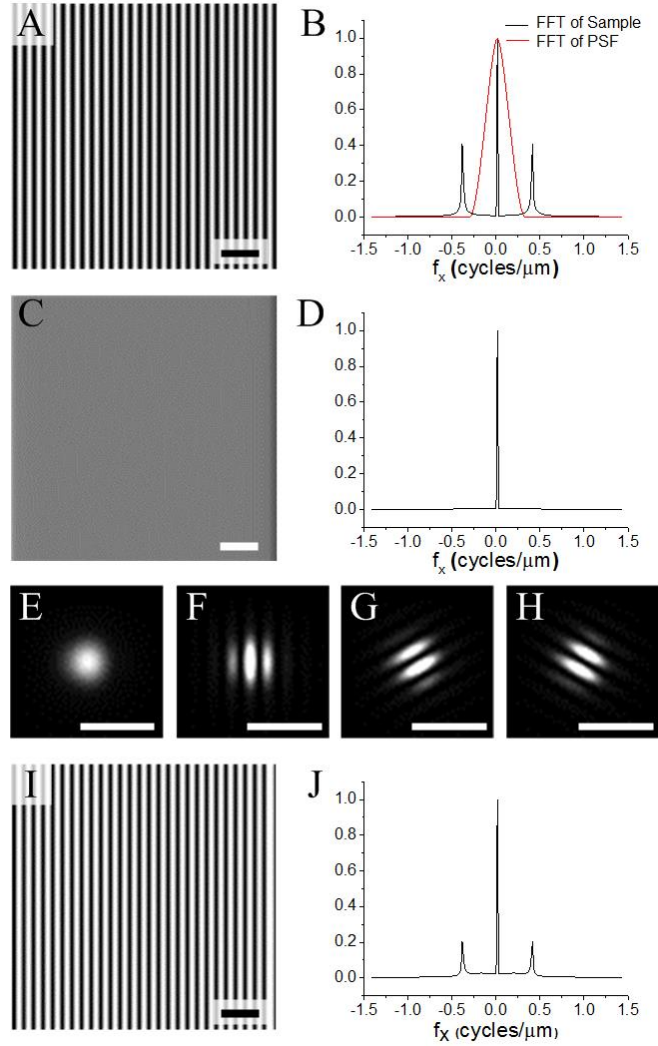


Fig.2. Computational simulation of the VSD-based super-resolution imaging.  $\lambda=830$  nm,  $NA=0.1$  and incoherent illumination was assumed. The resolution of this system was  $0.61\lambda/NA = 5 \mu\text{m}$ . (A) Sample of sinusoidal stripes. The period was  $2.5 \mu\text{m}$ . (B) Normalized spectra of the sample and the PSF of the system on x dimension. The PSF was defined by Eq. (1). (C) Conventional SLM image. (D) Normalized spectrum of the image (C) on x dimension. (E) Diffraction map of the sampling point at the center of the image (A). (F)-(H) superimposed images [see Eq. (7)] between the diffraction map (E) and the sinusoidal maps with orientation angle  $\theta=0, 60^\circ$  and  $120^\circ$ , respectively. (I)

Reconstructed super-resolution image. The background of the image was removed. (J)  
Normalized spectrum of the image (I) on x dimension. Scale bars indicate 10  $\mu\text{m}$ .

### *3.2. VSD-based super-resolution imaging of standard optical target*

First of all, we used standard optical target (USAF 1951 1X, Edmond) to verify the VSD-based super-resolution imaging. Fig. 3A was the image acquired by conventional SLM. The period of the smallest grating (white and blue rectangles in Fig. 3A) of this test target is 4.4  $\mu\text{m}$ . The theoretical resolution of conventional SLM, which employed a 5X objective with 0.1 NA, was 5  $\mu\text{m}$ . Therefore, conventional SLM was not able to resolve the smallest gratings, as shown both in the white and blue rectangles in Fig. 3A. In contrast, the smallest bars could be differentiated in both x (green rectangle in Fig. 3B) and y (red rectangle in Fig. 3B) directions. The reflectance profiles in Fig. 3C further confirmed the resolution enhancement of the VSD-based super-resolution imaging in x direction. Likewise, Fig. 3D confirmed the resolution enhancement in y direction.



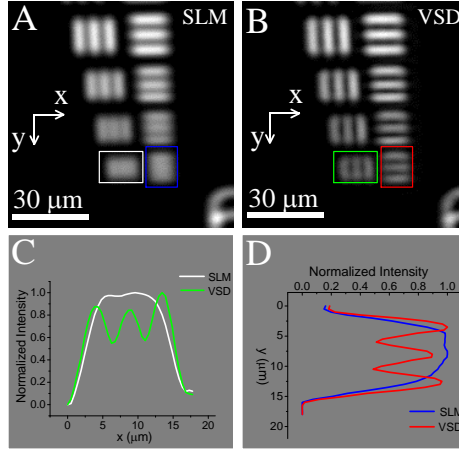


Fig. 3. Implementation of the VSD-based super-resolution imaging on the resolution test target. (A) Image of the test target acquired by conventional SLM. (B) Super-resolution image by VSD reconstruction. (C) Normalized intensity curves along x axis. The white curve was normalized intensity along x direction of the area specified by white rectangle in (A). The green curve was normalized intensity along x direction of the area specified by green rectangle in (B). (D) Normalized intensity curves along x axis. The blue curve was normalized intensity along y direction of the area specified by blue rectangle in (A). The red curve was normalized intensity along y direction of the area specified by red rectangle in (B).

### 3.3. VSD-based super-resolution imaging of isolated retina

The second step of this study was to verify the feasibility of the VSD-based super-resolution imaging of photoreceptors in intact retina. We used the freshly isolated frog retina for this technical validation. The diameter of frog rods is  $\sim 5\text{-}8\ \mu\text{m}$ , and cones  $\sim 1\text{-}3\ \mu\text{m}$  [26, 27]. Therefore, conventional SLM which has lateral resolution  $5\ \mu\text{m}$  could only resolve partial amount of photoreceptors in Fig. 4A. In contrast, the VSD-based super-

resolution microscopy, which has lateral resolution  $2.5\ \mu\text{m}$ , was able to detect more photoreceptors in Fig. 4B. For example, the region specified by the white ellipse in Fig. 4A appeared to be a single blur structure, while in the same area in Fig. 4B seven individual photoreceptors could be resolved. The resolution enhancement of the VSD-based super-resolution imaging could be also exemplified by comparing intensity profiles along lines drawn in Fig. 4A and Fig. 4B. Three clear bumps (arrowheads in Fig. 4C) corresponding to three photoreceptors (green arrowheads in Fig. 4B) became much more prominent in the red curve compared to the white curve in Fig. 4C.

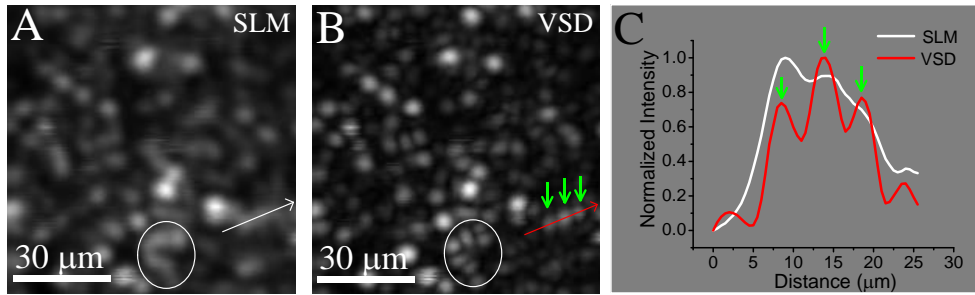


Fig. 4. VSD-based super-resolution imaging of freshly isolated frog retina. (A) Image of the retina acquired by conventional SLM. (B) Super-resolution image of the retina by VSD reconstruction. (C) Reflectance profiles of the white and red line areas in A and B. The white curve and the red curve were normalized intensity profiles along the white line in (A) and the red line in (B), respectively.

#### 4. Discussion

In summary, the VSD-based super-resolution imaging has been experimentally validated to break the diffraction limit. The theoretical simulation result indicated that the VSD-based super-resolution method was capable of enhancing the lateral resolution by a

factor of two (Fig. 2). Experimental imaging of optical target (Fig. 3) and isolated retina (Fig. 4) verified that the VSD-based super-resolution imaging revealed detailed structures that were not detectable in conventional SLM. Although the VSD-based method can be implemented in an imaging system with a high magnification objective, we selected a relatively low magnification objective (5X) in this study for technical validation of super-resolution imaging of retinal photoreceptors.

The VSD-based super-resolution imaging has two technical merits over conventional SIM. First, the VSD-based super-resolution imaging is modulation artifact free. In conventional SIM systems, dynamic phase (e.g.,  $0^\circ$ ,  $120^\circ$  and  $240^\circ$ ) modulation of structured illumination (e.g., sinusoidal gratings) is necessary for super-resolution reconstruction. Therefore, precise phase manipulation of illumination patterns is necessary, which makes conventional SIM vulnerable to modulation artifacts [30, 31]. In contrast, the VSD-based super-resolution imaging applies virtual modulation digitally, and thus it is modulation artifact free. Second, the VSD-based super-resolution imaging provides improved sectioning ability. In conventional wide-field SIM, only modulation with positive magnitude on the illumination is allowed [12]. Therefore, there is a DC component in Eq. (8):

$$m(x, y) = 1 + \cos[2\pi f_0 (x \cos\theta + y \sin\theta) + \alpha] \quad (17)$$

Eq. (15) consequently becomes:

$$\begin{aligned} \tilde{p}(f_x, f_y) &= \tilde{h}_{il}(f_x, f_y) \tilde{s}(f_x, f_y) \\ &+ 0.5 \tilde{h}_{il}(f_x, f_y) \tilde{s}(f_x - f_0 \cos\theta, f_y - f_0 \sin\theta) e^{i\alpha} \\ &+ 0.5 \tilde{h}_{il}(f_x, f_y) \tilde{s}(f_x + f_0 \cos\theta, f_y + f_0 \sin\theta) e^{-i\alpha} \end{aligned} \quad (18)$$

The first item in Eq. (18) contains the zero spatial frequency that does not attenuate with defocus in a wide-field illumination system [32]. Although the structured illumination can theoretically remove the first item in Eq. (18), the first item may become dominant and overwhelm the second and third items that contain super-resolution information in a complex structure, especially in thick tissues. Thus, it has been challenging to conduct wide-field SIM in deep ( $> 100 \mu\text{m}$ ) tissues. In contrast, a confocal configuration, such as the VSD-based super-resolution imaging, can provide improved sectioning capability, due to attenuated zero spatial frequency signals correlated with out-of-focus volumes [33]. In order to further improve the sectioning ability, we are currently pursuing a VSD-based super-resolution optical coherence tomography (OCT). We anticipate the OCT technique can provide improved penetration capability and enhanced imaging resolution in deep tissues. Moreover, we anticipate that VSD can have extended application in super-resolution assessment of retinal structures *in vivo*. High resolution is important for advanced retinal study and diagnosis. Adaptive optics (AO) [34] has been used to compensate for optical aberration of ocular optics to achieve diffraction limited resolution [35, 36]. Further integration of VSD into SLO promises a possible strategy to break the diffraction limit in *in vivo* imaging of the retina.

## 5. Conclusion

The VSD-based super-resolution imaging has been demonstrated as a new strategy to break the diffraction limit. The VSD method is modulation artifact free, with improved sectioning ability, compared to wide-field SIM. In addition to confocal SLM demonstrated in this paper, the VSD method can be integrated into other imaging

modalities, such as line-scan confocal imager [37, 38], multifocal scanning system [39], OCT, SLO, etc..

### **Acknowledgments**

This research is supported in part by NSF CBET-1055889, NIH R21 RR025788, NIH R21 EB012264, and UASOM I3 Pilot Award.

## Reference

1. S. W. Hell and J. Wichmann, "Breaking the diffraction resolution limit by stimulated emission: stimulated-emission-depletion fluorescence microscopy," *Opt. Lett.* **19**, 780-782 (1994).
2. S. Berning, K. I. Willig, H. Steffens, P. Dibaj, and S. W. Hell, "Nanoscopy in a living mouse brain," *Science* **335**, 551 (2012).
3. M. J. Rust, M. Bates, and X. Zhuang, "Sub-diffraction-limit imaging by stochastic optical reconstruction microscopy (STORM)," *Nat. Methods* **3**, 793-795 (2006).
4. E. Betzig, G. H. Patterson, R. Sougrat, O. W. Lindwasser, S. Olenych, J. S. Bonifacino, M. W. Davidson, J. Lippincott-Schwartz, and H. F. Hess, "Imaging intracellular fluorescent proteins at nanometer resolution," *Science* **313**, 1642-1645 (2006).
5. M. F. Juetten, T. J. Gould, M. D. Lessard, M. J. Mlodzianoski, B. S. Nagpure, B. T. Bennett, S. T. Hess, and J. Bewersdorf, "Three-dimensional sub-100 nm resolution fluorescence microscopy of thick samples," *Nat. Methods* **5**, 527-529 (2008).
6. S. A. Jones, S. H. Shim, J. He, and X. Zhuang, "Fast, three-dimensional super-resolution imaging of live cells," *Nat. Methods* **8**, 499-508 (2011).
7. S. H. Shim, C. Xia, G. Zhong, H. P. Babcock, J. C. Vaughan, B. Huang, X. Wang, C. Xu, G. Q. Bi, and X. Zhuang, "Super-resolution fluorescence imaging of organelles in live cells with photoswitchable membrane probes," *Proc. Natl. Acad. Sci. U. S. A.* **109**, 13978-13983 (2012).
8. H. Shroff, C. G. Galbraith, J. A. Galbraith, H. White, J. Gillette, S. Olenych, M. W. Davidson, and E. Betzig, "Dual-color superresolution imaging of genetically expressed probes within individual adhesion complexes," *Proc. Natl. Acad. Sci. U. S. A.* **104**, 20308-20313 (2007).
9. M. Bertero, P. Brianzi, and E. Pike, "Super-resolution in confocal scanning microscopy," *Inverse Probl.* **3**, 195-212 (1987).
10. M. Bertero, P. Boccacci, M. DeFrise, C. De Mol, and E. Pike, "Super-resolution in confocal scanning microscopy: II. The incoherent case," *Inverse Probl.* **5**, 441-461 (1989).
11. M. DeFrise and C. De Mol, "Super-resolution in confocal scanning microscopy: generalized inversion formulae," *Inverse Probl.* **8**, 175-185 (1992).
12. M. G. Gustafsson, "Surpassing the lateral resolution limit by a factor of two using structured illumination microscopy," *J. Microsc.* **198**, 82-87 (2000).

13. M. G. Gustafsson, "Nonlinear structured-illumination microscopy: wide-field fluorescence imaging with theoretically unlimited resolution," *Proc. Natl. Acad. Sci. U. S. A.* **102**, 13081-13086 (2005).
14. M. G. Gustafsson, L. Shao, P. M. Carlton, C. J. Wang, I. N. Golubovskaya, W. Z. Cande, D. A. Agard, and J. W. Sedat, "Three-dimensional resolution doubling in wide-field fluorescence microscopy by structured illumination," *Biophys. J.* **94**, 4957-4970 (2008).
15. D. Debarre, E. J. Botcherby, M. J. Booth, and T. Wilson, "Adaptive optics for structured illumination microscopy," *Opt. Express* **16**, 9290-9305 (2008).
16. D. Karadagic and T. Wilson, "Image formation in structured illumination wide-field fluorescence microscopy," *Micron* **39**, 808-818 (2008).
17. J. Lu, W. Min, J. A. Conchello, X. S. Xie, and J. W. Lichtman, "Super-resolution laser scanning microscopy through spatiotemporal modulation," *Nano Lett.* **9**, 3883-3889 (2009).
18. D. M. Rector, D. M. Ranken, and J. S. George, "High-performance confocal system for microscopic or endoscopic applications," *Methods* **30**, 16-27 (2003).
19. M. Rajadhyaksha, R. R. Anderson, and R. H. Webb, "Video-rate confocal scanning laser microscope for imaging human tissues in vivo," *Appl. Opt.* **38**, 2105-2115 (1999).
20. A. Dubra, Y. Sulai, J. L. Norris, R. F. Cooper, A. M. Dubis, D. R. Williams, and J. Carroll, "Noninvasive imaging of the human rod photoreceptor mosaic using a confocal adaptive optics scanning ophthalmoscope," *Biomed. Opt. Express* **2**, 1864-1876 (2011).
21. M. J. Booth, M. A. Neil, R. Juskaitis, and T. Wilson, "Adaptive aberration correction in a confocal microscope," *Proc. Natl. Acad. Sci. U. S. A.* **99**, 5788-5792 (2002).
22. T. Y. Chui, D. A. Vannasdale, and S. A. Burns, "The use of forward scatter to improve retinal vascular imaging with an adaptive optics scanning laser ophthalmoscope," *Biomed. Opt. Express* **3**, 2537-2549 (2012).
23. T. Wilson and A. R. Carlini, "Size of the detector in confocal imaging systems," *Opt. Lett.* **12**, 227-229 (1987).
24. M. Bertero and P. Boccacci, "Super-resolution in computational imaging," *Micron* **34**, 265-273 (2003).
25. M. G. L. Gustafsson, D. A. Agard, and J. W. Sedat, "Doubling the lateral resolution of wide-field fluorescence microscopy using structured illumination," *Proc. SPIE* **3919**, 141-150 (2000).

26. S. E. Nilsson, "An Electron Microscopic Classification of the Retinal Receptors of the Leopard Frog (*Rana Pipiens*)," *J. Ultrastruct. Res.* **10**, 390-416 (1964).
27. P. A. Liebman and G. Entine, "Visual pigments of frog and tadpole (*Rana pipiens*)," *Vision Res.* **8**, 761-775 (1968).
28. X. C. Yao and Y. B. Zhao, "Optical dissection of stimulus-evoked retinal activation," *Opt. Express* **16**, 12446-12459 (2008).
29. X. C. Yao, A. Yamauchi, B. Perry, and J. S. George, "Rapid optical coherence tomography and recording functional scattering changes from activated frog retina," *Appl. Opt.* **44**, 2019-2023 (2005).
30. S. A. Shroff, J. R. Fienup, and D. R. Williams, "Phase-shift estimation in sinusoidally illuminated images for lateral superresolution," *J. Opt. Soc. Am. A Opt. Image Sci. Vis.* **26**, 413-424 (2009).
31. S. A. Shroff, J. R. Fienup, and D. R. Williams, "Lateral superresolution using a posteriori phase shift estimation for a moving object: experimental results," *J. Opt. Soc. Am. A Opt. Image Sci. Vis.* **27**, 1770-1782 (2010).
32. M. A. Neil, R. Juskaitis, and T. Wilson, "Method of obtaining optical sectioning by using structured light in a conventional microscope," *Opt. Lett.* **22**, 1905-1907 (1997).
33. T. Wilson, *Confocal microscopy* (Academic Press, London, 1990)
34. J. Liang, D. R. Williams, and D. T. Miller, "Supernormal vision and high-resolution retinal imaging through adaptive optics," *J. Opt. Soc. Am. A* **14**, 2884-2892 (1997).
35. D. Merino, J. L. Duncan, P. Tiruveedhula, and A. Roorda, "Observation of cone and rod photoreceptors in normal subjects and patients using a new generation adaptive optics scanning laser ophthalmoscope," *Biomed. Opt. Express* **2**, 2189-2201 (2011).
36. R. J. Zawadzki, S. M. Jones, S. Pilli, S. Balderas-Mata, D. Y. Kim, S. S. Olivier, and J. S. Werner, "Integrated adaptive optics optical coherence tomography and adaptive optics scanning laser ophthalmoscope system for simultaneous cellular resolution in vivo retinal imaging," *Biomed. Opt. Express* **2**, 1674-1686 (2011).
37. Q. X. Zhang, R. W. Lu, C. A. Curcio, and X. C. Yao, "In vivo confocal intrinsic optical signal identification of localized retinal dysfunction," *Invest. Ophthalmol. Vis. Sci.* **53**, 8139-8145 (2012).
38. Q. X. Zhang, R. W. Lu, Y. G. Li, and X. C. Yao, "In vivo confocal imaging of fast intrinsic optical signals correlated with frog retinal activation," *Opt. Lett.* **36**, 4692-4694 (2011).
39. Q. X. Zhang, J. Y. Wang, L. Liu, and X. C. Yao, "Microlens array recording of localized retinal responses," *Opt. Lett.* **35**, 3838-3840 (2010).



RAPID SUPER-RESOLUTION LINE SCANNING MICROSCOPY THROUGH  
VIRTUALLY STRUCTURED DETECTION

by

RONGWEN LU, YANAN ZHI, BENQUAN WANG, QIUXIANG ZHANG AND  
XINCHENG YAO

In Preparation for Optics Letters

Format adapted for dissertation

## **Abstract**

Virtually structured detection (VSD) has been demonstrated to achieve resolution-doubling in scanning laser microscopy (SLM) and optical coherence tomography (OCT). The VSD provides an easy, low-cost and phase-artifact free strategy to achieve super-resolution imaging. However, deployable application of the method is challenged by limited frame speed. We report here to combine the VSD to line scanning microscopy (LSM) to improve imaging speed. A motorized dove prism is employed to achieve automatic control of four-angle ( $0^\circ$ ,  $45^\circ$ ,  $90^\circ$  and  $135^\circ$ ) scanning, and thus to ensure isotropic resolution improvement. Optical resolution target and living retinal tissue are used to verify the resolution-doubling.

*OCIS codes:* (100.6640) Superresolution; (170.3880) Medical and biological imaging; (180.5810) Scanning Microscopy.

## **Body of Paper**

Advanced light microscopy possesses important role in laboratory research and clinical diagnosis due to its excellent ability to identify fine structures invisible to naked eyes. Multiple imaging modalities such as phase contrast microscopy, differential interference contrast (DIC), confocal scanning laser microscopy (SLM), and fluorescence microscopy have been developed to extend the capabilities of light microscopy. However, spatial resolution of conventional microscopy is fundamentally limited by light diffraction. For fluorescence imaging, multiple strategies have been developed to break the diffraction limit, such as stimulated emission depletion (STED) microscopy, stochastic optical reconstruction microscopy (STORM) [1], photoactivated localization

microscopy (PALM) [2], fluorescence PALM (FPALM) [3] and structured illumination microscopy (SIM) [4-6]. For the STED imaging, the shape of effective illumination point spread function (PSF) of the excitation light is sharpened by doughnut-shape depletion light which deactivates peripheral regions of the center focal spot while leaving the fluorophores at the desired center to emit fluorescence. Single-molecule imaging, i.e., STORM, PALM, and FPALM, alternatively can achieve super-resolution resolution by localizing centroids of individual single molecules with photo-switchable fluorescence probes. Both STED and single-molecular imaging modalities requires specific dyes or fluorescent proteins, and are not suitable for autofluorescence imaging or intrinsic signal (i.e., reflection or transmission) imaging.

The SIM is applicable to both fluorescence [4-6] and intrinsic signal imaging [7, 8]. The SIM requires a sinusoidal patterned illumination to shift some high frequency information beyond the diffraction limit to the lower frequency, and thus the passing band of one optical system can be effectively expanded. However, for the purpose of the reconstruction, the SIM requires complicated mechanical manipulation of grating [4-6] or grid [9, 10] to generate structured illumination patterns with specific phases, which is particularly challenging for the moving sample. In addition, the SIM (i.e., epi-illumination SIM) employs wide field illumination which is difficult to penetrate through thick (i.e.  $> 100 \mu\text{m}$ ) tissues. There are currently two strategies to modify the epi-illumination SIM for applications in thick tissues. First, the wide field illumination is condensed to a single line illumination which consists of two superimposed lines of illumination [11, 12]. Along the longitudinal direction the intensity is modulated with sinusoidal function because of interference of two illumination lines. Therefore, there

will be resolution enhancement along this direction, just as epi-illumination SIM, while at the same time the condensed illumination allows optical sectioning by reducing the out-of-focus light. However, in this scheme, the axial resolution is compromised by the reduced effective numerical aperture of the objective [11]. The other strategy is to combine the structured illumination with light sheet illumination [13, 14]. Perpendicular to the direction of observation, a sheet of structured light pattern is sent to the sample. Because only the volume close to the focal plane of the detection objective is illuminated, the structured light sheet microscopy could provide unparalleled optical sectioning ability. However, it is not practical to employ the light sheet approach for *in vivo* applications such as cortex or retinal imaging.

In theory, SIM can also be realized in a point scanning system through spatiotemporal modulation, either by modulating light source intensity in illumination light path or by moving a physical mask in detection light path [15]. However, the spatiotemporal modulation of the illumination/detection light is technically difficult. So far, experimental validation of the proposed spatiotemporal modulation is not yet demonstrated. We recently demonstrated the VSD-based super-resolution SLM [16] and OCT [17], which requires neither dynamic modulation of the light source intensity in illumination arm nor the physical mask in light detection arm [15]. However, the imaging speed of our prototype SLM was limited. Instead of using a high speed photo detector in conventional confocal microscope, a digital camera was required for capturing light profile of individual sampling points in the VSD-based SLM. Typically, it took ~40 s ( $100 \times 100 \mu\text{m}$ ) to collect data necessary for one super-resolution image. In this paper, we report a system to combine VSD to line scanning microscopy (LSM) to enhance the

image acquisition speed.

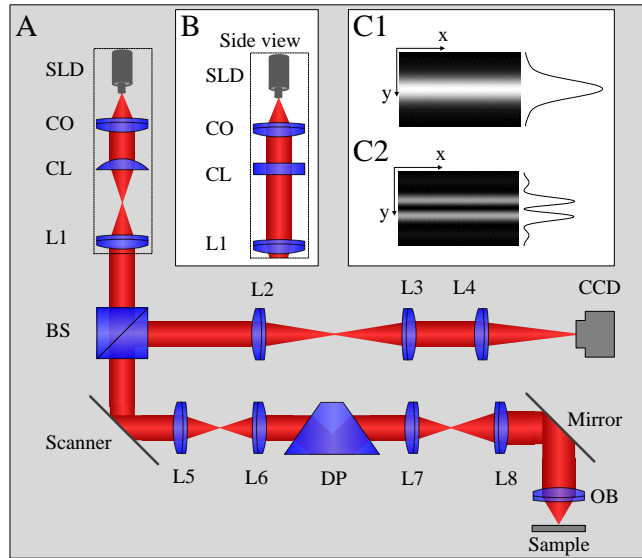


Fig.1. Schematic diagram of experimental setup. OB: objective; CO: collimator; L1-L8: lens; and BS: beam splitter. Focal lengths of lenses L1-L8 are 100 mm, 150 mm, 40 mm, 80 mm, 100 mm, 100 mm, 75 mm, and 100 mm, respectively. The NA of 5 X objective is 0.1. SLD is the light source (center wavelength  $\lambda=830$  nm and bandwidth  $\Delta\lambda=60$  nm). The theoretical resolution of this system is  $0.61\lambda/\text{NA}=5$   $\mu\text{m}$ . The inset (B) is the side view of the illumination beam. The inset (C1) is the simulated image acquired by the camera. The height of the image (along y axis) is 20  $\mu\text{m}$  which is twice the diameter of the Airy disc. Along y axis the intensity profile is the convolution between one dimensional illumination PSF and detection PSF, while it is constant along x axis. (C2) Superimposed image between (C1) and the modulation function.

Figure 1 illustrates a schematic diagram of the VSD-based super-resolution LSM. A low coherence near infrared (NIR) source (SLD-35-HP, SUPERLUM), with center wavelength  $\lambda=830$  nm and bandwidth  $\Delta\lambda=60$  nm, is employed to illuminate the specimen. A cylindrical lens CL is used to condense the light into a focused line, which is

imaged to the sample. The focused line is swept across the specimen by a scanning mirror (GVS001, THORLABS). The pivot point of the scanner is conjugate to the pupil plane of the objective to minimize the vignetting effect. The reflected light from the sample is descanned by the scanner, and is relayed to the image plane. In conventional line scanning microscopy system, a linear camera is used [18]. Here, a camera of two-dimensional CCD array (AVT Pike F-032B) is used to record light profile of individual sampling lines, as shown in Fig. 1C1. The theoretical lateral resolution of the conventional SLM is 5  $\mu\text{m}$  for 0.1 numerical aperture (NA) 5X objective. After VSD reconstruction, the theoretical resolution can be enhanced by a factor of two. To achieve the isotropic resolution improvement, a custom-designed dove prism DP is mounted to a motorized rotation stage to rotate the image field. Given the fact that rotation of the prism with respect to the longitudinal axis rotates the image field at twice the rate of the prism's rotation, ( $0^\circ$ ,  $22.5^\circ$ ,  $45^\circ$  and  $67.5^\circ$ ) dove prism rotation is required to produce the four-angle ( $0^\circ$ ,  $45^\circ$ ,  $90^\circ$  and  $135^\circ$ ) scanning pattern.

The detail principle of VSD has been described in our recent publication [16]. In conventional SIM, the acquired wide-field image can be presented as:

$$p(x, y) = \{[m(x, y) \otimes h_{il}(x, y)]s(x, y)\} \otimes h_{de}(x, y) \quad (1)$$

where  $m$  is the modulation function,  $s$  is reflectance ratio,

and  $h_{il}$  and  $h_{de}$  are PSFs of illumination path and detection path, respectively.  $\otimes$  denotes convolution. In the VSD-based SLM, Two dimensional light profiles of individual scanning points are collected (Fig. 1C1), modulated (Fig. 1C2) and then integrated, generating an image:

$$\begin{aligned}
p(x, y) &= \iint [h_{il}(u-x, v-y)s(u, v)] \otimes h_{de}(u, v)m(u, v)dudv \\
&= h_{il}(x, y) \otimes \{s(x, y)[h_{de}(x, y) \otimes m(x, y)]\} \\
&= \{[m(x, y) \otimes h_{de}(x, y)]s(x, y)\} \otimes h_{il}(x, y) \tag{2}
\end{aligned}$$

where the fact that  $h_{il}$  and  $h_{de}$  are even functions is applied. If we assume  $h_{il}$  and  $h_{de}$  are identical, then Eq. (1) is exactly equivalent to Eq. (2). In other word, modulations in the illumination arm and in the detection arm are equivalent to each other in theory. If we only consider one dimension (i.e., along y axis) as for the VSD-based LSM, Eq. (2) can be rewritten:

$$p(y) = \{[m(y) \otimes h_{de}(y)]s(y)\} \otimes h_{il}(y) \tag{3}$$

Along y axis, the resolution can be doubled, while along x axis, the resolution keeps the same as the wide field microscopy. Therefore, the image field needs to be rotated to achieve isotropic resolution doubling.

We select a region of interest (ROI) of the camera using a virtual slit of 2X Airy disc diameters for VSD reconstruction. Considering the pixel size of the camera is  $7.4 \times 7.4 \mu\text{m}$  and the magnification of the system is 11.11, 2X Airy disc diameters is corresponding to  $\sim 31$  pixels at the image plane. At the x direction, although we could set the maximum length of 640 pixels, we choose 150 pixels so that the field of view is identical to our early works for quantitative comparison. Therefore, the ROI of the camera area is  $31 \times 150$  pixels. Along y axis, we sample 150 lines. Thus the final reconstructed super-resolution image size is  $150 \times 150$  pixels. Each raw CCD frame takes 1 ms. To cover the same field of view ( $150 \times 150$  pixels), the single point VSD scheme in our prototype instrument requires  $\sim 40$  s. In contrast, the line scanning scheme only

requires  $\sim 0.15$  s to finish one dimensional scanning, and thus possible in-frame blur due to sample movement can be suppressed. For isotropic resolution enhancement, four-angle ( $0^\circ$ ,  $45^\circ$ ,  $90^\circ$  and  $135^\circ$ ) scanning pattern is used. It is worth noting that at  $45^\circ$  and  $135^\circ$  the ROI of camera should be set longer to  $31 \times 213$  pixels to cover the field of view at  $45^\circ$  and  $135^\circ$ . However, the line readout rate of the camera is the same if the height of the ROI keeps the same (31 lines) even though each line is longer. It takes  $\sim 0.6$  s ( $0.15$  s  $\times 4$ ) for the camera to acquire images at four scanning angles and  $\sim 1.4$ s ( $0.47$  s  $\times 3$ ) for the rotation motor (NR360S, THROLABS) to control the dove prism at the desired angles in sequence ( $0^\circ$ ,  $22.5^\circ$ ,  $45^\circ$  and  $67.5^\circ$ ). Therefore, it takes in total  $\sim 2$  s ( $0.6$  s +  $1.4$  s) to scan four angles for reconstructing a final isotropic super-resolution image of the VSD-based LSM. Compared to our previous prototype SLM with single point scanning scheme which required  $\sim 40$  s to cover the same field of view, the speed is increased by a factor of  $\sim 20$ .

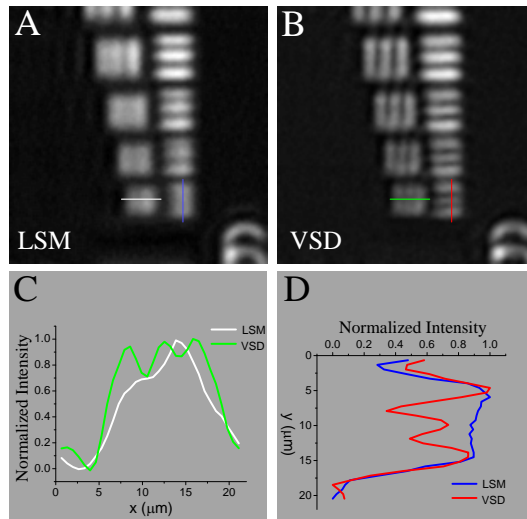


Fig. 2. VSD-based super-resolution LSM on the resolution test target. (A) Image of the test target acquired by conventional LSM. (B) Super-resolution image by VSD reconstruction. The field of the view of both (A) and (B) is  $100 \times 100$   $\mu\text{m}$ . (C)



Normalized intensity profiles along x axis. The white curve was normalized intensity profile along the white line in (A). The green curve was normalized intensity profile along the green line in (B). (D) Normalized intensity profiles along y axis. The blue curve was normalized intensity profile along the blue line in (A). The red curve was normalized intensity profile along the red line in (B).

A standard resolution target (USAF 1951 1X, EDMOND) was employed to verify the resolution enhancement of the VSD-based super-resolution LSM. Fig.2 shows the comparison between conventional LSM (Fig. 2A) and VSD-based super-resolution LSM (Fig. 2B) images. The smallest grating has a period of 4.4  $\mu\text{m}$ . Therefore, the conventional LSM which has a theoretical resolution of 5  $\mu\text{m}$  could not differentiate them, as shown in Fig. 2A. In contrast, after VSD reconstruction, the smallest grating could be resolved, in both horizontal direction (specified by green line in Fig. 2B) and the vertical direction (specified by red line in Fig. 2B). The resolution enhancement could be confirmed in Figs. 2C and 2D. In Fig. 2C, three bumps could be observed in the green curve which is the intensity profile along the horizontal green line in Fig. 2B, while it is difficult to differentiate them at the white curve which is the intensity profile along the horizontal white line in Fig. 2A. Likewise, in Fig. 2D three bumps along y axis could be resolved (red curve in Fig. 2D) after VSD reconstruction, while they are hidden in the blue curve in Fig. 2D before VSD reconstruction.

Freshly isolated frog (*Rana Pipiens*) retina was also used for functional validation of the VSD-based super-resolution LSM system. It is established that the frog retina consists of photoreceptors with variable diameters (rods:  $\sim 5\text{-}8\ \mu\text{m}$ ; cones:  $\sim 1\text{-}3\ \mu\text{m}$ ) [19, 20]. Therefore, the frog retina provides a simple preparation to evaluate the LSM

resolution before (5  $\mu\text{m}$ ) and after (2.5  $\mu\text{m}$ ) VSD data processing. Animal handling was approved by the Institutional Animal Care and Use Committee of the University of Alabama at Birmingham. Preparation procedures of freshly isolated retinas have been documented in previous publications [21, 22]. Briefly, the frog was euthanized by rapid decapitation and double pithing. After enucleating frog eyes, we hemisected the globe below the equator with fine scissors. The lens and anterior structures were removed before the retina was separated from the retinal pigment epithelium. Then the retina was moved into the chamber with Ringer solution for imaging. Fig. 3A shows one image acquired by the conventional LSM, while Fig. 3B illustrates super-resolution image through VSD reconstruction. At the area marked by the white circle in Fig. 3B, seven photoreceptors could be clearly identified after VSD reconstruction. The red curve (Fig. 3C) of the intensity profile along the red line in Fig. 3B shows two clear bumps, while the white curve of the intensity profile along the white line in Fig. 3A only shows one wider blunt bump, which confirms the resolution enhancement in the thick tissue.

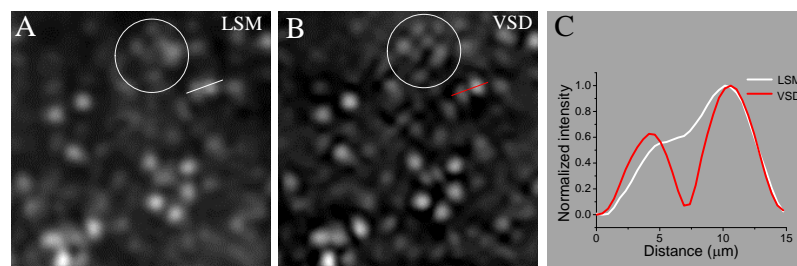


Fig. 3. VSD-based super-resolution LSM imaging of freshly isolated frog retina. The frog was placed with the photoreceptor layer downward and the illumination light entered the retina from the natural direction, i.e., from the nerve fiber layer. (A) Image of the retina acquired by conventional LSM. (B) Super-resolution image of the retina by VSD reconstruction. The field of the view of both (A) and (B) is  $100 \times 100 \mu\text{m}$ . (C)

Reflectance profiles of the white and red lines in A and B. The white curve and the red curve were normalized intensity profiles along the white line in (A) and the red line in (B), respectively.

In summary, a line scanning strategy is combined with VSD to achieve rapid super-resolution imaging. A motorized dove prism is employed to achieve rapid change of four-angle ( $0^\circ$ ,  $45^\circ$ ,  $90^\circ$  and  $135^\circ$ ) scanning, and thus to ensure isotropic resolution improvement. Both standard resolution target and living retinal tissue are used to verify the resolution-doubling. Further combination of the VSD to line-scan OCT to improve the axial resolution is also possible [17].

High imaging speed is important for practical application of the super-resolution LSM for imaging biological dynamics and moving samples. Currently, it takes  $\sim 0.15$  s for one-angle scan and  $\sim 2$  s in total for four-angle recordings required for one super-resolution image. It is significantly improved compared to our prototype VSD SLM with single point scanning scheme which required  $\sim 40$  s to cover the same field of view ( $100 \times 100 \mu\text{m}$ ) [16, 17]. Within one-angle scan, the imaging speed is limited by the line readout rate. If a faster camera is used (i.e., pco.dimax S, PCO-TECH), it is possible to reduce the time to 5 ms to finish one-angle scan while maintaining the field of view. Thus, in-frame movements (i.e., movements during one-angle scan) could be minimized for *in vivo* applications, i.e., cortex or retinal imaging. The imaging speed for the four-angle scan which is to ensure isotropic resolution improvement is not only determined by the camera but also the rotation motor of dove prism. If a faster motorized rotation stage (i.e., RGV160BL, NEWPORT) is used, the time required to rotate the dove prism to specific angles in sequence ( $0^\circ$ ,  $22.5^\circ$ ,  $45^\circ$  and  $67.5^\circ$ ) could be reduced to 70 ms ( $23 \text{ ms} \times 3$ ).

Although the time for rotating the dove prism is relatively longer than the imaging time for the one-angle scan (e.g., 5 ms), the displacement of the sample among different scanning angles could be corrected by the tracking system or the global registration method. In principle, future integration of acousto-optic dove prism can provide fast angle rotation at microsecond speed [23]. We anticipate further development of the VSD-based LSM could achieve super-resolution imaging in *in vivo* cortex imaging or retinal imaging.

This research is supported in part by NIH R01 EY023522, NIH R01 EY024628, NSF CBET-1055889, and NSF EPSCoR-158862.

### References

1. M. J. Rust, M. Bates, and X. Zhuang, "Sub-diffraction-limit imaging by stochastic optical reconstruction microscopy (STORM)," *Nature methods* **3**, 793-795 (2006).
2. E. Betzig, G. H. Patterson, R. Sougrat, O. W. Lindwasser, S. Olenych, J. S. Bonifacino, M. W. Davidson, J. Lippincott-Schwartz, and H. F. Hess, "Imaging intracellular fluorescent proteins at nanometer resolution," *Science* **313**, 1642-1645 (2006).
3. M. F. Juette, T. J. Gould, M. D. Lessard, M. J. Mlodzianoski, B. S. Nagpure, B. T. Bennett, S. T. Hess, and J. Bewersdorf, "Three-dimensional sub-100 nm resolution fluorescence microscopy of thick samples," *Nature methods* **5**, 527-529 (2008).
4. M. G. Gustafsson, "Surpassing the lateral resolution limit by a factor of two using structured illumination microscopy," *Journal of microscopy* **198**, 82-87 (2000).
5. M. G. Gustafsson, "Nonlinear structured-illumination microscopy: wide-field fluorescence imaging with theoretically unlimited resolution," *Proceedings of the National Academy of Sciences of the United States of America* **102**, 13081-13086 (2005).
6. M. G. Gustafsson, L. Shao, P. M. Carlton, C. J. Wang, I. N. Golubovskaya, W. Z. Cande, D. A. Agard, and J. W. Sedat, "Three-dimensional resolution doubling in wide-field fluorescence microscopy by structured illumination," *Biophysical journal* **94**, 4957-4970 (2008).

7. S. Chowdhury, A. H. Dhalla, and J. Izatt, "Structured oblique illumination microscopy for enhanced resolution imaging of non-fluorescent, coherently scattering samples," *Biomedical optics express* **3**, 1841-1854 (2012).
8. J. H. Park, J. Y. Lee, and E. S. Lee, "Enhancing the isotropy of lateral resolution in coherent structured illumination microscopy," *Biomedical optics express* **5**, 1895-1912 (2014).
9. D. Debarre, E. J. Botcherby, M. J. Booth, and T. Wilson, "Adaptive optics for structured illumination microscopy," *Optics express* **16**, 9290-9305 (2008).
10. D. Karadagic and T. Wilson, "Image formation in structured illumination wide-field fluorescence microscopy," *Micron* **39**, 808-818 (2008).
11. T. Kim, D. Gweon, and J. H. Lee, "Enhancement of fluorescence confocal scanning microscopy lateral resolution by use of structured illumination," *Meas Sci Technol* **20**(2009).
12. O. Mandula, M. Kielhorn, K. Wicker, G. Krampert, I. Kleppe, and R. Heintzmann, "Line scan--structured illumination microscopy super-resolution imaging in thick fluorescent samples," *Optics express* **20**, 24167-24174 (2012).
13. L. Gao, L. Shao, B. C. Chen, and E. Betzig, "3D live fluorescence imaging of cellular dynamics using Bessel beam plane illumination microscopy," *Nature protocols* **9**, 1083-1101 (2014).
14. T. A. Planchon, L. Gao, D. E. Milkie, M. W. Davidson, J. A. Galbraith, C. G. Galbraith, and E. Betzig, "Rapid three-dimensional isotropic imaging of living cells using Bessel beam plane illumination," *Nature methods* **8**, 417-423 (2011).
15. J. Lu, W. Min, J. A. Conchello, X. S. Xie, and J. W. Lichtman, "Super-resolution laser scanning microscopy through spatiotemporal modulation," *Nano letters* **9**, 3883-3889 (2009).
16. R. W. Lu, B. Q. Wang, Q. X. Zhang, and X. C. Yao, "Super-resolution scanning laser microscopy through virtually structured detection," *Biomedical optics express* **4**, 1673-1682 (2013).
17. B. Wang, R. Lu, Q. Zhang, and X. Yao, "Breaking diffraction limit of lateral resolution in optical coherence tomography," *Quant Imaging Med Surg* **3**, 243-248 (2013).
18. R. W. Lu, C. A. Curcio, Y. Zhang, Q. X. Zhang, S. J. Pittler, D. Deretic, and X. C. Yao, "Investigation of the hyper-reflective inner/outer segment band in optical coherence tomography of living frog retina," *Journal of biomedical optics* **17**, 060504 (2012).
19. S. E. Nilsson, "An Electron Microscopic Classification of the Retinal Receptors of the Leopard Frog (*Rana Pipiens*)," *Journal of ultrastructure research* **10**, 390-416 (1964).

20. P. A. Liebman and G. Entine, "Visual pigments of frog and tadpole (*Rana pipiens*)," *Vision research* **8**, 761-775 (1968).
21. X. C. Yao and Y. B. Zhao, "Optical dissection of stimulus-evoked retinal activation," *Optics express* **16**, 12446-12459 (2008).
22. X. C. Yao, A. Yamauchi, B. Perry, and J. S. George, "Rapid optical coherence tomography and recording functional scattering changes from activated frog retina," *Applied optics* **44**, 2019-2023 (2005).
23. E. G. Paek, J. Y. Choe, T. K. Oh, J. H. Hong, and T. Y. Chang, "Nonmechanical image rotation with an acousto-optic dove prism," *Optics letters* **22**, 1195-1197 (1997).

## SUMMARY

The objective of this dissertation is to explore intrinsic structural and functional biomarkers for assessments of morphological structures and physiological conditions of the outer retina. This dissertation research is twofold: (1) to investigate two structural biomarkers (FAF and OCT) and one functional biomarker (transient rod phototropic adaptation); (2) to develop a super-resolution method, VSD, for confocal scanning imaging systems to break the diffraction limit on transverse direction, which allows reliable evaluation of structural and functional biomarkers.

Explorations in FAF imaging using two-photon excitation revealed origins of FAF throughout retinal depth. Autofluorescence signals could be observed from all retinal layers. At the PIO, ONL, INL, and GCL, cellular structures could be observed. At the PIO, autofluorescence signals were dominant in the intracellular compartment of the photoreceptors. Homogeneous autofluorescence could be observed in the rod outer segment, while sub-cellular bright spots well above the surrounding area were identified close to the edge of cone outer segment. These bright spots coincided with the position of the connecting cilium. They may imply different fluorophores or alternatively a different optical structure in cones. Mixed intracellular and extracellular autofluorescence signals were observed at the ONL, INL, and GCL. Autofluorescence signals could be also observed from the OPL and IPL. Previous studies showed that NAD(P)H and oxidized flavoproteins in mitochondria could contribute FAF signals [60]. Therefore, they might be also helpful for functional evaluation of metabolic activates. Further research might

reveal discrete features of cones and rods, respectively.

Investigation on OCT biomarkers was to identify anatomic origins of the presumed 'IS/OS' OCT band by comparing OCT images with histological images quantitatively. LS-OCT was developed to achieve sub-cellular resolution in both lateral and axial directions to obtain high-quality OCT images to facilitate comparison. The OCT distance ratio  $(OCT_{IS/OS} - OCT_{OLM}) / (OCT_{OLM} - OCT_{OPL})$  was significantly smaller than the histological distance ratio  $(H_{IS/OS} - H_{OLM}) / (H_{OLM} - H_{OPL})$ . The significant difference suggests that dominant source of the signal reported as the 'IS/OS' OCT band actually originates from the IS.

Examinations on the transient phototropism show that rod photoreceptors in frog and mouse retinas rapidly shifted toward the incident direction of oblique stimuli on transverse direction. In contrast, movements of cones were negligible. Such transient phototropism is one mechanism of observed IOS biomarker. In addition, such rod-dominant transient phototropic response could compensate for the loss of illumination efficiency under oblique stimulation in the rod system which may explain for Stiles-Crawford effect (SCE) is exclusively observed in cone photoreceptors and is absent in rod photoreceptors. In other words, rapid (onset: ~10 ms for frog and ~ 5 ms for mouse; time-to-peak: ~200 ms for frog and ~20 ms for mouse) phototropic adaptation in retinal rods is too quick for the SCE to be detected by conventional psychophysical methods with the advanced involvement of brain perception. OCT imaging could further characterize the transient phototropism along the axial direction.

High resolution imaging is important for reliable interpretations of structural and functional biomarkers. VSD was developed for confocal scanning system to break the



diffraction limit on transverse direction. VSD was first integrated to confocal SLM with single point raster scanning pattern. The theoretical simulation result indicated that the VSD-based super-resolution method was capable of enhancing the lateral resolution by a factor of two. Experimental imaging of optical target and isolated retina verified that the VSD-based super-resolution imaging revealed detailed structures that were not detectable in conventional SLM. VSD was also applicable for time-domain OCT [19], although the corresponding published paper was not presented in this dissertation. Because the raster scanning pattern is time consuming, we integrated VSD to LSM with line scanning pattern for high speed super-resolution imaging. A motorized dove prism is employed to achieve rapid change of four-angle ( $0^\circ$ ,  $45^\circ$ ,  $90^\circ$  and  $135^\circ$ ) scanning, and thus to ensure isotropic resolution improvement. Both standard resolution target and living retinal tissue are used to verify the resolution-doubling. Further combination of the VSD to line-scan OCT to improve the axial resolution is also possible. High imaging speed is important for practical application of the super-resolution LSM for imaging biological dynamics and moving samples. Currently, it takes  $\sim 0.15$  s for one-angle scan and  $\sim 2$  s in total for four-angle recordings required for one super-resolution image. It is significantly improved compared to the prototype VSD SLM with single point scanning scheme which required  $\sim 40$  s to cover the same field of view ( $100 \times 100 \mu\text{m}$ ). The imaging speed could be further improved by using a faster camera and a faster rotation motor. Within one-angle scan, the imaging time could be reduced to 5 ms. Therefore, within-frame movements could be minimized for retinal imaging. To finish four-angle scans, the bottleneck of the imaging speed is limited by the mechanical movement of the rotation motor. However, if within-frame blurring is minimized, the

displacement of the sample among different scanning angles could be corrected by the tracking system or the global registration method. Therefore, VSD-based LSM with line scanning pattern promises a practical super-resolution approach for sub-diffraction-limited *in vivo* retinal imaging.

In summary, this dissertation research characterized FAF cross all retinal layers, investigated the origin of the presumed ‘IS/OS’ OCT band, explored the transient phototropic responses of rod photoreceptors and developed a super-resolution imaging method for confocal scanning systems. This dissertation could not only contribute to a better understanding of the existing clinical FAF and OCT biomarkers for eye disease diagnosis, but also discovered and explored a new functional biomarker, transient phototropism, which may promise an alternative methodology for early diagnosis of eye diseases. Moreover, VSD, a super-resolution method developed in this dissertation research, allows imaging of subtle structural and functional biomarkers for more reliable assessments of the retina.

## GENERAL LIST OF REFERENCES

1. S. G. Schuman, A. F. Koreishi, S. Farsiu, S. H. Jung, J. A. Izatt, and C. A. Toth, "Photoreceptor layer thinning over drusen in eyes with age-related macular degeneration imaged in vivo with spectral-domain optical coherence tomography," *Ophthalmology* **116**, 488-496 e482 (2009).
2. N. M. Bressler, S. B. Bressler, and S. L. Fine, "Age-related macular degeneration," *Survey of ophthalmology* **32**, 375-413 (1988).
3. C. A. Curcio, N. E. Medeiros, and C. L. Millican, "Photoreceptor loss in age-related macular degeneration," *Investigative ophthalmology & visual science* **37**, 1236-1249 (1996).
4. R. M. Petters, C. A. Alexander, K. D. Wells, E. B. Collins, J. R. Sommer, M. R. Blanton, G. Rojas, Y. Hao, W. L. Flowers, E. Banin, A. V. Cideciyan, S. G. Jacobson, and F. Wong, "Genetically engineered large animal model for studying cone photoreceptor survival and degeneration in retinitis pigmentosa," *Nature biotechnology* **15**, 965-970 (1997).
5. C. P. Herbort, "Fluorescein and indocyanine green angiography for uveitis," *Middle East African journal of ophthalmology* **16**, 168-187 (2009).
6. W. R. Freeman, D. U. Bartsch, A. J. Mueller, A. S. Banker, and R. N. Weinreb, "Simultaneous indocyanine green and fluorescein angiography using a confocal scanning laser ophthalmoscope," *Archives of ophthalmology* **116**, 455-463 (1998).
7. M. D. Abramoff, M. K. Garvin, and M. Sonka, "Retinal imaging and image analysis," *IEEE reviews in biomedical engineering* **3**, 169-208 (2010).
8. R. Alford, H. M. Simpson, J. Duberman, G. C. Hill, M. Ogawa, C. Regino, H. Kobayashi, and P. L. Choyke, "Toxicity of organic fluorophores used in molecular imaging: literature review," *Molecular imaging* **8**, 341-354 (2009).
9. M. Hope-Ross, L. A. Yannuzzi, E. S. Gragoudas, D. R. Guyer, J. S. Slakter, J. A. Sorenson, S. Krupsky, D. A. Orlock, and C. A. Puliafito, "Adverse reactions due to indocyanine green," *Ophthalmology* **101**, 529-533 (1994).
10. S. Schmitz-Valckenberg, F. G. Holz, A. C. Bird, and R. F. Spaide, "Fundus autofluorescence imaging: review and perspectives," *Retina* **28**, 385-409 (2008).
11. C. H. Chen, E. Tsina, M. C. Cornwall, R. K. Crouch, S. Vijayaraghavan, and Y. Koutalos, "Reduction of all-trans retinal to all-trans retinol in the outer segments of frog and mouse rod photoreceptors," *Biophys J* **88**, 2278-2287 (2005).
12. M. Han, G. Giese, S. Schmitz-Valckenberg, A. Bindewald-Wittich, F. G. Holz, J. Y.

- Yu, J. F. Bille, and M. H. Niemz, "Age-related structural abnormalities in the human retina-choroid complex revealed by two-photon excited autofluorescence imaging," *Journal of Biomedical Optics* **12**(2007).
13. Y. Imanishi, K. H. Lodowski, and Y. Koutalos, "Two-photon microscopy: Shedding light on the chemistry of vision," *Biochemistry* **46**, 9674-9684 (2007).
  14. R. W. Lu, Y. C. Li, T. Ye, C. Strang, K. Keyser, C. A. Curcio, and X. C. Yao, "Two-photon excited autofluorescence imaging of freshly isolated frog retinas," *Biomedical optics express* **2**, 1494-1503 (2011).
  15. R. W. Lu, C. A. Curcio, Y. Zhang, Q. X. Zhang, S. J. Pittler, D. Deretic, and X. C. Yao, "Investigation of the hyper-reflective inner/outer segment band in optical coherence tomography of living frog retina," *Journal of biomedical optics* **17**, 060504 (2012).
  16. B. Wang, R. Lu, Q. Zhang, Y. Jiang, and X. Yao, "En face optical coherence tomography of transient light response at photoreceptor outer segments in living frog eyecup," *Optics letters* **38**, 4526-4529 (2013).
  17. R. Lu, A. M. Levy, Q. Zhang, S. J. Pittler, and X. Yao, "Dynamic near-infrared imaging reveals transient phototropic change in retinal rod photoreceptors," *Journal of biomedical optics* **18**, 106013 (2013).
  18. R. W. Lu, B. Q. Wang, Q. X. Zhang, and X. C. Yao, "Super-resolution scanning laser microscopy through virtually structured detection," *Biomedical optics express* **4**, 1673-1682 (2013).
  19. B. Wang, R. Lu, Q. Zhang, and X. Yao, "Breaking diffraction limit of lateral resolution in optical coherence tomography," *Quantitative imaging in medicine and surgery* **3**, 243-248 (2013).
  20. M. Minsky, "Memoir on inventing the confocal scanning microscope," *Scanning* **10**, 128-138 (1988).
  21. C. Sheppard and T. Wilson, "Image formation in scanning microscopes with partially coherent source and detector," *Journal of Modern Optics* **25**, 315-325 (1978).
  22. G. Li, H. Zwick, B. Stuck, and D. J. Lund, "On the use of schematic eye models to estimate retinal image quality," *Journal of biomedical optics* **5**, 307-314 (2000).
  23. J. M. Schmitt, "Optical coherence tomography (OCT): a review," *Selected Topics in Quantum Electronics, IEEE Journal of* **5**, 1205-1215 (1999).
  24. X. C. Yao, A. Yamauchi, B. Perry, and J. S. George, "Rapid optical coherence tomography and recording functional scattering changes from activated frog retina," *Applied optics* **44**, 2019-2023 (2005).
  25. J. M. Huntley, G. H. Kaufmann, and D. Kerr, "Phase-shifted dynamic speckle pattern interferometry at 1 kHz," *Applied optics* **38**, 6556-6563 (1999).
  26. H. P. Scholl and E. Zrenner, "Electrophysiology in the investigation of acquired retinal disorders," *Survey of ophthalmology* **45**, 29-47 (2000).

27. D. C. Hood, "Assessing retinal function with the multifocal technique," *Progress in retinal and eye research* **19**, 607-646 (2000).
28. R. A. Stepnoski, A. LaPorta, F. Raccuia-Behling, G. E. Blonder, R. E. Slusher, and D. Kleinfeld, "Noninvasive detection of changes in membrane potential in cultured neurons by light scattering," *Proceedings of the National Academy of Sciences of the United States of America* **88**, 9382-9386 (1991).
29. I. Tasaki and P. M. Byrne, "Rapid structural changes in nerve fibers evoked by electric current pulses," *Biochemical and biophysical research communications* **188**, 559-564 (1992).
30. M. W. Kaplan and M. E. Deffebach, "Birefringence measurements of structural inhomogeneities in *Rana pipiens* rod outer segments," *Biophysical journal* **23**, 59-70 (1978).
31. P. A. Liebman, W. S. Jagger, M. W. Kaplan, and F. G. Bargoot, "Membrane structure changes in rod outer segments associated with rhodopsin bleaching," *Nature* **251**, 31-36 (1974).
32. Q. X. Zhang, R. W. Lu, J. D. Messinger, C. A. Curcio, V. Guarcello, and X. C. Yao, "In vivo Optical Coherence Tomography of Light-Driven Melanosome Translocation in Retinal Pigment Epithelium," *Sci Rep* **3**, 2644 (2013).
33. Y. C. Li, C. Strang, F. R. Amthor, L. Liu, Y. G. Li, Q. X. Zhang, K. Keyser, and X. C. Yao, "Parallel optical monitoring of visual signal propagation from the photoreceptors to the inner retina layers," *Optics letters* **35**, 1810-1812 (2010).
34. Q. X. Zhang, R. W. Lu, C. A. Curcio, and X. C. Yao, "In vivo confocal intrinsic optical signal identification of localized retinal dysfunction," *Investigative ophthalmology & visual science* **53**, 8139-8145 (2012).
35. C. Owsley, G. McGwin, Jr., G. R. Jackson, K. Kallies, and M. Clark, "Cone- and rod-mediated dark adaptation impairment in age-related maculopathy," *Ophthalmology* **114**, 1728-1735 (2007).
36. K. Shintani, D. L. Shechtman, and A. S. Gurwood, "Review and update: current treatment trends for patients with retinitis pigmentosa," *Optometry-Journal of the American Optometric Association* **80**, 384-401 (2009).
37. M. J. Rust, M. Bates, and X. Zhuang, "Sub-diffraction-limit imaging by stochastic optical reconstruction microscopy (STORM)," *Nature methods* **3**, 793-795 (2006).
38. E. Betzig, G. H. Patterson, R. Sougrat, O. W. Lindwasser, S. Olenych, J. S. Bonifacino, M. W. Davidson, J. Lippincott-Schwartz, and H. F. Hess, "Imaging intracellular fluorescent proteins at nanometer resolution," *Science* **313**, 1642-1645 (2006).
39. M. F. Juetten, T. J. Gould, M. D. Lessard, M. J. Mlodzianoski, B. S. Nagpure, B. T. Bennett, S. T. Hess, and J. Bewersdorf, "Three-dimensional sub-100 nm resolution fluorescence microscopy of thick samples," *Nature methods* **5**, 527-529 (2008).
40. M. G. Gustafsson, "Surpassing the lateral resolution limit by a factor of two using structured illumination microscopy," *Journal of microscopy* **198**, 82-87 (2000).

41. M. G. Gustafsson, "Nonlinear structured-illumination microscopy: wide-field fluorescence imaging with theoretically unlimited resolution," *Proceedings of the National Academy of Sciences of the United States of America* **102**, 13081-13086 (2005).
42. M. G. Gustafsson, L. Shao, P. M. Carlton, C. J. Wang, I. N. Golubovskaya, W. Z. Cande, D. A. Agard, and J. W. Sedat, "Three-dimensional resolution doubling in wide-field fluorescence microscopy by structured illumination," *Biophysical journal* **94**, 4957-4970 (2008).
43. S. Chowdhury, A. H. Dhalla, and J. Izatt, "Structured oblique illumination microscopy for enhanced resolution imaging of non-fluorescent, coherently scattering samples," *Biomedical optics express* **3**, 1841-1854 (2012).
44. J. H. Park, J. Y. Lee, and E. S. Lee, "Enhancing the isotropy of lateral resolution in coherent structured illumination microscopy," *Biomedical optics express* **5**, 1895-1912 (2014).
45. D. Debarre, E. J. Botcherby, M. J. Booth, and T. Wilson, "Adaptive optics for structured illumination microscopy," *Optics express* **16**, 9290-9305 (2008).
46. D. Karadaglic and T. Wilson, "Image formation in structured illumination wide-field fluorescence microscopy," *Micron* **39**, 808-818 (2008).
47. J. Lu, W. Min, J. A. Conchello, X. S. Xie, and J. W. Lichtman, "Super-resolution laser scanning microscopy through spatiotemporal modulation," *Nano letters* **9**, 3883-3889 (2009).
48. Y. J. Sepah, A. Akhtar, M. A. Sadiq, Y. Hafeez, H. Nasir, B. Perez, N. Mawji, D. J. Dean, D. Ferraz, and Q. D. Nguyen, "Fundus autofluorescence imaging: Fundamentals and clinical relevance," *Saudi Journal of Ophthalmology* **28**, 111-116 (2014).
49. S. Schmitz-Valckenberg, A. Bindewald-Wittich, J. Dolar-Szczasny, J. Dreyhaupt, S. Wolf, H. P. Scholl, and F. G. Holz, "Correlation between the area of increased autofluorescence surrounding geographic atrophy and disease progression in patients with AMD," *Investigative ophthalmology & visual science* **47**, 2648-2654 (2006).
50. P. Popović, M. Jarc-Vidmar, and M. Hawlina, "Abnormal fundus autofluorescence in relation to retinal function in patients with retinitis pigmentosa," *Graefe's Archive for Clinical and Experimental Ophthalmology* **243**, 1018-1027 (2005).
51. S. P. Haen and R. F. Spaide, "Fundus autofluorescence in multifocal choroiditis and panuveitis," *American journal of ophthalmology* **145**, 847-853 (2008).
52. N. L. Gomes, V. C. Greenstein, J. N. Carlson, S. H. Tsang, R. T. Smith, R. E. Carr, D. C. Hood, and S. Chang, "A comparison of fundus autofluorescence and retinal structure in patients with Stargardt disease," *Investigative ophthalmology & visual science* **50**, 3953-3959 (2009).
53. J. C. Hwang, D. Y. Kim, C. L. Chou, and S. H. Tsang, "Fundus Autofluorescence, Optical Coherence Tomography, and Electroretinogram Findings Choroidal Sclerosis," *Retina-the Journal of Retinal and Vitreous Diseases* **30**, 1095-1103 (2010).

54. D. C. Hood, X. Zhang, R. Ramachandran, C. L. Talamini, A. Raza, J. P. Greenberg, J. Sherman, S. H. Tsang, and D. G. Birch, "The inner segment/outer segment border seen on optical coherence tomography is less intense in patients with diminished cone function," *Investigative ophthalmology & visual science* **52**, 9703-9709 (2011).
55. N. Doble, S. S. Choi, J. L. Codona, J. Christou, J. M. Enoch, and D. R. Williams, "In vivo imaging of the human rod photoreceptor mosaic," *Optics letters* **36**, 31-33 (2011).
56. D. Merino, J. L. Duncan, P. Tiruveedhula, and A. Roorda, "Observation of cone and rod photoreceptors in normal subjects and patients using a new generation adaptive optics scanning laser ophthalmoscope," *Biomedical optics express* **2**, 2189-2201 (2011).
57. E. A. Rossi, M. Chung, A. Dubra, J. J. Hunter, W. H. Merigan, and D. R. Williams, "Imaging retinal mosaics in the living eye," *Eye* **25**, 301-308 (2011).
58. A. Binns and T. H. Margrain, "Development of a technique for recording the focal rod ERG," *Ophthalmic Physiol Opt* **26**, 71-79 (2006).
59. R. Klein, Q. Wang, B. E. Klein, S. E. Moss, and S. M. Meuer, "The relationship of age-related maculopathy, cataract, and glaucoma to visual acuity," *Investigative ophthalmology & visual science* **36**, 182-191 (1995).
60. B. L'Heureux, H. Gurden, and F. Pain, "Autofluorescence imaging of NADH and flavoproteins in the rat brain: insights from Monte Carlo simulations," *Optics express* **17**, 9477-9490 (2009).

## APPENDIX A

### INSTITUTIONAL ANIMAL CARE AND USE COMMITTEE

#### Admission to Candidacy Research Compliance Verification Form

**Instructions**

Complete this form, including all applicable forms and the signatures of the student, the student's advisor, and the Graduate Program Director. For research approval forms, contact the Institutional Review Board (IRB) (<http://www.uab.edu/irb> or 934-3789), or the Institutional Animal Care and Use Committee (IACUC) (<http://www.uab.edu/iacuc> or 934-7692).

**Human Subjects**

The University of Alabama at Birmingham defines a human subject as not only a living human being, but also human tissue, blood samples, pathology or diagnostic specimens, study of medical records, observation of public behavior, and all questionnaires or surveys.

Does the research proposed by the student involve human subjects?  Yes (continue below)  No

This research is:

Approved \_\_\_\_\_ Date \_\_\_\_\_

IRB Protocol No. \_\_\_\_\_

Attach a copy of your IRB approval. Your own name must appear on the original approval or on an attached amendment.

**Animal Subjects**

The University of Alabama at Birmingham defines a laboratory animal as any vertebrate animal (e.g., traditional laboratory animals, farm animals, wildlife, and aquatic animals) and certain higher invertebrate animals used in research, teaching, or testing at UAB or sponsored through UAB but conducted off-site (i.e., field research or at collaborating institutions, etc.).

Does the research proposed by the student involve animal subjects?  Yes (continue below)  No

This research is:

Approved X Date 02/15/2013

IACUC Protocol No. 130309367

Attach a copy of your IACUC Notice of Approval, showing your research subject and the animal project number. If your own name does not appear on the Notice of Approval, take this form to the IACUC office for verification of approval.

The IACUC office verifies that Rongwen Lu is covered under the attached approval.  
(name of candidate)

Signature of IACUC representative [Signature] Date: 8-22-13

**NOTE: The student's advisor, the student, and the Graduate Program Director agree that no research will be initiated until an application is submitted for review and approved by the appropriate review boards (IRB and/or IACUC) if the proposed thesis or dissertation project requires approval. If approval already exists, this student's name must be added to the existing protocol before candidacy will be approved by the Graduate School. It is the responsibility of the student's advisor and the student to comply with federal and UAB regulations associated with this research. Documentation of continuous, appropriate approval will be required before degree conferral; all required IRB and/or IACUC approvals must be current at the time final versions of theses or dissertations are submitted to the Graduate School.**

<p><u>Rongwen Lu</u> Student's Signature</p> <p><u>Xin Cheng Yao</u> Signature of Student's Advisor</p> <p><u>Vladimir Fast</u> Graduate Program Director</p>	<p><u>Biomedical Engineering</u> <u>08/22/2013</u> Dept. Date</p> <p><u>Biomedical Engineering</u> <u>8-27-2013</u> Dept. Date</p> <p><u>BME</u> <u>8/27/13</u> Dept. Date</p>
---------------------------------------------------------------------------------------------------------------------------------------------------------------------------	--------------------------------------------------------------------------------------------------------------------------------------------------------------------------------------------





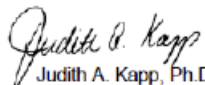
THE UNIVERSITY OF ALABAMA AT BIRMINGHAM

*Institutional Animal Care and Use Committee (IACUC)*

**NOTICE OF RENEWAL**

**DATE:** February 15, 2013

**TO:** XINCHENG YAO, Ph.D.  
VH -390B 0019  
FAX: (205) 975-4919

**FROM:**   
Judith A. Kapp, Ph.D., Chair  
Institutional Animal Care and Use Committee (IACUC)

**SUBJECT:** Title: Angle-Resolved Polarization Signal Imaging of Early Receptor Potential  
Sponsor: NIH  
Animal Project Number: 130309367

As of March 31, 2013, the animal use proposed in the above referenced application is renewed. The University of Alabama at Birmingham Institutional Animal Care and Use Committee (IACUC) approves the use of the following species and numbers of animals:

Species	Use Category	Number in Category
Frogs	A	100
Invertebrates	A	40

Animal use must be renewed by March 30, 2014. Approval from the IACUC must be obtained before implementing any changes or modifications in the approved animal use.

**Please keep this record for your files, and forward the attached letter to the appropriate granting agency.**

Refer to Animal Protocol Number (APN) 130309367 when ordering animals or in any correspondence with the IACUC or Animal Resources Program (ARP) offices regarding this study. If you have concerns or questions regarding this notice, please call the IACUC office at (205) 934-7692.

Institutional Animal Care and Use Committee  
CH19 Suite 403  
933 19<sup>th</sup> Street South  
205.934.7692  
FAX 205.934.1188

Mailing Address:  
CH19 Suite 403  
1530 3RD AVE S  
BIRMINGHAM AL 35294-0019



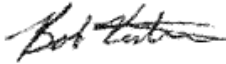
THE UNIVERSITY OF ALABAMA AT BIRMINGHAM

*Institutional Animal Care and Use Committee (IACUC)*

**NOTICE OF APPROVAL**

**DATE:** February 12, 2014

**TO:** XINCHENG YAO, Ph.D.  
VH -390B  
(205) 996-7459

**FROM:**   
Robert A. Kesterson, Ph.D., Chair  
Institutional Animal Care and Use Committee (IACUC)

**SUBJECT:** Title: Functional Imaging of Retinal Photoreceptors  
Sponsor: NIH  
Animal Project\_Number: 140210050

As of February 12, 2014 the animal use proposed in the above referenced application is approved. The University of Alabama at Birmingham Institutional Animal Care and Use Committee (IACUC) approves the use of the following species and number of animals:

Species	Use Category	Number In Category
Mice	A	96
Frogs	A	100

Animal use must be renewed by February 11, 2015. Approval from the IACUC must be obtained before implementing any changes or modifications in the approved animal use.

**Please keep this record for your files, and forward the attached letter to the appropriate granting agency.**

Refer to Animal Protocol Number (APN) 140210050 when ordering animals or in any correspondence with the IACUC or Animal Resources Program (ARP) offices regarding this study. If you have concerns or questions regarding this notice, please call the IACUC office at (205) 934-7692.

<b>Institutional Animal Care and Use Committee (IACUC)</b> CH19 Suite 403 933 19th Street South (205) 934-7692 FAX (205) 934-1188	Mailing Address: CH19 Suite 403 1530 3rd Ave S Birmingham, AL 35294-0019
-----------------------------------------------------------------------------------------------------------------------------------------------	-----------------------------------------------------------------------------------



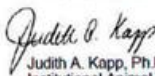
THE UNIVERSITY OF ALABAMA AT BIRMINGHAM

*Institutional Animal Care and Use Committee (IACUC)*

**Notice of Approval for Protocol Modification**

**DATE:** June 21, 2011

**TO:** STEVEN J PITTER, Ph.D.  
VH -375B 0019  
FAX: (205) 934-5725

**FROM:**   
Judith A. Kapp, Ph.D., Chair  
Institutional Animal Care and Use Committee (IACUC)

**SUBJECT:** Title: Analysis of Retina Rod Photoreceptor GARP and cGMP-Gated Cation Channel  
Sponsor: NIH  
Animal Project Number: 110208381

On June 21, 2011, the University of Alabama at Birmingham Institutional Animal Care and Use Committee (IACUC) reviewed the animal use proposed in the above referenced application. It approved the modification as described: Additional Personnel to protocol: Rongwen Lu, Qiuxiang Zhang, Location: VH - 340,342,344. The sponsor for this project may require notification of modification(s) approved by the IACUC but not included in the original grant proposal/experimental plan; please inform the sponsor if necessary. The following species and numbers of animals reflect this modification.

Species	Use Category	Number in Category
Mice	B	Zero - Procedural modification only

The IACUC is required to conduct continuing review of approved studies. This study is scheduled for annual review on or before February 24, 2012. Approval from the IACUC must be obtained before implementing any changes or modifications in the approved animal use.

**Please keep this record for your files.**

Refer to Animal Protocol Number (APN) 110208381 when ordering animals or in any correspondence with the IACUC or Animal Resources Program (ARP) offices regarding this study. If you have concerns or questions regarding this notice, please call the IACUC office at (205) 934-7692.

**Institutional Animal Care and Use Committee**  
403 Community Health  
933 19<sup>th</sup> St S  
205.934.7692  
FAX 205.934.1188

**Mailing Address:**  
403 CH19  
1530 3RD AVE S  
BIRMINGHAM AL 35294-2041